Universitat Autònoma de Barcelona

**Escola Tècnica Superior d'Enginyeria**

**Departament d'Enginyeria Química**

# MATHEMATICAL MODELLING AND MOLECULAR ANALYSIS OF A NITRIFYING PACKED BED BIOFILM REACTOR

**PhD Thesis**

ANNA MONTRÀS BOET

February 2009

**Title:**

Mathematical modelling and molecular analysis of a nitrifying packed bed biofilm reactor

**Author:**

Anna Montràs Boet

**Directors:**

Dr. Francesc Gòdia Casablancas

Dr. Julio Pérez Cañestro

FRANCESC GÒDIA CASABLANCAS, catedràtic del Departament d'Enginyeria Química de la Universitat Autònoma de Barcelona i JULIO PÉREZ CAÑESTRO, professor agregat del Departament d'Enginyeria Química de la Universitat Autònoma de Barcelona,

CERTIFIQUEM:

Que l'enginyera Anna Montràs Boet ha realitzat amb la nostra direcció el treball que amb el títol "Mathematical modelling and molecular analysis of a nitrifying packed bed biofilm reactor" es presenta en aquesta memòria, i que constitueix la seva Tesi per a optar al Grau de Doctora per la Universitat Autònoma de Barcelona.

I perquè en prengueu coneixement i consti als efectes oportuns, presentem a l'Escola de Postgrau de la Universitat Autònoma de Barcelona l'esmentada Tesi, signant el present certificat a

Bellaterra, Febrer 2009

Dr. FRANCESC GÒDIA CASABLANCAS Dr. JULIO PÉREZ CAÑESTRO

*Als meus pares, Joaquim i Montserrat*

*“I've seen the bridge and the bridge is long*
*And they built it high and they built it strong*
*Strong enough to hold the weight of time*
*Long enough to leave some of us behind*

*And every one of us has to face that day*
*Do you cross the bridge or do you fade away*
*And every one of us that ever came to play*
*Has to cross the bridge or fade away*

*And the bridge it shines*
*Oh cold hard iron*
*Saying come and risk it all*
*Or die trying”*

The Bridge
Elton John & Bernie Taupin, 2006

# Agraïments / Acknowledgements

Després d'uns quants anys dedicats a aquesta tesi, ha arribat el moment de donar per acabada aquesta etapa, de la qual només en tinc bons records. Aquest treball no hauria estat possible sense l'ajut de tots aquells que m'heu acompanyat durant aquests anys.

En primer lloc, avui no seria aquí escrivint aquestes paraules si no fos per l'oportunitat que em va donar en Quico de fer un treball de màster dins del projecte MELiSSA, que es va acabar convertint en una tesi. Moltes gràcies per la confiança i per recolzar-me sempre.

Mai podré agrair prou al Julio les constants aportacions a aquest treball, gràcies per donar-me llibertat quan calia i guiar-me quan feia falta, i per les discussions científiques del dia a dia. No cal dir que aquesta tesi no hagués arribat enlloc sense el teu ajut i la teva confiança.

Moltes gràcies Vane per la teva contribució a la part experimental d'aquest treball, i a la resta de companys del MELiSSA amb qui he compartit moltes hores al laboratori i moltes reunions de grup.

I would like to thank Benny, for all his hard work on the biofilm samples. You know a part of this work is yours.

Special thanks go to the late Larissa Hendrickx. For teaching me all I know about molecular techniques, for her patience and for being the gracious person she was. An important part of this thesis would never have been possible without her valuable contribution.

Gràcies a tots els companys de department, aquests anys no haguessin estat el mateix sense els cafès, dinars, sopars i sortides varies que hem compartit. Us trobaré a faltar!

I és clar, moltes gràcies a tots els amics amb qui he compartit caps de setmana, escapades, viatges i il·lusions durant aquests anys de tesi. Gràcies a la Tània per aguantar-me els canvis d'humor durant l'etapa final de l'escriptura de la tesi.

I no puc acabar sense donar les gràcies als meus pares per donar-me suport i ànims durant aquests anys.

Barcelona, 24 de Febrer de 2009

## Summary

MELiSSA (Micro Ecological Life Support System Alternative) is the system developed by the European Space Agency (ESA) and the MELiSSA consortium in the field of life support for long term manned missions in Space. Based on the principle of an aquatic ecosystem, MELiSSA was conceived as a tool to develop the required technology for a future biological life support system. Its final aim is the production of food, fresh water and oxygen from the organic wastes of a crew.

To achieve this goal, the MELiSSA concept is based on the use of five interconnected compartments colonised by several microorganisms and higher plants. This thesis is focused on the third compartment of the MELiSSA loop, in which ammonium is converted to nitrate, the most suitable nitrogen source for the growth of the bacteria and higher plants colonising the photosynthetic compartment. The biological oxidation of ammonium to nitrate, which consists of two successive reactions carried out by two different bacterial strains, takes place in a packed bed biofilm reactor. *Nitrosomonas europaea* and *Nitrobacter winogradskyi* are immobilised on a polymeric support, with air flowing cocurrently with the feed medium. The pilot-scale reactor of compartment III (CIII) had been in operation in the MELiSSA pilot plant for several years before the start of the present work. The main contributions of this thesis are in increasing the understanding of the reactor performance by studying the nitrifying biofilm in depth, and by developing a mathematical model that allows the effects of different operational parameters on the process and on the biofilm structure, to be studied. Moreover, continuous monitoring of the nitrifying efficiency will be improved by installing the necessary on-line equipment to experimentally measure the concentrations of all the nitrogen species in the liquid phase. The additional knowledge achieved on the reactor performance via this work will finally lead to re-design the reactor hardware for optimal performance in the MELiSSA pilot plant.

Fluorescent *in situ* Hybridisation (FISH), coupled with Confocal Laser Scanning Microscopy (CLSM) observation is used to identify the main trends in the biofilm composition with height. To improve the reliability of the quantification, the Quantitive Polymerase Chain Reaction (Q-PCR) is subsequently used to determine the relative abundance of the two strains. Prior to the application of FISH and Q-PCR, it is assessed using Denaturing Gradient Gel Electrophoresis (DGGE) that *N. europaea* and *N. winogradskyi* are indeed the dominant species in all the biofilm samples. The application of these molecular techniques to analyse the biofilm after a period of operation of 4.8 years confirms the segregation of *N. europaea* and *N. winogradskyi* along the packed bed.

A mathematical model allowing an accurate definition of the biofilm processes is subsequently developed. The model considers the presence of the two initial nitrifying strains (*N. europaea* and *N. winogradskyi*) as well as a population of heterotrophic bacteria growing on the products of bacterial decay. The growth rate of *N. europaea* is considered to be affected by substrate inhibition (free ammonia). For *N. winogradskyi,* non-competitive inhibition by FA and substrate inhibition by free nitrous acid (FNA) is considered. The predictions of the model regarding the biomass distribution along the packed bed at the final steady state correlate well with the trends revealed by molecular analysis, showing a decrease of the *N. europaea* relative abundance with increasing height. The influence of several operational and kinetic parameters on this segregation is investigated to identify the main effects. The mathematical model is subsequently calibrated with experimental data from the reactor start-up process through optimisation of different parameters. The dynamic behaviour of the reactor during perturbations was then simulated. In particular, the backwash events carried out to avoid clogging in the packed bed were studied and the applicability of the model to design an optimal maintenance strategy, in terms of frequency and intensity of the events, was demonstrated. The simulations indicated that stronger backwash events are more convenient than weaker, more frequent events.

The necessary on-line instrumentation to monitor the nitrogen species in the effluent of the reactor is configured and implemented on-line. The performance of the ammonium and nitrate on-line equipment is successfully tested, although several necessary improvements in the analysis cycle are identified. For the continuous monitoring of nitrite two different working strategies were proposed: (i) the indirect estimation of nitrite using the data supplied by the ammonium and nitrate analysers and (ii) the implementation of a nitrite analyser. The first strategy is finally discarded due to the high amplitude noise obtained in the nitrite estimations, which did not fulfil the requirements of the nitrite control system. Therefore, a nitrite analyser based on the spectrophotometric detection of nitrite over a wide range of concentrations (0.005-20 mg $N\text{-}NO_2^- \cdot L^{-1}$) was installed in the MELiSSA pilot plant.

The knowledge acquired in this thesis was finally used to define the main features of the re-design of the pilot reactor of the MELiSSA compartment III.

## Resum

MELiSSA (Micro Ecological Life Support System Alternative) és el sistema desenvolupat per l'Agència Espacial Europea (ESA) i el consorci MELiSSA en el camp del suport de vida durant missions de llarga durada a l'espai. Basat en un ecosistema aquàtic, MELiSSA va ser concebut com una eina per desenvolupar la tecnologia necessària per a un sistema de suport de vida biològic que en un futur ha de permetre la producció d'aliment, aigua i oxigen a partir dels residus orgànics generats per una tripulació.

Per assolir aquest objectiu, el concepte MELiSSA compta amb l'activitat combinada de cinc compartiments colonitzats per diferents microorganismes i plantes superiors, interconnectats entre ells. Aquesta tesi es centra en el tercer compartiment del bucle MELiSSA, en el qual l'amoni és convertit a nitrat, que és la font de nitrogen més adequada per al creixement dels cianobacteris i plantes superiors que colonitzen els compartiments fotosintètics.

L'oxidació biològica d'amoni a nitrat té lloc en dues etapes successives que porten a terme dos tipus de soques bacterianes. En el projecte MELiSSA aquest procés es porta a terme en una columna de llit fix mitjançant *Nitrosomonas europaea* i *Nitrobacter winogradkyi* immobilitzats sobre un suport polimèric, i amb aportació d'aire en el mateix sentit de circulació que el medi líquid. El reactor pilot del tercer compartiment ha estat operant a la planta pilot del projecte MELiSSA durant períodes prolongats de temps abans de l'inici del treball realitzat en aquesta tesi.

La principal aportació d'aquesta tesi es troba en l'aportació de nova informació sobre el funcionament del reactor a través d'un estudi detallat de la biopel·lícula i també mitjançant el desenvolupament d'un model matemàtic que ens permetrà estudiar els efectes de diferents paràmetres d'operació sobre el procés i l'estructura de la biopel·lícula. S'implementaran també els aparells de mesura necessaris per millorar la qualitat de la monitorització de les diferents espècies de nitrogen a la fase líquida. Els coneixements adquirits en la realització d'aquest treball seran utilitzats per portar a terme el re-disseny del reactor per tal de millorar-ne el funcionament dins de la planta pilot del projecte MELiSSA.

El mètode d'hibridació fluorescent *in situ* (FISH), seguit d'observació mitjançant el microscopi làser confocal és utilitzat per identificar la tendència general de la composició de la biopel·lícula a diferents alçades. Per millorar la fiabilitat de la quantificació, s'aplica una anàlisi mitjançant el mètode de la PCR quantitativa (Q-PCR) per determinar de forma fiable l'abundància relativa de les dues espècies bacterianes. Abans de l'aplicació dels mètodes FISH i Q-PCR, la predominància de *N. europaea* i *N.*

*winogradskyi* en les mostres es comprova mitjançant electroforesi en gels de gradient desnaturalitzant (DGGE). L'aplicació d'aquest seguit de tècniques moleculars d'anàlisi a la biopel·lícula després de 4.8 anys d'operació en continu confirma la segregació de *N. europaea* i *N. winogradskyi* al llarg del llit fix.

Tot seguit es desenvolupa un model matemàtic que permeti descriure amb cert rigor els processos que tenen lloc en la biopel·lícula. El model contempla la presència de *N. europaea* i *N. winogradskyi*, a més d'una població heteròtrofa que creix a partir dels productes de lisi cel·lular. El creixement de *N. europaea* es considera inhibit per substrat (amoni lliure), mentre que per *N. winogradskyi* les inhibicions considerades són la inhibició no-competitiva per amoni lliure i la inhibició per substrat (àcid nitrós). Les prediccions del model sobre la distribució de la biomassa al llarg de l'alçada del llit fix a l'estat estacionari final presenten una bona correlació amb les tendències evidenciades per les tècniques d'anàlisi molecular, és a dir, l'abundància relativa de *N. europaea* disminueix a mesura que ens desplacem en l'açada del llit fix. S'estudia la influència de diversos paràmetres cinètics i d'operació sobre aquesta segregació, tot portant a l'identificació dels principals efectes. Tot seguit es porta a terme la calibració del model matemàtic amb dades experimentals obtingudes durant la posada en marxa del reactor, i a través de l'optimització de determinats paràmetres. Es realitza una simulació del comportament del reactor durant perturbacions, concretament s'estudiraran en detall els episodis de rentat en contra-corrent que s'han de portar a terme periòdicament al reactor per evitar la colmatació del llit fix. S'avaluaran les possibilitats d'aplicació del model en el disseny d'una estratègia que permeti optimitzar la intensitat i la freqüència dels episodis de manteniment per reduir-ne els possibles efectes negatius sobre l'eficàcia de nitrificació del reactor. Les simulacions indiquen que un rentat de més intensitat era més recomanable que un rentat freqüent i poc intens.

S'implementarà la instrumentació necessària per monitoritzar les diferents espècies de nitrogen presents a l'efluent del reactor. Es comprovarà el correcte funcionament dels analitzadors d'amoni i de nitrat, tot identificant algunes millores necessàries en la presa de mostra i en el circuït d'anàlisi. Respecte a la monitorització del nitrit es proposen dues possibles estratègies: (i) l'estimació indirecta de la concentració de nitrit utilitzant les dades de concentració mesurades pels analitzadors d'amoni i nitrat i (ii) la implementació d'un analitzador de nitrit.

La primera estratègia es descarta finalment a causa de l'elevada amplitud del soroll que presenten les estimacions de la concentració de nitrit obtingudes mitjançant aquest mètode, les quals no satisfan els requeriments del sistema de control de nitrit. Finalment, s'implementa un analitzador en línia de nitrit que permeti la determinació d'aquest compost en un ampli rang de concentracions (0.005-20 mg $N\text{-}NO_2^- \cdot L^{-1}$). La

informació adquirida sobre el funcionament i l'estructura del reactor en aquesta tesi,.serà utilitzada finalment per definir els requeriments de re-disseny del reactor pilot del compartiment III del projecte MELiSSA.

# Table of contents

**PART III - MATHEMATICAL MODELLING**



**PART IV - NITROGEN MONITORING AND CONTROL**

# PART I

# GENERAL INTRODUCTION

# CHAPTER 1

# INTRODUCTION

## 1.1 LIFE SUPPORT SYSTEMS FOR SPACE MISSIONS

The term life support comprises the main functions required to sustain life in an environment or situation in which the vital functions could not be maintained without the need for external supply. The main objectives of life support systems are the supply of food, water and oxygen and the removal of wastes, faeces, urine and $CO_2$ (Tamponnet et al., 1994).

In the development of space exploration programmes, the key motivation for the development of life support systems is the fulfilment of the needs of a crew during long term manned missions. For this kind of missions, like a trip to Mars, involving long distances and a crew of several members, it is not feasible to resupply water, food and oxygen from Earth due to the technical requirements and the high economical costs connected to the high value of the associated weight. Therefore, a self-sustainable system is required to overcome the limitations imposed by mass transportation on human space exploration.

Life support systems can be classified in two main categories: non-regenerative and regenerative. Non-regenerative systems rely completely on the material taken initially or periodically supplied from the original biosphere while waste material is stored until the end of the mission and returned. Regenerative systems are those that involve water, oxygen and food, all of which have regeneration potential. Different degrees of closure are defined for these systems depending on their recycling capacity towards these resources. The type of process

used for recycling leads to a further division of the regenerative systems into physicochemical and biological (or bioregenerative) systems (Table 1.1).

**Table 1.1** Classification of the regenerative life support systems based on the type of recycling process used for their resources.

| REGENERATIVE SYSTEM CLASSIFICATION | CHARACTERISTICS |
|---|---|
| Physicochemical | Atmospheric management<br>Wastes management<br>Water treatment<br>No food production<br>Suitable for short distance missions |
| Biological | Atmospheric management<br>Wastes management<br>Water treatment<br>Food production (microorganisms, algae, higher plants)<br>Suitable for long distance missions |

The development of life support systems with a high closure level requires the progressive incorporation of biological elements. Therefore, in recent years special attention has been paid to the study of closed ecological systems (Meleshko et al., 1991) as one of the best approaches to a biological life support system for space applications.

The first experiments with systems including algae for oxygen regeneration were carried out in the USA in 1961. Similar experiments were carried out in the former Soviet Union in the same year. In the meantime, research on bioregenerative life support has evolved considerably and currently several organisations are running R&D programs on bioregenerative life support. Government funded projects in progress at the moment include those of the European Space Agency (ESA), the Canadian Space Agency (CSA), the National Aeronautics and Space Administration (NASA) in the USA or the National Space Development Agency (NASDA) in Japan.

Several activities involving life support have been carried out by NASA at different research sites. Currently, all research activity on cyanobacteria and higher plants is carried out in the NASA Specialized Center of Research and Training (NSCORT) located at Purdue University (Mitchell, 1994).

The Bios-1 facility constructed by the former Soviet Union in 1965 experimented with the regeneration of the atmosphere in a sealed 12 $m^3$ chamber through the connection to an 18 L culture of *Chlorella vulgaris.* Further experiments were conducted in 1973 in the Bios-3 facility (Gitelson et al., 1976 and 1989) that demonstrated the viability of a closed ecological system based on a 63 $m^2$ plant growing area to sustain life.

The Closed Ecology Experiment Facility (CEEF) developed by Japan is based on the connection of several modules colonised by plants and animals (Kibe et al., 1997). Closed system experiments using closed CEEF started in 2005 (Abe et al., 2005).

Biosphere 2 was a 1.2 hectare closed chamber built in Arizona. This project, which was financed with private funds, operated in an essentially materially-closed ecological system mode between 1991 and 1994 (Allen et al., 2003). In spite of several problems, the system was successful in supporting life for 2 years with 100% food closure (Drysdale et al., 2003).

The activity of ESA in bioregenerative life support provided the frame for the development of the work presented in this thesis. Therefore the main features of the research conducted by ESA will be described in some detail in the following sections.

## 1.2 THE MELiSSA PROJECT

The MELiSSA (Micro-Ecological Life Support System Alternative) project started at ESA in 1989. The project is managed from ESA's European Space and Technology Center (ESTEC) in Nordwijk (The Netherlands) and it involves several independent organisations: University of Ghent (Belgium), EPAS (Belgium), University of Clermont Ferrand (France), SHERPA Engineering (France), Belgian Nuclear Research Centre (SCK-CEN) in Belgium, Flemish institute for technological research (VITO) in Belgium, Universitat Autònoma de Barcelona (Spain) and University of Guelph (Canada). It is co-funded by ESA, the MELISSA partners, the Belgium (SSTC), Spanish (CIRIT and MCYT) and Canadian (CRESTech) authorities. Contributions for specific studies have been received as well from Ireland and The Netherlands authorities. (Lasseur and Vieira da Silva, 2005).

The following phases have been distinguished in the progress of the MELiSSA project:

1. *Basic research and development*: each compartment of the loop is first analysed separately. The mass balance is mathematically described and is validated with experimental results from batch and continuous cultures. The overall MELISSA loop is then simulated in terms of mass balance and kinetics.

2. *Preliminary flight experiments*: biological processes are known to be influenced by the space environment and thus the quantification of these effects is essential to verify the validity of the engineering work performed in the MELiSSA project.
3. *Ground and space demonstration*: the main features of this phase are (i) MELiSSA Pilot Plant, where the integration and testing of the results obtained by the MELISSA international team are performed, located at Universitat Autònoma de Barcelona; (ii) Concordia station, based on the first compartment, a black water recycling system is under construction for a research base in Antarctic.
4. *Technology transfer:* The combination of advanced biotechnological processes, together with the stringent requirements of a space mission, result in a number of innovative solutions, some of which may find their application to industry.
5. *Education and communication*: The MELiSSA objectives, as well the obtained results, attract the attention of the public opinion

### 1.2.1 MELiSSA CONCEPT

MELiSSA was conceived as a tool to gain understanding of the behaviour of artificial ecosystems, with the final aim to develop the required technology for a future regenerative life support system for long term manned space missions, e.g. a lunar base or a mission to Mars.

The concept of MELiSSA is inspired on the structure of a lake ecosystem (Figure 1.1), using the combined activities of several micro-organisms and higher plants in order to achieve the recovery of edible biomass, water and oxygen from waste (faeces, urea), carbon dioxide and minerals using light as the source of energy to promote biological photosynthesis (Mergeay et al., 1988; Hendrickx and Mergeay, 2007).

MELISSA consists of five interconnected compartments colonised respectively by thermophilic anoxygenic bacteria (CI), photohererotrophic bacteria (CII), nitrifying bacteria (CIII), photosynthetic bacteria (CIVa), higher plants (CIVb), and the crew (V) as shown in Figure 1.2.


**Figure 1.1** Scheme of the different biological functions in a lake ecosystem, providing the basis for the MELiSSA concept.

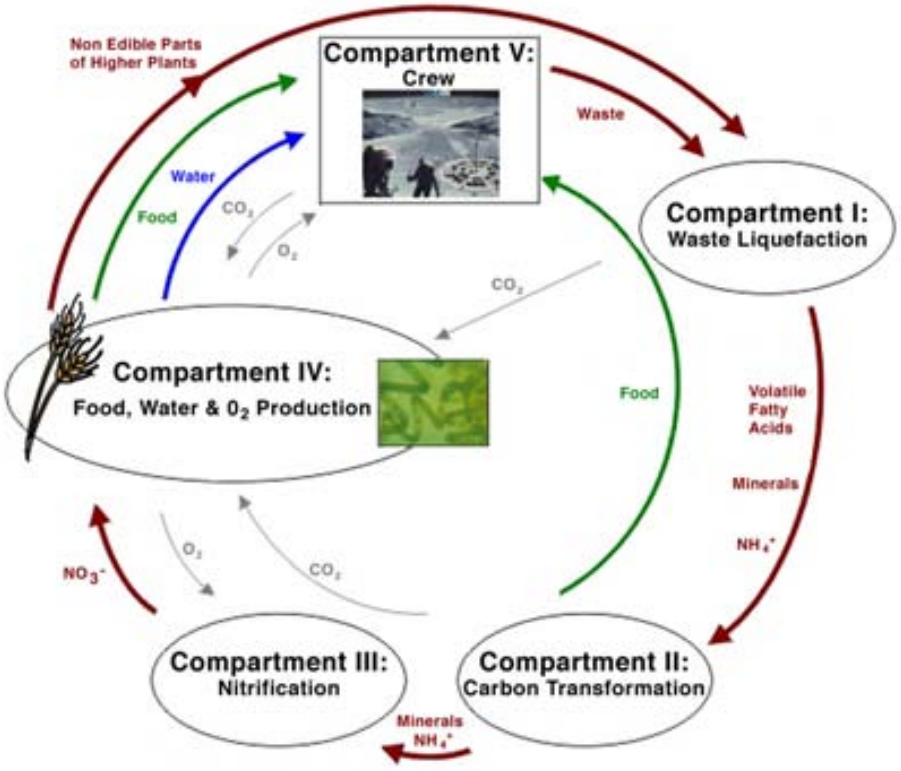


**Figure 1.2** Scheme of the MELiSSA loop as a combination of specific biological compartments. Adapted from Hendrickx et al. (2006).

The first step in the MELiSSA loop is the degradation of organic wastes such as non-edible parts of plant material, paper or crew faeces and urine by the thermophilic anaerobic bacteria of CI. This compartment determines the fraction of these organic wastes that can be recycled in the loop. At present, around 60-70% degradation is achieved (Lasseur and Vieira da Silva, 2005). Research is currently being performed to test physical/chemical treatment of the remaining fraction in order to further improve biodegradability. The improvement of the biodegradation efficiency by fungi is also being investigated.

The $CO_2$ produced in CI is supplied to CIV (photosynthetic compartment). The volatile fatty acids and ammonia produced during the anaerobic fermentation process are fed to the second anoxygenic compartment (CII) where a photoheterotrophic microorganism (*Rhodospirillum rubrum*) converts organic carbon into inorganic carbon sources used in the subsequent compartments, while providing edible biomass (Albiol, 1994; Cornet and Albiol, 2000). The nitrifying compartment (CIII) has, as a main purpose, the conversion of ammonia into nitrate, which is the most suitable nitrogen source for CIV. The oxidation of ammonium in CIII is carried out by *Nitrosomonas europaea*, and the subsequent oxidation of nitrite to nitrate, by *Nitrobacter winogradskyi*, both of which are immobilised onto the surface of a support material (BIOSTYR® beads) forming a biofilm (Pérez et al., 2004). The use of immobilised biomass is the most suitable strategy in this case, achieving a high conversion activity with low-growth-rate cells.

The function of the photoautotrophic compartment (CIV) is the removal of carbon dioxide, generation of edible biomass as food supply, water recovery and the regeneration of oxygen for the crew. This compartment is divided into a photoautotrophic bacteria compartment *Arthrospira platensis*, (CIVa; Vernerey et al., 2001) and a Higher Plant Compartment (HPC or CIVb), thus allowing better $CO_2$ assimilation rates and providing a more balanced diet for the crew. Nowadays a total of 20 higher crops are included in the MELiSSA candidate list, although research on this subject is, as yet, not complete.

## 1.2.2 THE MELISSA COMPARTMENTS

### *1.2.2.1 The liquefying compartment (CI)*

The liquid and solid wastes produced by the crew (i.e faeces, urine, paper), the non-edible output of the higher plant compartment and the non-edible microbial biomass are collected and constitute the feed to this compartment.

The function of this compartment is to transform the waste (polymeric molecules) into ammonium, $CO_2$, volatile fatty acids and minerals as well as $H_2$, whose production will be minimised as far as possible. Due to the need to minimise oxygen consumption in the MELiSSA loop, this degradation is anaerobic. Three main functions are thus expected from this compartment: proteolysis, saccharolysis, and cellulolysis. A general diagram summarising the main steps of an anaerobic biodegration process is shown in Figure 1.3.

The main difference between the MELiSSA CI and a conventional anaerobic system is the interest in inhibiting unwanted methane production in MELiSSA, due to its lack of utility in the MELiSSA loop. In order to minimise methane production, CI is operated at a pH of 6.5 and under termophilic conditions (i.e. 55ºC). Under these conditions, the main products generated are volatile fatty acids (VFA), $CO_2$ and ammonium.

During the early stages of development of MELiSSA, it was expected that, with careful selection, a restricted number of mesophilic bacteria could reach a reasonable level of degradation. However, a percentage of degradation higher than 15% has never been obtained with the bacterial strains *Clostridium thermocellum*, *Clostridium thermosaccharolyticum* and *Coprothermobacter proteolyticus* selected initially. Hence it was decided to extend the number of bacteria and to work with a consortium of autochthonous strains (i.e. isolated from human faecal material).

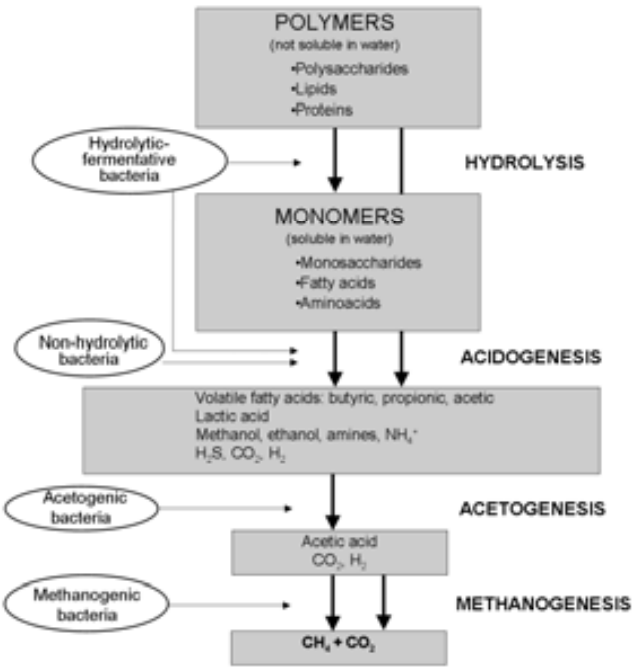


**Figure 1.3** General diagram of the anaerobic digestion process.

The overall biodegradation efficiency achieved with the selected inoculum has significantly improved, values of 70% proteolysis and 44% fibre degradation being achieved. The achievement of yet better degradation results is currently limited by two factors: (i) the very slow degradation of fibrous material (i.e cellulose, xylan, lignin) and (ii) the mechanical difficulty of extracting these non-degraded compounds for a specific and more adapted treatment. The application of further degradation techniques to improve the degration of fibre material is currently under study (subcritical oxydation, fungi, rumen bacteria, hyperthermophilic bacteria).

#### *1.2.2.2 The photoauto/heterotrophic compartment (CII)*

The function of compartment II is the metabolisation of the end products of the liquefying compartment (CI). The main compounds expected in the effluent of CI are listed in Table 1.2. In order to transform these products into biomass under anaerobic conditions, two species of photoheterotrophic bacteria were selected: *Rhodospirillum rubrum*, which carry out the degradation of the organic carbon source and *Rhodobacter capsulata*, responsible for the consumption of $H_2$ and $CO_2$. Sulphide can also be consumed by both *R. rubrum* and *R. capsulata*. However, an important extracellular accumulation of elemental sulphur takes place (Hansen and Gemerden, 1972; Kompatseva, 1981). Therefore, the use of *Thiocapsa roseopersicina* to reduce sulphur to sulphate was required.

The study of the autotrophic growth of both bacterial species revealed that *R. capsulata* grew more rapidly in the absence of an organic carbon source in the medium. Therefore, CII was divided into two independent subcompartments (i.e photoautotrophic and photoheterotrophic compartment) as depicted in Figure 1.4 (Albiol, 1994). Although the $H_2$ production in CI cannot be overlooked, simplification of CII by using only the photoheterotrophic subcompartment (i.e. *R. rubrum* subcompartment) is being considered. Specific studies performed with *R. rubrum* have demonstrated the suitability of this biomass for inclusion in the crew diet at low concentrations.

**Table 1.2** Expected composition of the effluent of the liquefying compartment (Albiol, 1994).

| | |
|---|---|
| **Carbon sources** | Acids acetic, propionic, butyric, isobutyric, valeric, isovaleric, caproic, isocaproic and lactic; Ethanol; $CO_2$. |
| **Nitrogen sources** | Ammonium, urea, uric acid, aminoacids and amines |
| **Other compouds** | $H_2$, mineral nutrients and vitamins |

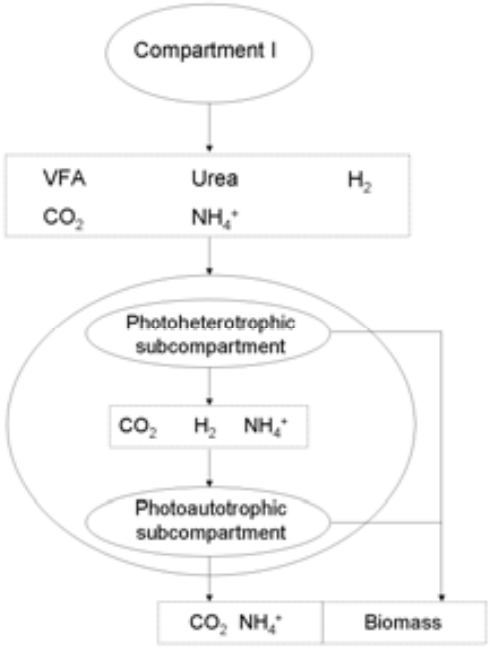


**Figure 1.4** Diagram of the Compartment II subcompartments. Adapted from Albiol, 1994.

### *1.2.2.3 The nitrifying compartment (CIII)*

The main function of CIII is to convert ammonium present in the effluent of CII into nitrate, which is the most favourable source of nitrogen for *Arthrospira platensis* (CIVa) and for the higher plants of the HPC (CIVb). The compartment is colonised by a co-culture of *Nitrosomas europaea* and *Nitrobacter winogradskyi*, which oxidise $NH_4^+$ to $NO_2^-$ and $NO_2^-$ to $NO_3^-$, respectively, using $CO_2$ as carbon source. The work developed in the present thesis is focused on the the nitrifying compartment of MELiSSA. Therefore, a more comprehensive description of this compartment will be provided in further sections of this chapter.

### *1.2.2.4 The photoautotrophic compartment (CIV)*

The photoautotrophic compartment is split into two parts: the compartment colonised by the cyanobacteria *Arthrospira platensis* (CIVa) and the Higher Plant Compartment (CIVb). These compartments are essential for the regeneration of oxygen as well as for the production of food.

**The algae compartment (CIVa)**

This compartment has been the most extensively studied in the MELiSSA project. The aim of this compartment is to produce edible biomass using $CO_2$ originating in other compartments as a carbon source and the nitrate generated in

the effluent of CIII as a nitrogen source. *Arthrospira platensis* was selected in the preliminary stages of development of this compartment as it fulfilled all the requirements: high photosynthetic efficiency, low duplication time, high nutritional value, high digestibility, low contamination risk and no toxic effect. The high nutritional value of *A. platensis* is well documented (Jassby, 1988). Its protein content is similar to the levels found in lactic products and meat, and even higher than in vegetables. In addition, the high content of vitamins A, $B_{12}$ and Fe, as well as amino acids, minerals and other vitamins, contribute to the high nutritional value of *A. platensis*.

**The higher plant compartment (CIVb)**

The incorporation of a higher plant compartment in the MELiSSA loop is aimed at providing a richer and healthier diet for the crew. Like for CIVa, the main functions of the HPC are atmospheric regeneration, water purification and production of edible biomass for the crew.

The activities on this compartment have been initiated with eight crops: wheat, tomato, potato, soybean, rice, spinach, onion and lettuce. Research has been carried out in the MELiSSA project focusing on the description of biomass production rates as well as their mineral compositions. Following the main studies with crops both in open-field and in greenhouses, research has been directed at the design of higher plant chambers (Waters et al., 2004) and their integration in the MELiSSA pilot plant (Waters et al., 2007).

#### *1.2.2.5 The crew compartment (CV)*

The main aim of the MELiSSA loop is to be able to support a crew through the connection of the four compartments described above. An experiment involving connection of the complete MELiSSA loop is foreseen using animals as a test crew. The use of humans has not been considered due to the higher costs and safety issues involved. Therefore, the animals used as a test crew will consume oxygen and produce $CO_2$, while human faeces and urine will be collected externally and introduced into CI instead of using the waste produced by the animals. The details of this phase are still under design.

### 1.2.3 CONTROL SYSTEM IN THE MELiSSA LOOP

The implementation of a controlled life support system based on biological processes requires the development of a control system able to maintain the stability of the loop performance, ensuring the survival of the crew in the main

compartment (CV). The control system implemented in the MELiSSA loop is divided into different levels, constituting a hierarchical structure as shown in Figure 1.5. Level 0 is composed of the process and the local control loops of single process variables (e.g. pH, temperature) while level 1 includes control actions that depend on more than one variable such as the control of biomass concentration in one of the bioreactors. The main function of level 2 is the on-line optimisation of the values of several global process variables and parameters and finally, level 3 makes it possible to design the operation strategy and take decisions according to the objectives achieved in the lower levels. Therefore, the achievement of the global objectives strongly relies on the knowledge acquired locally for each one of the individual compartments and incorporated in the mathematical model. A complete scheme of the control system architecture is presented in Figure 1.6.

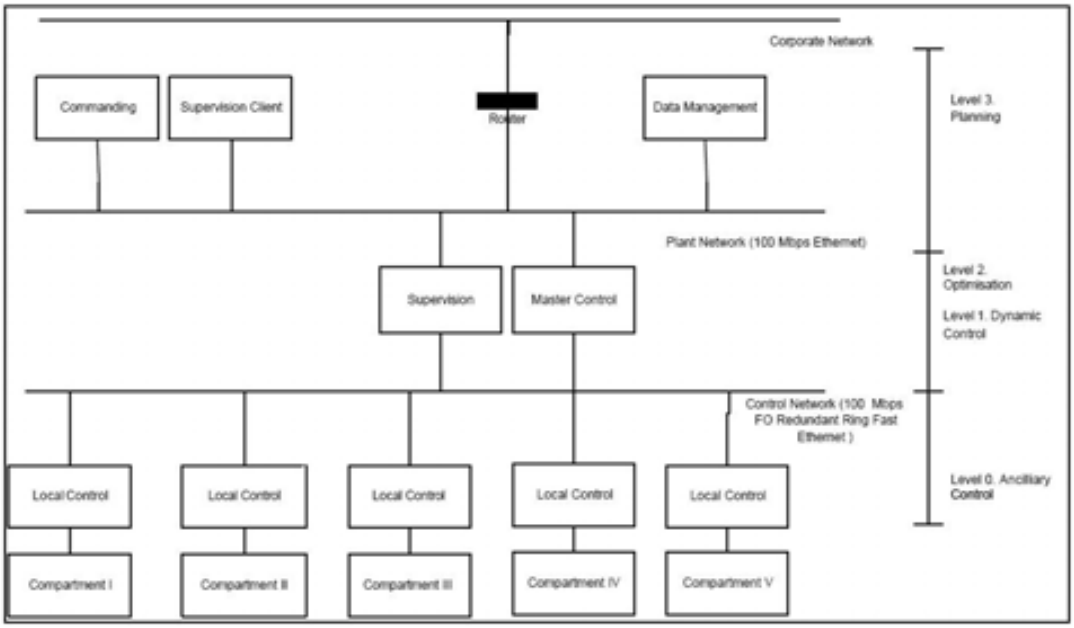


**Figure 1.5** Structure of the control system in the MELiSSA loop.

### 1.2.4 THE MELISSA PILOT PLANT

During phase 1 of the MELiSSA project, each compartment of the loop is analysed separately. Mathematical models are developed for each one of the compartments and subsequent validation is performed with experimental results from batch and continuous cultures. Following basic experimental research and demonstration at bench-scale through simulation, each compartment is scaled-up and integrated in the MELiSSA Pilot Plant (MPP). The MPP, located at UAB, was conceived as a test bed facility in which all the results obtained by the MELiSSA consortium are integrated and the robustness and stability of the continuous

operation of the MELiSSA loop is tested (Gòdia et al., 2004). A layout of the current distribution of the MPP is shown in Figure 1.7.

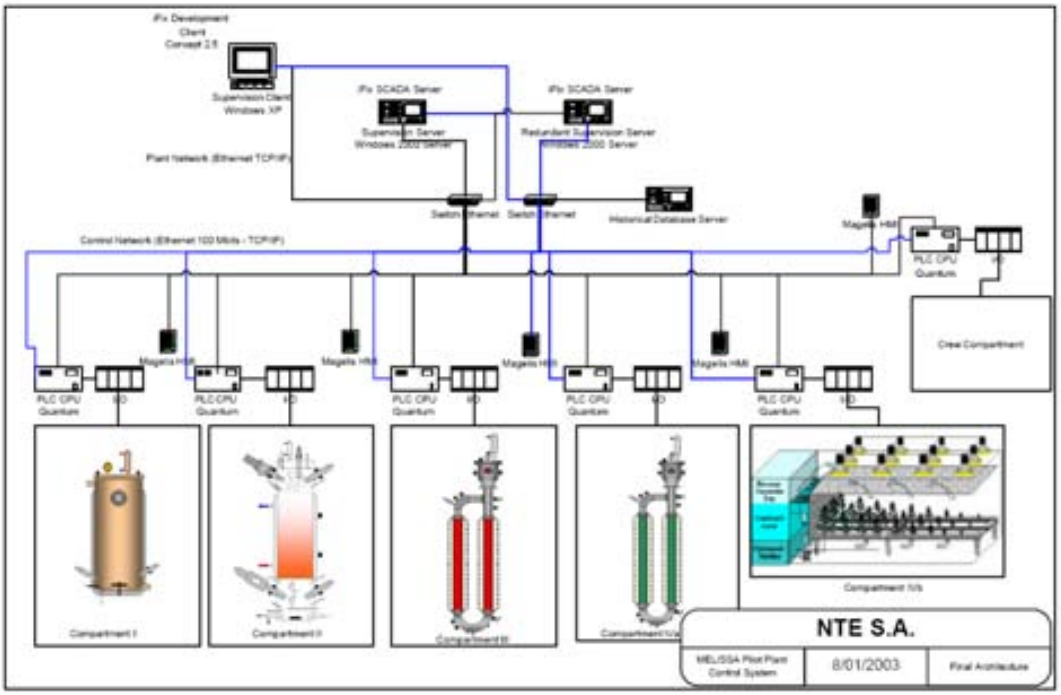


**Figure 1.6** General diagram of the architecture of the control system of the MELiSSA pilot plant.


**Figure 1.7** Layout of the MELiSSA Pilot Plant laboratory at Universitat Autònoma de Barcelona.

The status of the different pilot scale compartments of the MPP is summarised as follows:

- **Compartment I**: installation of CI in the MPP has finalised (Figure 1.8) and testing is under progress. The pilot scale reactor was developed by EPAS (Belgium) and has a total volume of 100L.

**Figure 1.8** Pilot scale reactor of CI (100 L).

- **Compartment II**: This compartment, scaled-up to 50L in 2007, is currently at the end of the detailed engineering phase, which will be immediately followed by construction (Cabello, 2007). Installation in the MPP.is foreseen at the end of 2009.
- **Compartment III:** A packed bed reactor with a total volume of 8 L has been successfully operating during long periods of time, including a 4.8-year period of continuous operation. A detailed description of this compartment is provided in this work. Indeed, the results of this thesis provide the bases of the re-design of this compartment and the construction of an improved bioreactor, which is currently under process.
- **Compartment IVa:** The pilot scale reactor of CIVa has a volume of 77 L (Figure 1.9). Its operation has been exhaustively tested under a wide range of operational conditions. CIII and CIVa were successfully connected at pilot scale in 2000 (Creus et al., 2001; Creus, 2003). Currently this reactor has been improved and the new hardware will be installed in the MPP in April 2009.

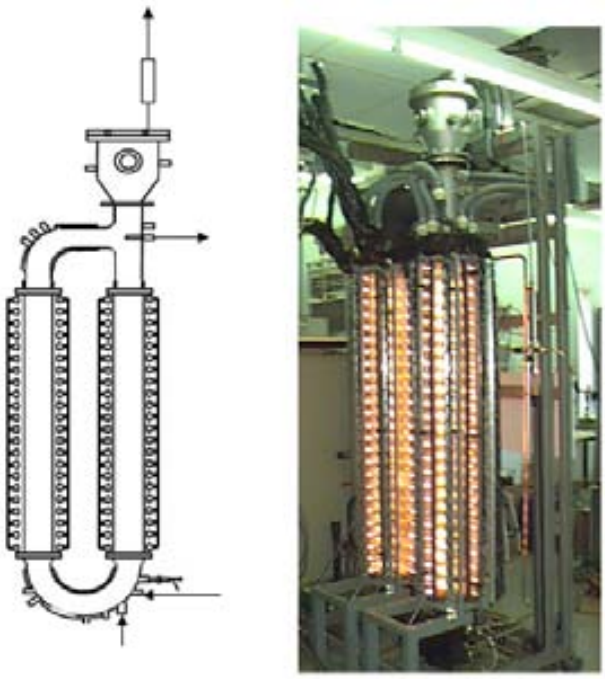

**Figure 1.9** Pilot scale reactor of compartment IVa, with a volume of 77L.

- **Compartment IVb:** the design of the higher plant chambers was finalised (Masot, 2007) and the hardware was built at Guelph University (Canada) and is now in operation at the MPP.

**Figure 1.10** Unit of the Higher Plant Compartment (CIVb) installed in the MPP.

# 1.3 THE NITRIFYING COMPARTMENT OF MELiSSA

## 1.3.1 THE ROLE OF NITRIFICATION IN THE MELiSSA LOOP

As previously mentioned, the function of CIII is the oxidation of the ammonium present in the effluent of CII to nitrate, to be subsequently used in the photosynthetic compartments: CIVa (*Arthrospira platensis*) and CIVb (Higher Plant Compartment, HPP). The ability of cyanobacteria to use different substrates as nitrogen sources, including both ammonium and nitrate, is well documented in the literature (Costa et al., 2001; Carvalho et al., 2004; Soletto et al., 2005; Converti et al., 2006). However, the use of ammonium instead of nitrate as a nitrogen source by *Arthrospira* and other cyanobacteria has also been widely reported to be inhibitory at high concentrations (Converti et al., 2006; Carvalho et al., 2004, Belkin and Boussiba, 1991). The level of ammonium that becomes inhibitory to the cell is different in all these studies and it depends on the type of cyanobacteria and on the operational conditions. The threshold ammonium concentration was found to be 79 mg N-$NH_4^+ \cdot L^{-1}$ for a culture of *Arthrospira* (Masot, 2007). Therefore, a nitrification step is necessary to treat the higher ammonium levels found in the effluent of CII (typically 300-600 mg N-$NH_4^+ \cdot L^{-1}$).

## 1.3.2 THE NITROGEN CYCLE

Nitrogen is an essential element, present in nature in many different forms and states. It is present in the atmosphere in the form of different gaseous compounds, dissolved in the hydrosphere ($NH_4^+$, $NO_2^-$, $NO_3^-$) and as an important component in living organisms as part of the DNA, RNA, proteins or cell tissue.

A natural global nitrogen cycle (Figure 1.11) is established in which nitrogen in its multiple forms is assimilated by biomass and subsequently released again.

All the fluxes involved in the nitrogen cycle are considered to be in steady state. Any alteration of the natural cycle of nitrogen leads to environmental problems such as eutrophication (excess of $NO_3^-$) or presence of NO, $N_2O$ in the atmosphere.

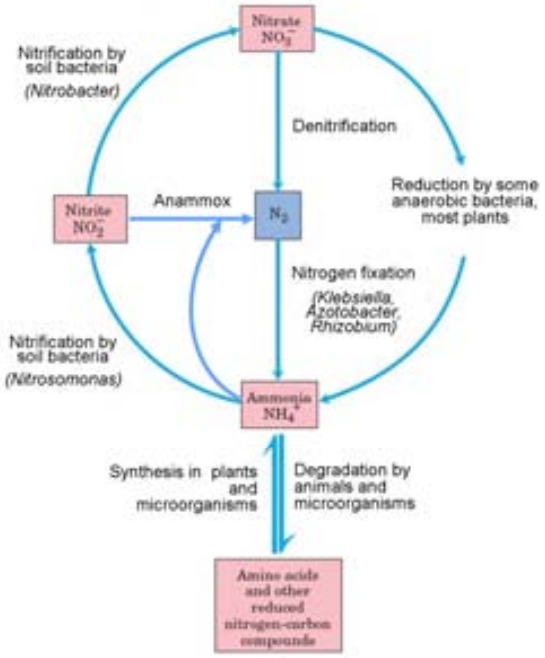


**Figure 1.11** The nitrogen cycle (Adapted from Lehninger et al., 2004).

## 1.3.3 DESCRIPTION OF THE BIOLOGICAL NITRIFICATION PROCESS

Nitrification is a two-step process consisting of two consecutive reactions carried out by two different groups of bacteria: Ammonia Oxidising Bacteria (AOB) and Nitrite Oxidising Bacteria (NOB). The vast majority of the bacteria responsible for nitrification in wastewater treatment systems are chemo-lithoautotrophic bacteria belonging to the *Nitrobacteraceae* group (Bock et al., 1991). This group comprises AOB from the *Nitroso-* group (*Nitrosomonas, Nitrosococcus, Nitrosospira, Nitrosolobus and Nitrosovibrio*) and NOB from the *Nitro-* group (*Nitrobacter, Nitrospina, Nitrococcus and Nitrospira*). The overall stoichiometry of the nitrification is usually represented by the following reactions:

$$NH_4^+ + \frac{3}{2}O_2 \rightarrow NO_2^- + H_2O + 2H^+$$

$$NO_2^- + \frac{1}{2}O_2 \rightarrow NO_3^-$$

### *1.3.3.1 Oxidation of ammonia to nitrite*

AOB carry out the oxidation of ammonia to nitrite through two consecutive reactions. The first one is catalysed by ammonia monoxygenase, an enzyme of the cell membrane (McTavish et al., 1993; Klotz et al., 1997) leading to the production of hydroxylamine ($NH_2OH$) according to the following reaction:

$$NH_3 + 2H^+ + O_2 \xrightarrow{\text{Monoxygenase}} NH_2OH + H_2O \quad \Delta G^o = 17\,kJ{\cdot}mol^{-1}$$

This intermediate product is then oxidised in the presence of hydroxylamine oxidoreductase (an enzyme located in the periplasm; Olson and Hooper, 1983) to $HNO_2$, providing energy for the cells. The catalytic dehydrogenation reaction produces HNO, which is highly unstable and spontaneously yields $HNO_2$ (Anderson and Hooper, 1983).

$$NH_2OH + H_2O \xrightarrow{\text{Hydroxylamin e oxidoreductase}} NO_2^- + 5H^+ + 4e^-$$

A schematic diagram of the electron transport model based on the general scheme proposed for different AOB and based on the model proposed by Bock et al. (1991) is presented in Figure 1.12A. According to this model, two of the four electrons produced in the oxidation reaction are used for the formation of hydroxylamine, while the two remaining electrons would provide the energy to the electron transport chain. It was also observed that under oxygen limiting conditions, these bacteria can produce NO and $N_2O$. The energy released is subsequently used to reduce $CO_2$ through the Calvin cycle (carbon fixation).

### *1.3.3.2 Oxidation of nitrite to nitrate*

The oxidation of nitrite to nitrate is carried out by NOB according to the following reaction, catalysed by the enzyme nitrite oxidoreductase. The substrate is used by NOB in its ionic form, i.e. $NO_2^-$ and oxygen are obtained from water.

$$NO_2^- + H_2O \xrightarrow{\text{nitrite oxidoreductase}} NO_3^- + 2H^+ + 2e^-$$

A simplified diagram of the oxidation metabolism for NOB is shown in Figure 1.12B.Nitrite has a double role in the chemo-lithoautotrophic metabolism, acting both as an electron donor in the oxidative phosphorylation and as an electron acceptor in the synthesis of NADH. The reduction of cytochrome c is thermodynamically unfavourable, thus the energy is low, similarly to AOB, leading to low growth rates of both AOB and NOB. In the particular case of NOB less than 10% of the energy produced is used for growth.

In addition to catalysing the oxidation of nitrite to nitrate, the enzyme nitrite oxidoreductase can reverse its function and reduce nitrate to nitrite under anaerobic conditions (Aleem and Sewell, 1984). Nitrobacter can use pyruvate as an electron donor and nitrate as an electron acceptor in the absence of oxygen.

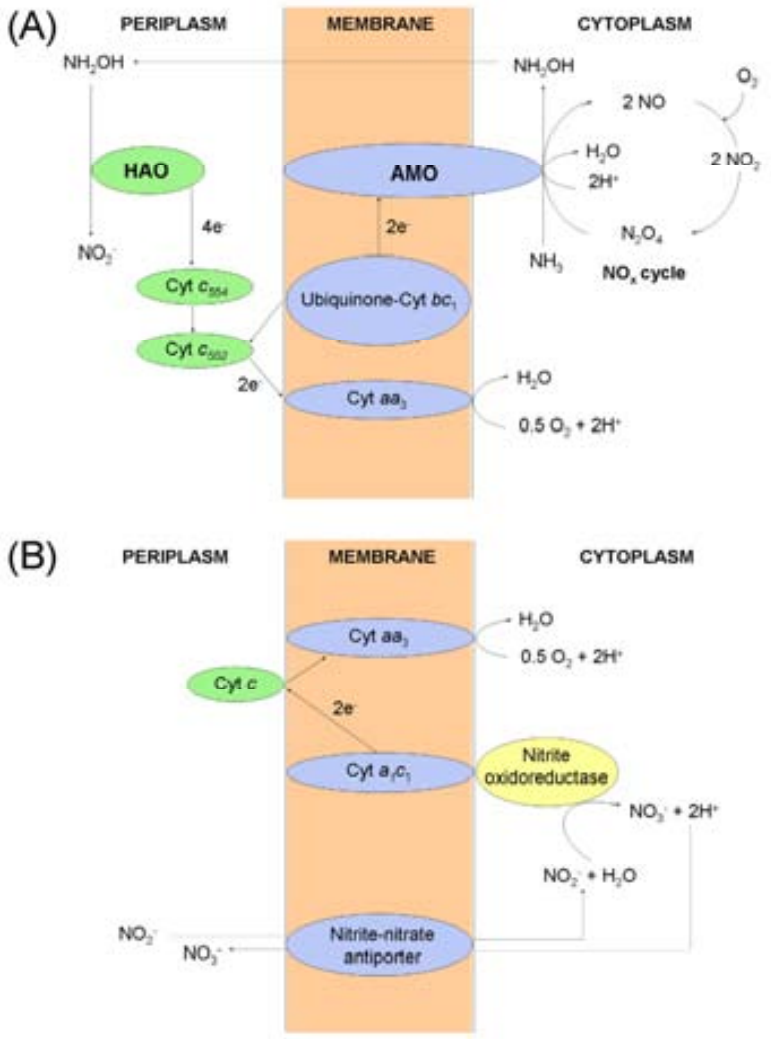


**Figure 1.12** Simplified diagram of the energy metabolism of nitrifying bacteria. (A) Metabolism from $NH_4^+$ oxidation by AOB of the genus *Nitrosomonas*, (B) Metabolism from $NO_2^-$ oxidation by NOB of the genus *Nitrobacter*. Adapted from Bock et al, 1991; Bock and Wagner, 2001 and Costa et al., 2006.

### 1.3.4 LIMITING FACTORS OF THE BIOLOGICAL NITRIFICATION

The main factors having an effect on the biological nitrification processes are listed in Table 1.3. The main limitations as well as the inhibiting effects are listed; they will be described in the following sections. In addition to the intrinsic limitations of the biological process, the limitations due to the use of a biofilm reactor have also been distinguised, due to the relevance of mass transfer processes in systems with immobilised biomass.

**Table 1.3** Summary of the main factors affecting the autotrophic nitrification process. (*) only applicable to a reactor with immobilised biomass.

| Factors affecting autotrophic biological nitrification in a biofilm reactor | |
|---|---|
| **Limitations** | Dissolved oxygen concentration<br>Substrate concentration ($HCO_3^-$, $NH_4^+$, $NO_2^-$)<br>Mass transfer (Gas/Liquid and Liquid/Solid)*<br>Culture conditions (pH, Temperature) |
| **Inhibition effects** | Free Ammonia (FA, $NH_3$)<br>Free Nitrous acid (FNA, $HNO_2^-$)<br>Light |
| **Toxic effects** | Presence of toxic substances |

### *1.3.4.1 Substrate limitations*

- **Limitation by carbon source ($CO_2$):** Under autotrophic growth conditions, the limitation by carbon source is a potential cause of incomplete nitrification (Bazin et al, 1982). $CO_2$ must be supplied to the system in any of its forms (i.e. $CO_2$, $HCO_3^-$ or $Na_2CO_3$) in order to avoid limitation. *Nitrobacter* requires $CO_2$ as a carbon source and will not adapt to other carbon sources in the absence of $CO_2$ (or other carbonate species).

- **Oxygen limitation:** Due to the significant amount of oxygen required by nitrifying bacteria, the effect of oxygen limitation has been broadly studied. The total stoichiometric quantity of oxygen required for nitrification is 4.57 $mgO_2 \cdot mg^{-1}N\text{-}NH_3$. In the absence of limitation by the nitrogen source, the oxygen limitation can be described using Monod-type kinetics. The half-saturation constant of AOB is lower than that of NOB, i.e. AOB have a higher affinity for oxygen than NOB, thus leading to nitrite accumulation at low concentrations (< 0.5-1 mg $O_2 \cdot L^{-1}$) of dissolved concentration (Hanaki et al., 1990b; Tokutomi, 2004).

- **Substrate limitation ($NH_4^+$ and $NO_2^-$):** These two compounds, which are the energy sources of AOB and NOB, respectively, are considered the most relevant limitations on the growth of nitrifying bacteria along with oxygen.

### *1.3.4.2 Physical limitations*

- **pH:** The optimal pH for the growth of nitrifying bacteria ranges between 7.5 and 8.5, although biological nitrification is feasible in the interval of pH 6-10 (Prosser, 1989). The effect of pH can be due to two different causes, one of them leading to inhibition. Low values of pH have a

negative effect on the enzymatic activity, thus slowing down the activity in the cell. In addition, high concentrations of $H^+$ in the medium have an effect on the $NH_3/NH_4^+$ and the $NO_2^-/HNO_2$ equilibria, leading to inhibition by FA and FNA, respectively, as exposed in the following section.

- **Temperature:** The optimal temperature for the growth of nitrifying bacteria bas been narrowed down to the interval 26-30ºC. Temperature has a direct effect on the acid/base and gas/liquid equilibria, affecting the solubility, diffusion coefficients and the enzymatic activity.
- **Mass transfer limitations:** In a biofilm reactor the diffusion of substrates and products, to and from the biofilm needs to be taken into account, in addition to the gas-liquid mass transfer of substrates such as oxygen, which are supplied as gas.

## 1.3.5 INHIBITION OF THE BIOLOGICAL NITRIFICATION

### *1.3.5.1 Substrate or product inhibition*

The actual compounds responsible for the inhibitory effect of $NH_4^+$ and $NO_2^-$ are the compounds $NH_3$ (free ammonia, FA) and $HNO_2^-$ (free nitrous acid, FNA) in equilibrium. In Figure 1.13 the total dissolved concentrations of $NH_4^+$ and $NO_2^-$ have been related to the actual inhibitory concentrations of FA and FNA through the pH (Anthonisen et al., 1976).

Different zones can be distinguished in Figure 1.11 depending on the pH and on the amount of the inhibiting species. Zone 3 defines the optimal zone for nitrification, where inhibition is hardly detected. In zone 2 the growth of *Nitrobacter* is inhibited by FA due to the combination of increasing ammonium concentration and incresing pH. In zone 4 *Nitrobacter* is inhibited by the presence of FNA and finally in zone 1, both *Nitrosomonas* and *Nitrobacter* are inhibited by FA.

### *1.3.5.2 Light inhibition*

One of the main physical inhibitions of nitrification described is the inhibition by light. Prosser (1989) reported a decrease of 50% of the nitrifying activity with a light intensity of 1/3 of the standard daylight. *Nitrobacter* was reportedly more sensible to light than *Nitrosomonas*. It was also demonstrated that the sensitivity of AOB to light is reduced in the absence of oxygen and at high ammonium levels.

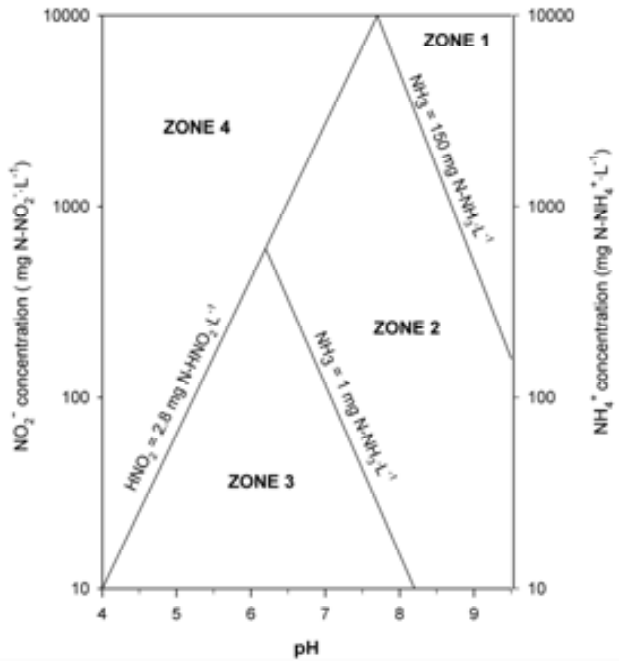


**Figure 1.13** Anthonisen inhibition diagram (Anthonisen et al., 1976). Zone 1: inbihibition of *Nitrosomonas* and *Nitrobacter* by free ammonia (FA); Zone 2: inhibition of *Nitrobacter* by FA: Zone 3: nitrification; Zone 4: inhibition of *Nitrobacter* by free nitrous acid (FNA).

## 1.4 BIOMASS IMMOBILISATION BY BIOFILM FORMATION

### 1.4.1 DEFINITION OF BIOFILM

A biofilm can be described in a simple way as an accumulation of microorganisms at an interface (Gjaltema, 1996) or as accumulation of microorganisms attached to a surface (Wanner et al., 2006). Wilderer and Characklis (1989) proposed a slightly more elaborate definition by describing a biofilm as a layer of prokaryotic or eukaryotic cells anchored to a substratum surface and embedded in an organic matrix of biological origin. However, the designation of biofilm has recently been broadened to include granules, a special type of biofilms that do not require a physical support (i.e. neither a surface, nor an interface are involved in their development). The natural potential of biofilms has often been exploited for biotechnological applications.

### 1.4.2 DEVELOPMENT OF A BACTERIAL BIOFILM

Biofilm development on a support takes place when the combination of several processes (physical, chemical and biological) gives as a net result an increase of the amount of biomass accumulated on the support (Gjaltema, 1996).

Under selected operational conditions in the bioreactor (usually a dilution rate higher than the maximum specific growth rate of the biomass, van Loosdrecht and Heijnen, 1993) the adhesion of the cells to the support is induced, starting the biofilm development.

The process starts with the adsorption of a high number of cells to the support, which will eventually start the active production of extracellular polymeric substances (EPS) thus making cell adhesion stronger than simple adsorption (Boyd and Chakrabarty, 1994). Support coverage develops from here thanks to growth of adhered cells. Finally, once a first layer of biofilm has developed, suspended biomass can also adhere to the biofilm-liquid interface through the process called attachment (Figure 1.14).

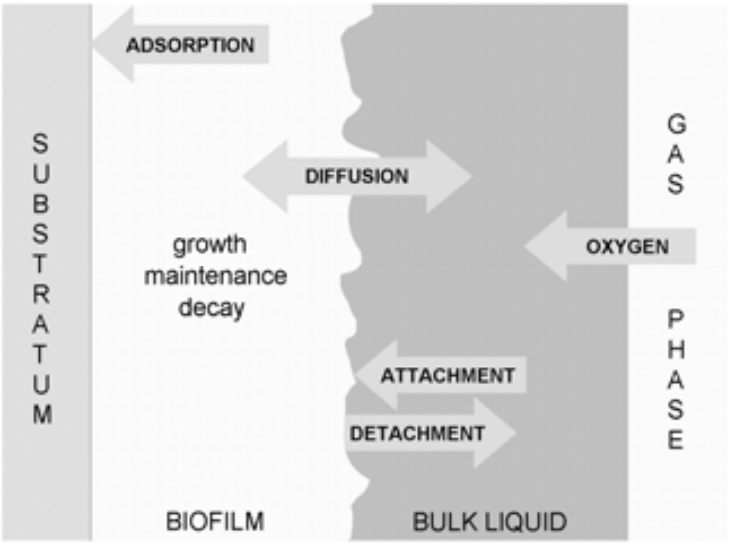


**Figure 1.14** Main phenomena taking place in a biofilm.

Similarly to the adhesion and attachment mechanisms, among the loss processes involved in biofilm development, desorption of cells from the support must be distinguished from detachment of cells and other components from the biofilm, the latter taking place at later stages of the biofilm. Several mechanisms of detachment have been described, all of which contribute to the structure of a mature biofilm and which depend on the hydrodynamic conditions in the bulk liquid of the reactor: (i) erosion, loss of single cells caused by liquid shear; (ii) sloughing, which implies the loss of bigger biofilm pieces or (iii) abrasion, caused by physical contact with other objects and bound to be present in air lift reactor, for instance (Chambless and Stewart, 2007; Morgenroth and Wilderer, 2000).

The biofilm thickness is considered to reach a pseudo steady state once the gain and loss processes are balanced in the biofilm, i.e. the biofilm thickness remains constant. (Morgenroth and Wilderer, 2000).

### 1.4.3 BIOFILM REACTORS

The use of immobilised microorganisms in bioreactors has become a widespread technique and has been widely tested for wastewater treatment applications (Lydmark et al., 2006; Egli et al., 2003; Persson et al., 2002 Fdz-Polanco et al., 2000). Different reactor types and configurations involving biomass immobilisation onto a substratum have been tested: packed bed, fluidised bed, biofilm airlift suspension reactor, etc. A common quality of all the biofilm reactors is the lower volume requirement in comparison to traditional configurations such as a CSTR. The use of a biofilm reactor allows operation at higher retention times without the need for massive volume availability. The immobilisation of biomass on a support makes this reactor the best choice for biomass cultures, such as nitrifying bacteria, with low growth rates, as it avoids wash-out of the cells from the reactor.

## 1.5 THE NITRIFYING PILOT REACTOR: BACKGROUND

### 1.5.1 REACTOR DESCRIPTION AND OPERATIONAL CONDITIONS

One of the main premises of the MELiSSA project is the use of axenic cultures of selected bacterial strains. The use of a well determined population of microorganisms also guarantees that the developed mathematical models provide an accurate picture of the process and no uncertainty is introduced by the presence of other hypothetical biomass populations.

The two strains selected to perform the biological nitrification step in the MELiSSA project were *Nitrosomonas europaea* (American Type Culture Collection, ATCC 19718) and *Nitrobacter winogradskyi* (ATCC 25391). The selection of these strains was based on the fact that these were the most studied strains of nitrifying bacteria.

The low growth rate of nitrifying bacteria, together with the fact that this biomass is not edible, makes of a biofilm reactor the best solution for CIII, as a high efficiency is achieved with a low volume, while the biomass content in the effluent is very low. During the preliminary phases of development of the CIII bioreactor, an assessment was carried out to select the most suitable reactor type (Forler, 1994).

Three reactor types were originally considered: packed bed, fluidised bed and stirred tank. The fluidised bed was discarded due to the expected difficulties anticipated in its implementation under microgravity conditions.

Experiments were subsequently performed in parallel with two axenic cultures using a stirred tank reactor and a packed bed. The ammonium degradation obtained was similar with both reactors. However, the efficiency of the conversion to nitrate was higher in the packed bed. Therefore, a packed bed reactor was adopted as the best option and further experiments were carried out in order to identify the most adequate support material to immobilise the biomass (Zeghal, 1992). The support material selected for the good results obtained was BIOSTYR® (Anjou Recherche, France), spherical polystyrene particles with an average diameter of 4.1 mm.

Following the selection of the support material, the design of the reactor was outlined taking into account not only the limitations of the process itself, but also the limitations introduced by the support material, which cannot be steam-sterilised. The up-flow cocurrent packed bed reactor of CIII consists of three different sections: (i) the bottom part, where magnetic agitation is provided and the homogenisation of the feeding medium and the recirculation takes place; (ii) the central part, where the support particles and the biofilm are confined and which constitutes the actual packed bed; (iii) the top section for gas/liquid phase separation. The bottom and top part of the reactors also provide housing for the different sensors (e.g. pH, dissolved oxygen).

Liquid recirculation towards the bottom section of the reactor was implemented to minimise liquid phase mixing time, while maximising oxygen transfer. In addition, magnetic stirring (400 rpm) was provided at the bottom of the reactor. The values of the main process parameters were as follows: pH=8.1, temperature= 28.0 ± 0.1 ºC. Air was supplied to the reactor by means of a sparger in the bottom section, while oxygen enriched air was added by the control system to maintain a dissolved oxygen set point of 80%. Dissolved oxygen in the culture medium, pH and temperature were measured by means of two on-line probes located at the top and at the bottom of the reactor, whose measurements were averaged by the control system.

The total pressure in the bioreactor was kept lower than 80 mbar. In regular continuous mode operation the reactor is fed with a given amount of $NH_4^+$ and is operated at a constant gas flow rate (usually 3 $L \cdot min^{-1}$). The carbon source for cellular methabolism is supplied to the reactor from the liquid medium as $NaHCO_3$.

The dimensions of the pilot reactor used to perform all the experiments presented in this thesis are presented in Table 1.4.

**Table 1.4** Dimesions of the pilot reactor and theoretical volumes of each one of the sections.

| | Diameter (mm) | Height (mm) | Volume (L) |
|---|---|---|---|
| **Bottom section** | 112 | 150 | 1.48 |
| | 112 | 18 | 0.18 |
| **Central section** | 120 | 475 | 5.37 |
| | 112 | 63 | 0.62 |
| **Top section** | 112 | 50 | 0.49 |
| **TOTAL** | | | **8.14** |

A comprehensive description of the reactor and the main elements of instrumentation are available in Figure 1.15 and Table 1.6

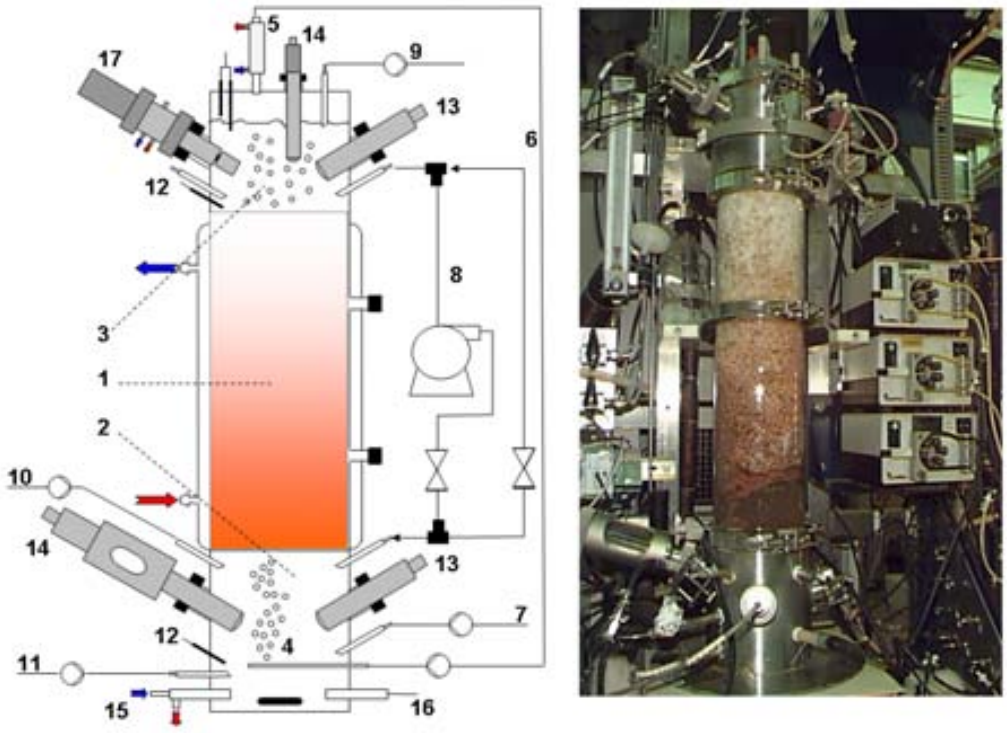


**Figure 1.15 –** Scheme of the hardware of the packed bed pilot bioreactor of compartment III of the MELiSSA (1) Packed-bed section with immobilised culture, (2) bottom section for aeration, liquid distribution and instrumentation, (3) top section for gas disengagement, (4) gas sparger, (5) gas exit condenser, (6) gas loop, connected to oxygen/nitrogen regulated supply to control dissolved oxygen, (7) liquid feed, (8) liquid recirculation, (9) liquid outlet, (10) acid addition, (11) base addition, (12) temperature probes, (13) dissolved oxygen probes, (14) pH probes, (15) cooling system, (16) heating system, (17) sampling device.

### 1.5.2 CHARACTERISATION OF THE REACTOR OPERATION

Following the installation of the pilot reactor of CIII in the MPP, the operation of this reactor was studied in detail Pérez et al. (2004). A physical characterisation of the reactor was carried out by means of Residence Time Distribution (RTD) experiments. The volume occupied by each one of the three phases of the reactor (solid, liquid, gas) was measured and the oxygen mass transfer both in bench-scale and in the pilot-scale reactors was studied in depth.

The nitrification efficiency of the reactor was subsequently assessed under different operational conditions. The nitrification experiments were designed in such a way that they would allow the investigation of the main variables affecting the process, both under steady state and during the transient states following a perturbation in the reactor (Pérez et al., 2004). These experiments also allowed the limits of the reactor operation to be established as further explained in section 1.5.3. Finally, a mathematical model was developed with the aim of gaining experience on the reactor operation under a wide range of operational conditions (Pérez et al., 2005).

### 1.5.3 DEFINITION OF THE LOAD LIMITS

The reactor was operated under a range of ammonium loads between 0.13-1.28 g $N\text{-}NH_4^+ \cdot L^{-1} \cdot d^{-1}$, leading to total conversion rates to nitrate that ranged between 99.6% and 95.3% respectively. The total conversion to nitrate was found to be higher than 99% as long as the incoming ammonium load was maintained below 1 g $N\text{-}NH_4^+ \cdot L^{-1}$ (Table 1.5). Thus, to guarantee an optimal conversion rate, this ammonium load should not be exceeded. Based on these results the range of concentrations and flow rates under normal operational conditions in the reactor are 0.3-0.6 g $NH_4^+ \cdot L^{-1}$ and 3.6-14.4 $L \cdot d^{-1}$.

**Table 1.5** Ammonium loads and corresponding steady states achieved during the testing period of the reactor (Pérez et al., 2004).

| Liquid flowrate ($L \cdot d^{-1}$) | Influent $NH_4^+$ concentration (g $N \cdot L^{-1}$) | Influent $NH_4^+$ load (g $N \cdot L^{-1} \cdot d^{-1}$) | Effluent $NH_4^+$ load (g $N \cdot L^{-1} \cdot d^{-1}$) | Total $NH_4^+$ load oxidation (%) | Effluent $NO_2^-$ load (g $N \cdot L^{-1} \cdot d^{-1}$) | Conversion of $NH_4^+$ load to $NO_2^-$ (%) |
|---|---|---|---|---|---|---|
| 3.6 | 0.3 | 0.13 | $2.3 \cdot 10^{-4}$ | 99.8 | $3 \cdot 10^{-4}$ | 99.6 |
| 6.0 | 0.3 | 0.22 | $8.7 \cdot 10^{-4}$ | 99.6 | $5.2 \cdot 10^{-4}$ | 99.4 |
| 7.2 | 0.3 | 0.27 | $9 \cdot 10^{-5}$ | 99.9 | $2.7 \cdot 10^{-5}$ | 99.9 |
| 14.3 | 0.3 | 0.53 | $8.8 \cdot 10^{-4}$ | 99.8 | $2.7 \cdot 10^{-3}$ | 99.3 |
| 12.7 | 0.6 | 0.94 | $7.9 \cdot 10^{-4}$ | 99.9 | $1.1 \cdot 10^{-3}$ | 99.8 |
| 34.7 | 0.3 | 1.28 | $1.2 \cdot 10^{-2}$ | 99.1 | $4.8 \cdot 10^{-2}$ | 95.3 |

**Table 1.6** Main elements of instrumentation of the pilot reactor of the MELiSSA compartment III. Label numbers refer to Figure 1.16.

| ELEMENT | LABEL | TECHNICAL FEATURES | MODEL | BRAND | ORIGIN |
|---|---|---|---|---|---|
| **Reactor** | | | | | |
| Reactor hardware: top section and lid | 001 | Stainless steel | Custom made | Payra | Terrassa, Spain |
| Reactor hardware: middle section | 002 | Glass | Custom made | Alco | Terrassa, Spain |
| Reactor hardware: bottom section | 003 | Stainless steel | Custom made | Payra | Terrassa, Spain |
| Magnetic stirrer | 004 | 30-1000 rpm | LD-14 | Labinco | Breda, Netherlands |
| Condenser | 005 | Stainless steel, 315 $cm^2$ | | Bioengineering | Wald, Switzerland |
| Air diffuser | 006 | Stainless steel | Not commercial | Not commercial | |
| **Sensors** | | | | | |
| Temperature sensor | 101 | Pt 100 | | | |
| pH sensor: top section | 102 | 12/120, sterilisable | InPro 3000/120 | Mettler Toledo | Urdorf, Switzerland |
| pH sensor: bottom section | 103 | with pressurizable shell | Infit 764-50 Mark I (carcassa) 465 (electrode) | Ingold | Urdorf, Switzerland |
| Dissolved oxygen sensor | 104 | 25/120, sterilisable | 322 Infit | Ingold | Urdorf, Switzerland |
| Level sensor | 105 | 12/60 | Hauser Lindeman | Hauser Lindeman | |
| Pressure module | 106 | 0-1000 mbar | MCR P/UI | Phoenix Contact | Blomberg, Germany |
| PT100 Temperature module | 107 | 4-150 ºC | MCR Pt 100/3/I | Phoenix Contact | Blomberg, Germany |
| pH pre-amplifier | 108 | | 270 I | Ingold | Urdorf, Switzerland |
| pH amplifier | 109 | | 271 | Ingold | Urdorf, Switzerland |
| Dissolved oxygen amplifier | 110 | | 170 | Ingold | Urdorf, Switzerland |
| **Actuators** | | | | | |
| Heating system | 201 | | Not commercial | Not commercial | |
| Cooler electrovalve | 202 | Stainless steel, 220V, 6W | 8263 | ASCO | Sherpenzeel, Netherlands |
| Peristaltic pump for base addition | 203 | 6 rodets | Ismatec | Ismatec | Zürich, Switzerland |
| $O_2$ mass flowmeter / electrovalve | 204 | 500 mL/min | 225-BX | MKS | Andover, MA, USA |
| $N_2$ mass flowmeter/electrovalve | 205 | 20 L/min | 225-BX | MKS | Andover, MA, USA |
| Gas loop electrovalve | 206 | Stainless steel, 220V, 6W | 8263 | ASCO | Sherpenzeel, Netherlands |
| Cooling system | 207 | Stainless steel | Not commercial | Not commercial | |
| **Auxiliary equipment** | | | | | |
| Thermostatic bath | 301 | Temperature control in jacket | TectronBio | Selecta | Abrera, Spain |
| Thermostatic bath (cooler) | 302 | Reactor and condenser refrigeration | Haake | Haake | Karlsruhe, Germany |
| **Liquid circuit** | | | | | |
| Antireturn valve (feed medium) | 401 | Stainless steel, sterilisable | HOKE | HOKE | Creskill NJ / USA |
| Antretun valve (acid/base) | 402 | Stainless steel, sterilisable | HOKE | HOKE | Creskill NJ / USA |
| Filtration unit | 403 | 0.22 | Opticap | Millipore | Bedford, MA, USA |
| Peristaltic pump (feed medium) | 404 | 8 rollers, 4 channels | Regio MS-4/8-100 ISM 827 | Ismatec | Zürich, Switzerland |
| Peristaltic pump (recirculation) | 405 | 6 rollers, 2 channels | Regio MS-2/6-160 ISM 830 | Ismatec | Zürich, Switzerland |
| Peristaltic pump (effluent) | 406 | 8 rollers, 4 channels | Regio MS-4/8-100 ISM 827 | Ismatec | Zürich, Switzerland |
| **Gas loop** | | | | | |
| Antireturn valve | 501 | Stainless steel, sterilisable | HOKE | HOKE | Creskill, NJ, USA |
| $CO_2$ mass flowmeter / electrovalve | 502 | 50 mL/min | 225-BX | MKS | Andover, MA,USA |
| Air compressor | 503 | membrane | KNF | Verder | Leeds, UK |
| Inlet rotameter and manometer | 504 | 0-10 L/min | 1100 | KDG Flowmeters | Sussex, UK |
| Ceramic filter | 505 | | Bioengineering | Bioengineering | Wald, Switzerland |
| Air filter | 506 | 0.22 | Millipore | Millipore | Bedford, MA, USA |
| Ball valve | 507 | Stainless steel | Whitey | Whitey | USA |
| Sterile pipelines | — | DN 6; 1mm. Wall, Stainless steel | Bioengineering | Bioengineering | Wald, Switzerland |
| Non-sterile pipelines | — | Flexible tubing, different diameters | Norprene | Ismatec | Zürich, Switzerland |
| **Analysis loop** | | | | | |
| Ammonium on-line analyser | 601 | on-line potentiometric analysis | A-103 | AQUATEC, S.A. | Barcelona, Spain |
| Nitrate on-line analyser | 602 | on-line potentiometric analysis | N-103 | AQUATEC, S.A. | Barcelona, Spain |
| Gas-liquid phase separator | 603 | | No comercial | Not commercial | Not commercial |
| Peristaltic pump (level control) | 604 | 6 rollers, 2 channels | Regio MS-2/6-160 ISM 830 | Ismatec | Zürich, Switzerland |
| Filter-holder | 605 | sterilisable | Nalgene | Nalgene | Hereford, UK |
| Filter | 606 | Fiberglass, 0.45 | Whattmann | Whattmann | |
| Reference electrode | — | AgCl/Ag , internal reference | 90/02 | Thermo Orion | Witchford, UK |
| Nitrate ion-selective electrode | — | solid state | N-102-41 | AQUATEC, S.A. | Barcelona, Spain |
| Ammonium ion-selective electrode | — | solid state | A-102-47 | AQUATEC, S.A. | Barcelona, Spain |
| Tubs bomba peristáltica | — | sterilisable, different diameters | TYGON R-3607 | Ismatec | Zürich, Switzerland |
| **Control** | | | | | |
| Programmable logic controller | | | P100 Sensycon | Hartman & Braun | Nanterre, France |
| Vertical communication module | | | VCC Sensycon | Hartman & Braun | Nanterre, France |

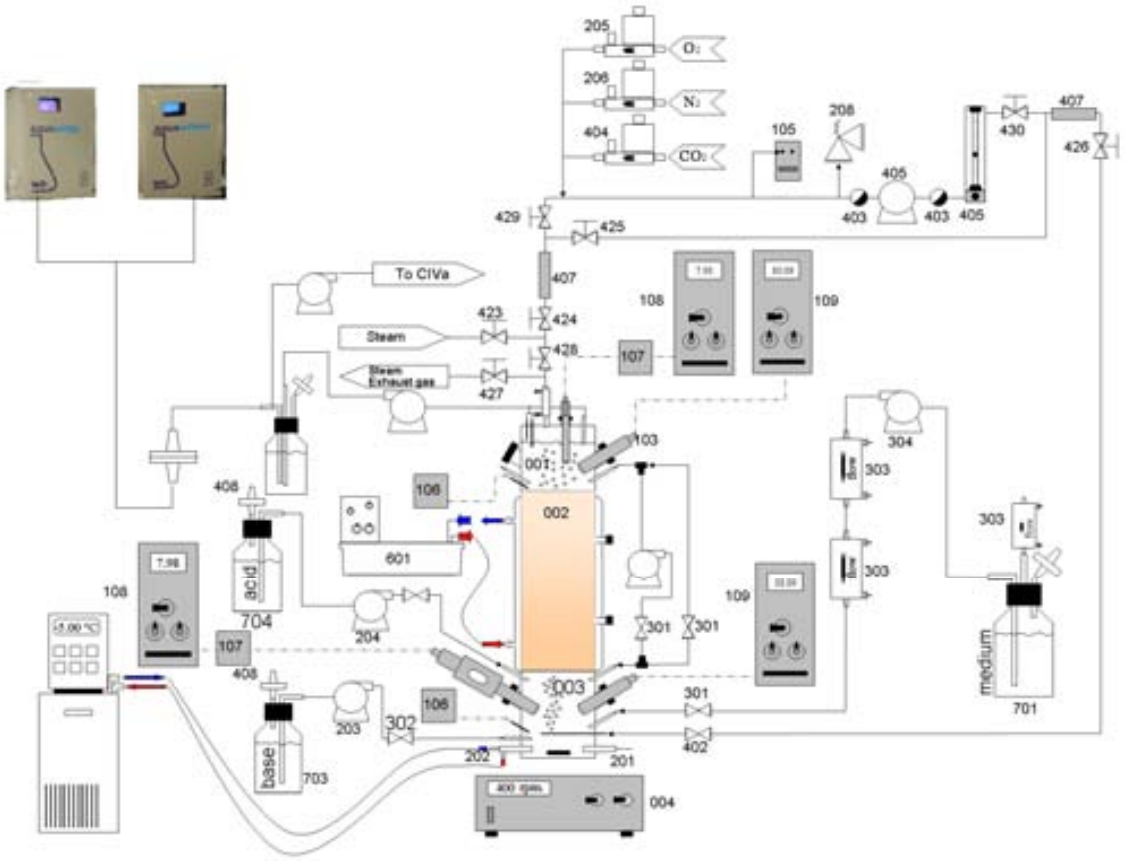


**Figure 1.16** Reactor and main instrumentation of the MELiSSA CIII pilot reactor (adapted from Pérez, 2001). The different instrumentation elements are listed in Table 1.6.

# CHAPTER 2

## THESIS OUTLINE

The main objective of this thesis is to implement the necessary tools to improve the understanding of the nitrifying compartment of the MELiSSA project, thus leading to its optimal performance and stability over long periods of operation.

To attain this final goal, the work has been divided into three main blocks:

- The application of different molecular techniques to assess the composition of the nitrifying biofilm after a long period of continuous operation.
- The development of a mathematical model capable of accurately describing the reactor operation and application of the model to the simulation of different scenarios.
- The development and implementation of an on-line monitoring system for all the nitrogen species in the effluent.

# PART II

# BIOLOGICAL BIOFILM CHARACTERISATION

## CHAPTER 3

### Analysis of the nitrifying biofilm: assessment of the relative abundance of *N. europaea* and *N. winogradskyi* using molecular techniques

# CHAPTER 3

# ANALYSIS OF THE NITRIFYING BIOFILM: ASSESSMENT OF THE RELATIVE ABUNDANCE OF *N. europaea* AND *N. winogradskyi* USING MOLECULAR TECHNIQUES

## *Foreword*

*The autotrophic biofilm from the nitrifying compartment of the MELiSSA pilot plant, initially containing N. europaea and N. winogradskyi, was analysed after 1750 days of continuous operation performing nitrification with an efficiency of close to 100%. Along the packed bed, the total biomass concentration was measured and a gradient of biomass concentration decreasing with increasing height was observed. The general condition and structure of the biofilm was investigated through the analysis of fresh biofilm samples. The presence of Extracellular Polymeric Substances (EPS) was studied using lectin probes labelled with fluorescent dyes to target EPS combined with nucleic acid stains DAPI or SYTO13 to target the bacterial DNA. Fluorescent* in situ *Hybridisation (FISH) coupled with Confocal Laser Scanning Microscopy (CLSM) visualisation was used to detect the two initial bacterial strains at different heights of the packed bed. Quantitative Polymerase Chain Reaction (Q-PCR) was used in combination with FISH to provide quantitative information on the abundance of both bacterial strains, disclosing a spatial segregation of both nitrifiying species along the vertical axis of the packed bed.*

## 3.1 INTRODUCTION

As integrating part of the MELiSSA loop, long term operation under stable conditions is an essential requirement for the nitrifying compartment which is the object of this study. Testing of the pilot scale nitrifying bioreactor in the MELiSSA pilot plant generated essential knowledge on its operation in different scenarios. The liquid phase of the pilot reactor was comprehensively analysed along different operational periods (Pérez et al., 2004). Hence, information about the nitrifiying efficiency of the reactor under a wide range of operational conditions was made available, providing experimental evidence about the load limitations and the response of the reactor to several perturbations that may occur.

Since the reactor was operated axenically, biofilm samples could not be harvested during operation and thus direct monitoring of the biofilm structure development and evolution was not feasible. Simple observation of the packed bed through the glass walls of the reactor provided experimental evidence of a non-homogeneous biofilm along the reactor vertical axis. Biomass concentration was visibly higher near the bottom of the packed bed, while it clearly decreased towards the top of the packed bed (Pérez et al., 2004; Figure 3.1).

Residence time distribution (RTD) analysis performed in the bioreactor indicated a very close to perfectly mixed tank behaviour, with only a slight contribution of plug-flow (Pérez et al., 2004). This small deviation was, however, the cause of the gradient of biofilm thickness along the packed bed, as the characteristic times of the nitrification process were found to be lower than the mixing time estimated through Residence Time Distribution (RTD) analysis (Pérez et al., 2004). A simple mathematical model, which did not take into account the diffusion of substrates into the biofilm, had been developed during previous stages of the reactor characterisation with the main aim of describing the efficiency of nitrification in the bioreactor. When applied to the estimation of biomass concentration, the model already hinted at an accumulation of biomass towards the bottom of the packed bed as well as a possible segregation of *N. europaea* and *N. winogradskyi* in the biofilm. (Pérez et al., 2005). In addition, a segregation of AOB and NOB biofilm populations in similar reactors has already been reported by several authors, both on the microscale along the biofilm thickness (Schramm, 2003; Okabe et al., 1999) and on the macroscale along the flow axis of the biofilm reactor (Noto et al., 1998;

Holben et al., 1998; Lydmark et al., 2006). Although the biofilm structure could not be evaluated during reactor operation, its analysis after termination of reactor operation and dismantling was foreseen to provide useful information regarding the final condition of the biofilm after a long operational period, as will be described in the present chapter. The results contribute to a better understanding and interpretation of long term operation results.

### 3.1.1 APPROACHES TO BACTERIAL COMMUNITY ANALYSIS

The use of molecular techniques has enabled *in situ* monitoring of microbial biofilm communities, not only involving phylogenetic identification but also enabling the determination of spatial distribution and thus leading to relevant conclusions in relation to the biofilm structure. Aoi (2002) reviewed the latest advances and limitations of different molecular techniques focusing on the convenience of the application of these methods to nitrifying biofilms. Fluorescent *in situ* Hybridisation (FISH) was regarded in this study as a highly effective method for the detection of specific bacteria in biofilms and for thestudy of their spatial organisation, emphasizing the possibility to detect specific bacterial cells at single cell level. The efficiency of FISH as a technique for the identification of microbial communities is well reported in the literature, and it has been successfully applied to estimate the proportion of AOB and NOB in biofilms (Persson et al., 2002; Nogueira et al., 2002; Sakano et al., 2002). However, recent studies have exposed some limitations of FISH and proposed solutions to overcome some of them (Wagner et al., 2003; Dorigo et al., 2005).

FISH (Schramm et al., 2000; Lydmark et al., 2006), 16S ribosomal DNA cloning analysis (Okabe et al., 2002) or Real-Time Quantitative Polymerase Chain Reaction (RTQ-PCR) (Kindaichi et al., 2006) have all been recently reported as useful tools to investigate nitrifying bacteria in biofilm systems. The selection of the most suitable method may depend on the final objectives of the study.

The use of FISH coupled with CLSM to study the distribution of bacteria in biofilms is well reported in the literature (Thurnheer et al., 2004; Persson et al., 2002; Nogueira et al., 2002; Sakano et al., 2002). Q-PCR has already proved itself as an important and powerful technique to detect and enumerate bacterial species or groups sharing the same function (Layton et al., 2005; Hermansson & Lindgren, 2001; Nakamura et al., 2006; Kindaichi et al., 2006; Geets et al., 2007). The good performance of this technique to estimate the relative abundance of different populations in biofilms is well reported in the literature (Egli et al., 2003; Silyn-

Roberts et al., 2001; Cole et al., 2004) and, contrary to the FISH analysis, it provides highly accurate quantitative information.

Real time Q-PCR is based on continuous monitoring of fluorescence intensity throughout the PCR reaction. Therefore, this assay is a fast, reliable, sensitive and convenient method to enumerate the relative and absolute abundance of a genus or species in complex multispecies biofilms: this makes it especially suitable for quantifying low abundances of dense microcolony-forming AOB and NOB in biofilms. It is however noted that the real time Q-PCR measures the gene copy number and not the cell number or the biovolume (Kindaichi et al., 2006).

### 3.1.2 ANALYSIS OF THE PRESENCE OF EXTRACELLULAR POLYMERIC SUBSTANCES (EPS) IN BIOFILMS

Microbial biofilms are composed of cellular aggregates as well as containing a large fraction of multipurpose polymers that are essential for biofilm structure, and which have several different roles related to cellular activity (Wingender et al., 1999; Wolfaardt et al., 1999).

Lawrence et al. (1998) found that some lectins with a broad range of carbohydrate specificity were well suited to general staining of exopolymers in biofilms. The use of lectins and probes to target EPS in biofilms has been reported and widely discussed in recent literature (Jin et al., 2005; Staudt et al., 2004; Böcklemann et al., 2002; Strathmann et al., 2002; Wolfaardt et al., 1998). However, in some cases, the specifity of a certain lectin towards a limited number of polymeric compounds might lead to innacurate estimations, making it necessary to use a combination containing different lectins to assess the real content of EPS in a certain biofilm structure, as performed by Jin et al. (2005). In this study the authors tested a combination of several lectins and evaluated their specificities towards different compounds present in the bacterial EPS.

Alternative methods have been proposed by other authors that did not rely on the use of fluorescently labelled lectins. Zhang and Fang (2001) developed a technique based on the staining of bacterial DNA and measurement of the content of volatile solids, assuming that the content of the latter in a biofilm was composed of two main elements: EPS and bacterial cells. However, the use of lectins is a faster and more direct method to detect EPS.

### 3.1.3 PRINCIPLES OF CONFOCAL LASER SCANNING ANALYSIS

Confocal Laser Scanning Microscopy (CLSM) allows direct investigation of microbial species present in biofilms, which can be specifically visualised by means of fluorescent probes (Caldwell et al., 1992). CLSM makes possible the *in situ* observation of the 3D structure of biofilms without interference from out-of-focus objects (Hartmann et al., 1998). Elimination of interference is achieved by focusing the laser beam to a certain confocal plane, so that the highest fluorescence is emitted by this plane and focalised by the objective. As a result an optodigital thin section is obtained that is parallel to the microscopic cover glass (x-y plane) with a thickness approaching the theoretical resolution of the light microscope. A series of 2D (x-y) images perpendicular to the attachment surface (z-direction) can be formed from the scanning object. This series of 2D images can be used to create a 3D reconstruction of the investigated sample (Caldwell et al., 1992). Grey scale images are subsequently enhanced by transformation of the grey level distribution, filtration operations, image calculation operation, object erosion and object dilatation. In a next step the image is converted into a digitised image and is then ready to be automatically processed (Caldwell et al., 1992; Kuehn et al., 1998)

Following image acquisition and image processing, quantification of areas occupied by biofilm cells as a stack of 2D images in biofilms divided into Z-sections makes possible the estimation of the biovolume of the investigated sample. The calculation of the accumulated biovolumes is obtained with a numerical integration algorithm.

## 3.2 OBJECTIVES

The ultimate goal of this chapter is the characterisation of the nitrifying biofilm as a tool to increase the understanding on CIII of the MELiSSA loop. The following partial objectives were defined:

- Evaluation of the biofilm structure using specific stains on fresh biofilm samples followed by CLSM visualisation.
- Assessment of the trends of biomass concentration and biomass distribution along the packed bed through fixation and subsequent molecular analysis of samples obtained after reactor operation shutdown.

- Combination of different molecular techniques to assess the dominance and the possible segregation of the two bacterial strains present in the initial co-culture used to inoculate the nitrifying compartment of the MELiSSA loop.

## 3.3 MATERIAL AND METHODS

### 3.3.1 BIOREACTOR OPERATIONAL CONDITIONS

After inoculation with an axenic co-culture of *N. europaea* (ATCC 19718) and *N. winogradskyi* (ATCC 25391) the nitrifying pilot bioreactor was maintained under continuous operation for a period of 1750 days (4.8 years). During the whole time of operation ammonium conversion was performed with high efficiency (Gòdia et al., 2002; Pérez et al., 2004). The reactor was fed under sterile conditions with different values of ammonium load throughout the operation in order to study the efficiency of the nitrification process. During the last five months of operation the load was kept at 0.22 g $N\text{-}NH_4^+ \cdot L^{-1} \cdot d^{-1}$ (referred to total reactor volume). The composition of the feed can be found in Table 3.1. The effluent was found to contain (on average) 296 mg $N\text{-}NO_3^- \cdot L^{-1}$, 0.07 mg $N\text{-}NO_2^- \cdot L^{-1}$ and 0.16 mg $N\text{-}NH_4^+$, hence a nitrification efficiency of 99% was achieved.

**Table 3.1** Feed composition during the five months preceding reactor dismantling.

| Compound | Concentration ($g \cdot L^{-1}$) |
|---|---|
| $FeSO_4 \cdot 7H_2O$ | $2.5 \cdot 10^{-3}$ |
| $KH_2PO_4$ | 0.680 |
| $NaHCO_3$ | 0.800 |
| $MgSO_4 \cdot 7H_2O$ | 0.052 |
| $CaCl_2 \cdot 2H_2O$ | $7.4 \cdot 10^{-4}$ |
| $(NH_4)_2 \cdot SO_4$ | 1.320 |
| $CuSO_4 \cdot 5H_2O$ | $4.0 \cdot 10^{-6}$ |
| $Na_2HPO_4$ | 0.710 |
| $ZnSO_4 \cdot 7H_2O$ | $4.3 \cdot 10^{-6}$ |
| $(NH_4)_6Mo_7O_{27} \cdot 4H_2O$ | 0.177 |

### 3.3.2 BIOFILM SAMPLING AND PREPARATION

After a period of 4.8 years of continuous operation, the reactor was stopped and dismantled to allow molecular analyses of the biofilm. The packed bed was divided into eight different fractions (henceforth referred to as $F_0$-$F_7$) ascending along the direction of the vertical axis of the reactor (Figure 3.1), $F_0$ being harvested

at a position below the packed bed and $F_1$-$F_7$ at positions located along the vertical axis of the packed bed. The volumes of the different fractions ranged between 250 mL and 1500 mL, and were established taking into account the estimated biomass concentration along the packed bed. Thus, fractions closer to the influent had smaller volumes than the fractions that were closer to the effluent, situated at the top of the reactor.

Since the conditions in which the bioreactor dismantling was carried out were not sterile, the process was performed rapidly and the samples were immediately prepared for storage. Samples from each fraction were processed for molecular analysis and 50 mL of each one of the 8 fractions were stored for future analysis in 15% glycerol at -80ºC after fixation, without altering the biofilm structure. The remaining biomass was subsequently detached from the substratum, lyophilised and used for biomass concentration estimation.

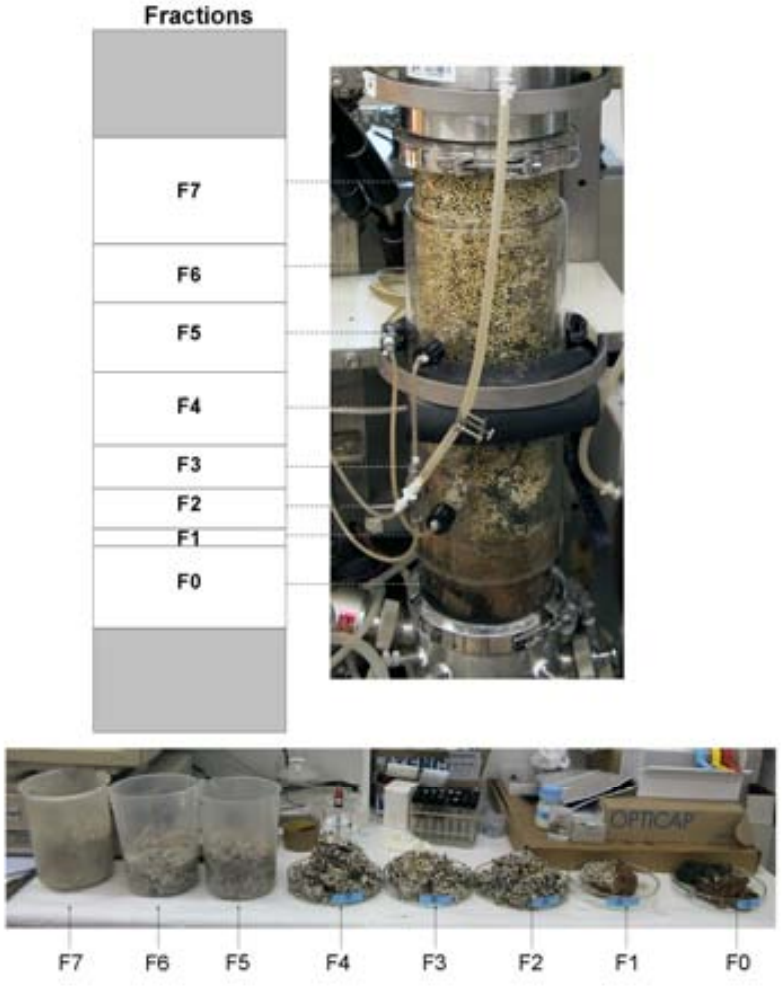


**Figure 3.1** Scheme of the sections ($F_0$-$F_7$) into which the packed bed was divided.

All biofilm samples that were to be stored for future investigation or hybridised with gene probes, underwent paraformaldehyde fixation. In contrast, no fixation was required for those biofilm samples that were immediately used to study the biofilm structure without hybridisation.

### 3.3.3 ANALYSIS OF THE GENERAL CONDITION OF THE BIOFILM

For the general study of the nitrifying biofilm, a small portion of the biofilm (approximately 5 *BIOSTYR*® beads and the corresponding attached biofilm) was collected from each fraction and subsequently washed in a Falcon tube with a 0.01M $MgSO_4$ solution by centrifugation at 6000 rpm for five minutes.

A summary of the protocol followed for the staining and visualisation of the fresh samples used to assess the general condition of the biofilm can be found in Figure 3.2. After washing and within 30 minutes of sampling, cells were stained according to an optimised standard protocol (Strathmann et al., 2002; Wolfaardt et al., 1998) with fluorescent acid stain SYTO13 (Molecular Probes, Inc.) at a concentration of 20 µg $mL^{-1}$. Some of the samples were stained with DAPI nucleic acid stain instead (Molecular Probes, Inc.) at a concentration of 0.3 µg $mL^{-1}$. After 10 minutes at room temperature excess staining was removed by gently rinsing with a 0.01 M $MgSO_4$ solution.

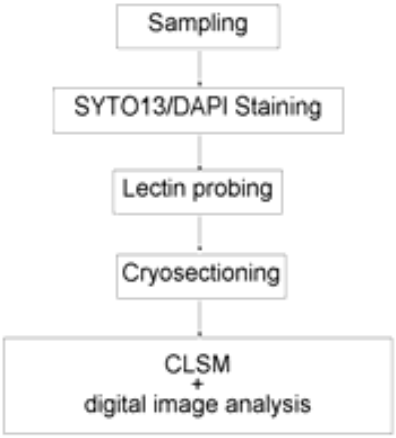


**Figure 3.2** Protocol for analysis of the general condition of the biofilm.

The presence of microbial external polysaccharides (EPS) was visualised by staining biofilm samples with the lectin probe Concanavalin A (Con A)-Texas red (Molecular Probes, Inc.) at a lectin concentration of 5 mg $mL^{-1}$. Excess staining was

removed after 10 minutes at room temperature by gently rinsing with 0.01 M $MgSO_4$ solution.

Prior to cryosectioning samples were resuspended in an appropriate volume of Tissue-Tek OCT embedding compound (Miles Inc., Elkhart Ind., USA) for 15 minutes and immediately frozen at -20ºC for 1 hour to enable slicing of the sample without causing structural damage to the biofilm. Horizontal 10 μm slices of the biofilm were obtained with a cryostat (LEICA Microsystems, Germany) and were subsequently transferred onto gelatine-coated SuperFrost® microscopic slides (Menzel-Gläser, Germany) and immobilised by overnight air drying at room temperature. The microscope slides with the samples were finally stored at 4ºC for up to 2 days.

Before visualisation by means of CLSM slides were mounted in citifluor AF3 antifadent solution (Citifluor Ltd., Canterbury, UK) in order to avoid fading of the fluorescent dyes. One drop of antifadent solution was added to the microscope slide. A random number of samples corresponding to different heights of the packed bed were analysed following this protocol.

### 3.3.4 FLUORESCENT IN SITU HYBRIDISATION (FISH)

For FISH analysis, 16S and 23S rRNA-specific oligonucleotide probes were purchased from MWG-Biotech AG (Germany). FISH probes were labelled at the 5'-end with the following fluorescent dyes: fluorescein isothiocyanate (FITC) and the sulfoindocyanine dyes Cy3 and Cy5. Samples were hybridised with a mixture containing oligonucleotide probes of different specificities. Sampling for the FISH analysis consisted in taking approximately 10 BIOSTYR® beads from each fraction of the packed bed, which were subsequently fixed following the protocol specified below and summarised in Figure 3.3.

From these 10 beads a 10 μm section was obtained by cryosectioning following the protocol described in section 3.3.3 for fresh samples and immobilised onto a microscopic slide for analysis. Since the samples were studied by means of microscopic analysis, the repeatability and accuracy of the results is determined by the area of the fields that were finally submitted to CLSM analysis and the thickness of the biofilm slices (which was constant and equal to 10μm).

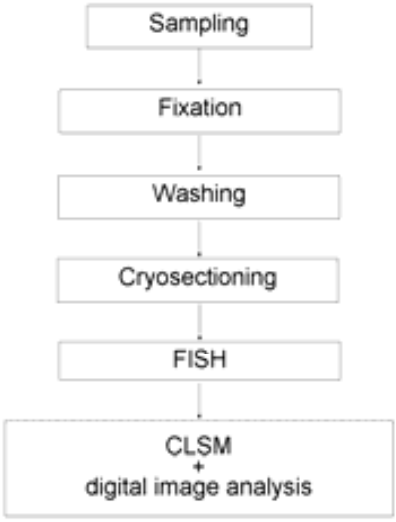


**Figure 3.3** Scheme of the protocol for the FISH analysis of biofilm samples.

### *3.3.4.1 Cell fixation protocol*

Samples were obtained from each fraction of the packed bed and fixed with formaldehyde prior to cryosectioning according to the following the protocol described by Amann (1995).

- Samples are obtained and washed in Falcon tubes with a 1X PBS solution by centrifugation at 6000 rpm for 5 minutes.
- 6 mL of a 4% paraformaldehyde solution are added to each sample and held for 3 hours at 4ºC
- Samples are subsequently washed three times with 5mL of 1X PBS solution (Table 3.2)
- Samples are then stored in 50% ethanol-PBS solution

**Preparation of the phosphate buffered saline (PBS) solution**

The composition of the used Phosphate Buffered Saline (PBS) solutions is specified in Table 3.2. All solutions were prepared using MilliQ water and filter sterilised at 0.45μm. The pH was set to 7.0 with 1M NaOH.

**Table 3.2** Composition of the PBS buffer solutions required in the fixation protocol.

| Compound | 1X PBS ($g \cdot L^{-1}$ MilliQ water) | 3X PBS ($g \cdot L^{-1}$ MilliQ water) |
|---|---|---|
| NaCl | 8 | 24 |
| KCl | 0.2 | 0.6 |
| $Na_2HPO_4 \cdot 2H_2O$ | 1.78 | 5.34 |
| $NaH_2PO_4 \cdot H_2O$ | 0.23 | 0.69 |

**Preparation of 4% paraformaldehyde fixative**

The fixative solution is prepared by adding 10g of paraformaldehyde to 165 mL of MilliQ water previously heated to 60ºC. After dissolving, 2-3 drops of NaOH are added until the solution becomes clear again and finally 3X PBS solution is added up to a total volume of 250 mL and pH is set to 7.0-7.4 using a NaOH solution.

After fixation, samples were resuspended in an appropriate volume of Tissue-Tek® OCT compound (Miles, Elkhart, Ind.) during 15 minutes and immediately frozen at -20ºC for 1 hour. The frozen biofilm samples were cut into 10μm-thick horizontal slices with a cryostat (LEICA Microsystems, Germany) at -20ºC. The obtained biofilm slices were then transferred onto gelatine-coated microscopic slides and air dried overnight to attain immobilisation of the biofilm slices on the microscope slides.

Samples were finally dehydrated by being submerged in a series of 50%, 80% and 98% ethanol-water solutions (3 minutes each), air dried and stored at -20ºC in a moisture-free environment, which was attained by keeping the slides inside a hermetic container until the day the FISH analysis was performed.

### *3.3.4.2 Hybridisation protocol*

Fluorescent *in situ* Hybridisation was performed according to Amann (1995) and following the adapted protocol described by Hugenholtz et al. (2001) for the evaluation of 16S rRNA-targeted probes for FISH.

Hybridisation was carried out for each set of probes at formamide concentrations such that the stringency requirements were fulfilled (Table 3.3). At the beginning of the process the hybridisation oven was pre-warmed to the optimal temperature for hybridisation (46ºC), while hybridisation buffer (Table 3.3) was prepared and mixed with the FISH probes in the appropriate proportion to accomplish the required stringency and a concentration of 50 ng $\mu L^{-1}$ for each of the probes.

To perform the hybridisation, an area of the slide is selected and 90 µL of the probe mixture are extended on it. The slide is subsequently introduced in a moisture chamber, i.e. a 50 mL polypropylene tube containing a folded paper towel (Whatman, 3MM) soaked with 2 mL of hybridisation buffer, in order to prevent evaporation of buffer during hybridisation. The tube is then placed into the hybridisation oven at 46ºC for 2 h.

**Table 3.3** Composition of the hybridisation buffer for the required stringencies.

| Stringency (%) | 5M NaCl (µL) | 1M Tris-HCl (µL) | $H_2O$ MilliQ (µL) | Formamide (µL) | 10% SDS (µL) |
|---|---|---|---|---|---|
| 30 | 180 | 20 | 499 | 300 | 1 |
| 35 | 180 | 20 | 449 | 350 | 1 |
| 40 | 180 | 20 | 399 | 400 | 1 |
| 50 | 180 | 20 | 299 | 500 | 1 |

Hybridisation was stopped by rinsing the probe from the slide with hybridisation buffer prewarmed at 48ºC with a pipette and the slides were then transferred to a new 50 mL Falcon tube containing washing buffer (Table 3.4) at hybridisation temperature which was place in a water bath at 48ºC and incubated for 15 min.

**Table 3.4** Composition of the washing buffer for the required stringencies.

| Stringency (%) | 5M NaCl (µL) | 1M Tris-HCl (µL) | $H_2O$ MilliQ (mL) | EDTA (µL) | 10% SDS (µL) |
|---|---|---|---|---|---|
| 30 | 1020 | 1000 | up to 50 mL | 500 | 50 |
| 35 | 700 | 1000 | up to 50 mL | 500 | 50 |
| 40 | 460 | 1000 | up to 50 mL | 500 | 50 |
| 50 | 180 | 1000 | up to 50 mL | 500 | 50 |

Finally, excess salts were removed by shortly rinsing the slide in ice-cold double distilled water and the slides were subsequently left to dry at room temperature for two hours. Prior to microscopic analysis slides were mounted in citifluor AF3 antifadent solution (Citifluor Ltd., Canterbury, UK) to avoid fading of the fluorescent dyes. A thin film (1 drop) of Citifluor was applied to the slide so that it covered the area on which FISH had been performed and a coverslip was carefully placed on the slide so that the excess of Citifluor could be removed (Hugenholtz et al., 2001).

## 3.3.5 VISUALISATION, IMAGE ANALYSIS AND QUANTIFICATION

### *3.3.5.1 Image acquisition*

A LEICA DM IRE2 inverted Confocal Laser Scanning Microscope (CLSM) by LEICA Microsystems (Germany) was used for image acquisition. The microscope was fitted with a TCS SP2 AOBS confocal laser scanning system. The excitation and emission wavelengths of the fluorescent stains used for the fresh samples as well as the fluorescent dyes used to label the FISH probes are shown in Table 3.5. The 256 grey-scale-level images obtained by CLSM and their corresponding intensity histograms are presented in Figure 3.4.

**Table 3.5** Absorption and emission wavelengths of the used fluorescent dyes.

| Fluorescent dye | Absorption wavelength (nm) | Emission wavelength (nm) |
|---|---|---|
| DAPI | 358 (405nm laser) | 461 |
| SYTO13 | 488 (488nm laser) | 509 |
| ConA-Texas Red | 595 (561 nm laser) | 615 |
| FITC | 488 laser | 518 |
| Cy3 | 550 (561 laser) | 570 |
| Cy5 | 649 (633 laser) | 670 |

### *3.3.5.2 Quantification*

Thresholding is achieved by defining an intensity below which any pixel is assigned an intensity of 0 while the pixels above the threshold are assigned 256 and thus were taken into account to compute the area. The 256 grey-scale-level images obtained with the CLSM (Figure 3.4) for each fluorochrome were converted into binary images by selecting a threshold level below which all grey levels were considered as background. Thresholding was performed manually using the Leica Confocal Software (LEICA, Heidelberg, Germany) as the tool for image analysis. The manual selection of the threshold levels consisted in selecting the lowest intensity detected for each channel, which was attributed to background noise, and setting it as the threshold value.

Although automatic thresholding methods would provide higher reproducibility than manual thresholding, better accuracy is usually obtained by using manual thresholding (Yang et al., 2001).

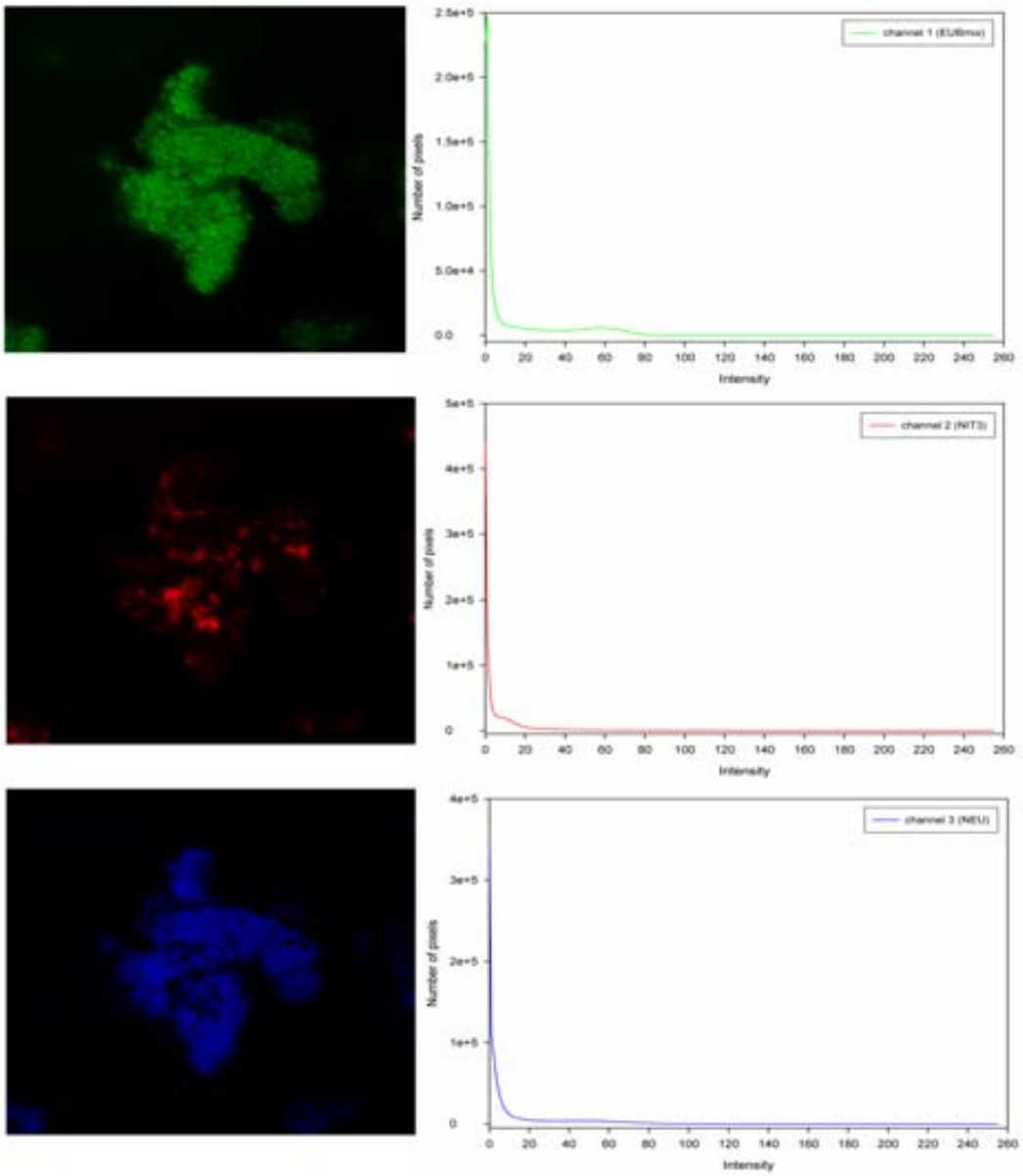


**Figure 3.4** Images obtained by CLSM corresponding to 3 different fluorochromes (green channel: FITC; red channel: Cy3; blue channel: Cy5) and their corresponding intensity histograms. The histograms show the number of pixels counted at each intensity between 0 and 256.

Figure 3.5 shows the images and the intensity histogram obtained after thresholding. All grey levels below the threshold value were considered as background. The threshold was determined separately for the images corresponding to each fluorochrome, which were available as separate image files, for each series of images.

Once the threshold levels were set, it was possible to estimate the area covered by each one of the fluorochromes by counting the number of pixels that were assigned an intensity of 256, i.e. the number of pixels whose intensities were

situated above the threshold value. A histogram can be seen in Figure 3.5 showing the number of pixels with an intensity of 256 for each channel. The area of each section comprising a stack was determined for each fluorochrome (j=1,…3 in this study) and for each scanned section along direction z (i=0,…e) as the area of the pixel (dependent on the CLSM settings) multiplied by the number of pixels ($Np$) above the threshold level set for that particular channel $j$ (Equation 3.1). $A_i^j$ (in $\mu m^2$) is the area of each scanned section across a stack (direction z) for a certain fluorochrome (j). Finally, $Np_i^j$ stands for the number of pixels above threshold level for that particular channel (j) and image.

$$A_i^j = A_{pixel} \cdot Np_i^j \qquad \textbf{3.1}$$

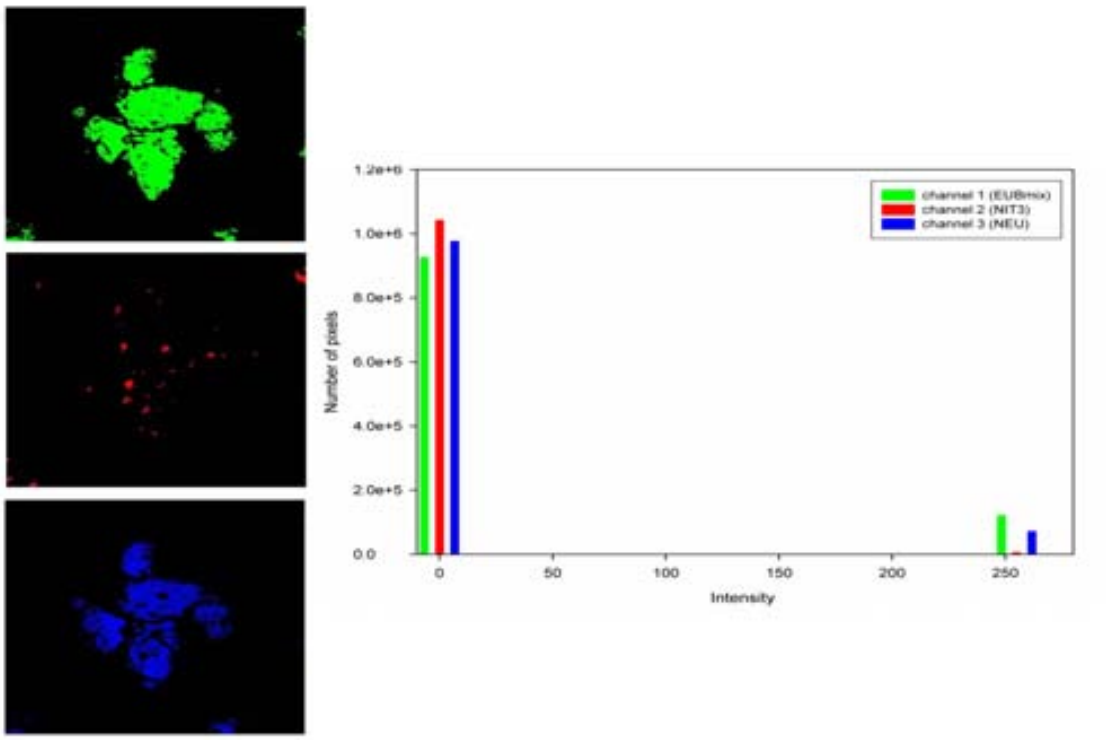


**Figure 3.5** Images obtained by CLSM corresponding to 3 different fluorochromes (green channel: FITC; red channel: Cy3; blue channel: Cy5) after thresholding. The histogram shows how all the pixels have been assigned an intensity of either 0 or 256 according to the selected threshold level.

The values obtained through Equation 3.1 were stored for the subsequent biovolume estimation. The total biovolume of each channel ($V^j$, expressed in $\mu m^3$) was calculated as described by Hendrickx et al. (2004). Through numerical integration across the image stacks (direction z) the volume occupied by the cells stained by each one of the fluorochromes was estimated (Equation 3.2), where $i$ is

the scanning position in the z direction (0<i<e) and e is the number of scanned positions within a stack

$$V^j = \frac{1}{2}\cdot(z_1 - z_0)\cdot A_0^j + \sum_{i=1}^{e-2}(z_{(i+1)} - z_i)A_i^j + \frac{1}{2}\cdot(z_e - z_{(e-1)})A_e^j \qquad \textbf{3.2}$$

## 3.3.6 POLYMERASE CHAIN REACTION (PCR)

Q-PCR assays were performed at the Belgian Nuclear Research Centre (SCK-CEN) using the samples obtained from the packed bed nitrifying bioreactor from the MELiSSA pilot plant.

### *3.3.6.1 Media and growth conditions*

*N. europaea* was cultured in 250 mL of minimal medium (Hyman and Arp, 1992) at 30ºC in a darkened incubator shaken at 100 rpm and *N. winogradskyi* was cultured in the same conditions using a mixotrophic medium (Hendrikus et al., 1993). Three days after inoculation ($A_{600}$ ~0.1) aliquots were taken from the original cultures and the cellular abundance was microscopically determined using a cell counting chamber (W. Screck, Hofheim/Ts., Germany). The enumeration of the *N. europaea* and *N. winogradskyi* cells was performed using a Zeiss Axioscop microscope (Clar Zeiss, Zaventem, Belgium)

### *3.3.6.2 DNA extraction*

Aliquots (25 mL), originating from the same cultures of *N. europaea* and *N. winogradskyi* as those used for microscopical enumeration, were subjected to a phenol-chloroform DNA extraction (Bron and Venema, 1972). The genomic DNA concentration and extract purity were determined after extraction using a Nanodrop® ND-1000 UV-Vis spectrophotometer (Isogen Life Science, Sint-Pieters-Leeuw, Belgium). The genomic DNA was diluted with sterile MilliQ water to 10 ng·μL$^{-1}$ and divided into aliquots that were stored at -20ºC until Q-PCR analysis was performed. From these 10 ng·μL$^{-1}$ stock, 10-fold serial dilutions were prepared and used immediately as the standard for the Q-PCR analyses.

Biofilm material originating from the packed bed bioreactor was stored in 15% glycerol at -80ºC until the phenol-chloroform DNA extraction was performed. The total genomic DNA concentration and purity were determined as described above with all the extracts being subsequently diluted to 7 ng·μL$^{-1}$ and stored at -20ºC until the Q-PCR analysis. Prior to analysis, the total genomic extracts were diluted twice

in 10-fold serial dilutions to reduce the concentration of potential inhibitory compounds in the nucleic acid extracts.

#### *3.3.6.3 Primer design*

16S rRNA gene-targeting primers were designed for *N. europaea* and *N. winogradskyi* using ARB's jan/03-database (Ludwig et al., 2004) in combination with the Primer3-program (http://frodo.wi.mit.edu/cgi-bin/primer3/primer3_www.cgi). With ARB, a specific probe was constructed for either *N. europaea* or *N. winogradskyi* and subsequently used as a primer. The second primer was generated using Primer3, in combination with the probe yielded with ARB. The *N. europaea* 16S rRNA gene targeting-primers were Neu1265F 5'-GCCAATCTCAGAAAGCAC- 3' and Neu1422R 5'-TCTGGTGAAAACCACTCC-3', yielding a 158 bp fragment; and the primers targeting the *N. winogradskyi* 16S rRNA gene sequence were Nwi70F 5'-GGCGTAGCAATACGTCAG and Nwi165R 5'-ATCCGGTATTAGCCCAAG-3', yielding a 96 bp fragment.

#### *3.3.6.4 Q-PCR assay*

The Q-PCR was performed using an Applied Biosystems 7500 Fast-Real Time PCR System (Applied Biosystems, Lennik, Belgium) with the Eurogentec Q-PCR MasterMix for SYBR®GreenI (Seraing, Belgium) in 25 µL reaction mixture with 5 µL of DNA-extracts and 600 nM of forward and reverse primer, following the manufacturer's instructions for the Standard 7500 run. The amplification program was as follows: 2 min at 50°C and 10 min at 95°C, followed by 40 cycles of 15 s at 95°C and 1 min at 60°C (with data collection at this point). A dissociation stage was added after the 40 cycles, with 15 s at 95°C, and 1 min at 60°C, followed by 15 s at 95°C. The genomic DNA standards, the samples and the non-template controls were treated similarly and were all performed in triplicate. The raw data were analysed using the Applied Biosystems' Sequence Detection Software, version 1.3. To determine the relative presence of both micro-organisms, the Q-PCR signals were compared in a 1:1 ratio, as both nitrifiers only carry a single copy of the 16S rRNA gene per genome (Chain et al., 2003; Starkenburg et al., 2006).

# 3.4 RESULTS AND DISCUSSION

## 3.4.1 GENERAL CONDITION OF THE BIOFILM

### *3.4.1.1 Biomass concentration*

The profile of total biomass concentration along the packed bed was assessed by means of dry weight analysis of each one of the eight fractions into which the contents of the reactor had been divided after reactor shutdown (Figure 3.6).

The porosity of the packed bed was estimated by experimentally measuring the void fraction left by the BIOSTYR® beads with respect to the total reactor volume after the biomass had been separated from the support beads. The porosity (0.39 mL void· $mL^{-1}$ packed bed) was used to estimate the total volumes of each one of the eight fractions, which were subsequently used to calculate the total biomass concentration (dry weight) to total fraction volume (Figure 3.6).

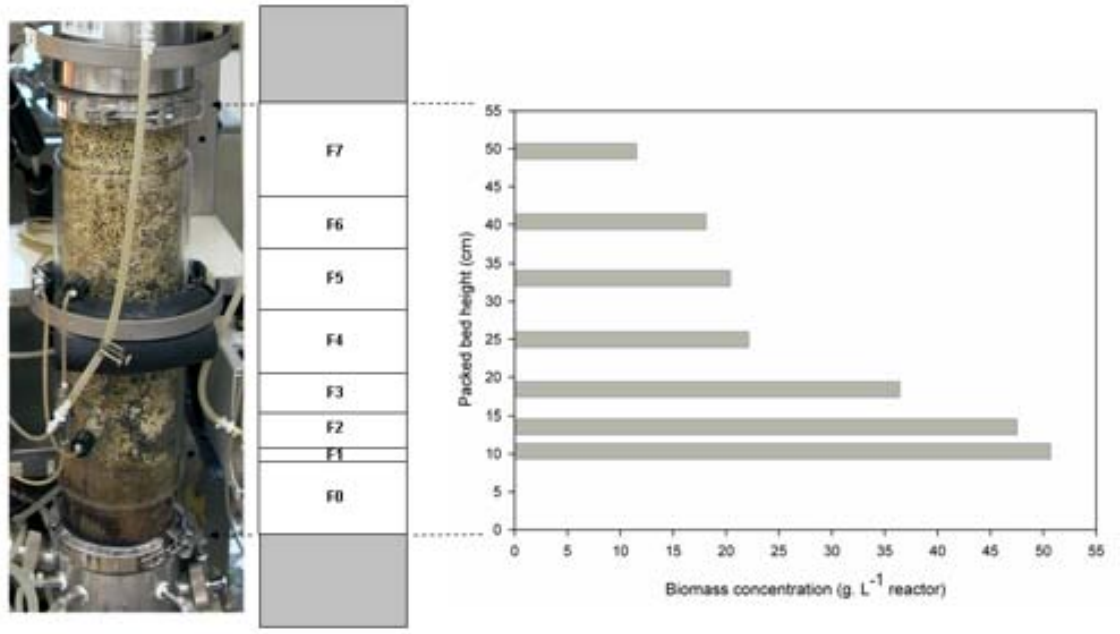


**Figure 3.6** Biomass concentration in packed bed as a function of the position along the vertical axis, experimentally estimated after reactor dismantling. Reactor height is expressed as the average height of the packed bed fraction from which the samples were obtained.

The results (Figure 3.6) confirmed that a clear biomass accumulation took place at the bottom part of the reactor, where the substrate was fed, leading to a heterogeneous distribution of the biofilm throughout the packed bed. This concentration profile was in agreement with previous experimental observations (Pérez et al., 2004) as well as with the predictions made by a mathematical model (Pérez et al., 2005). Biomass accumulation near the feeding point has also been

reported by other authors for reactors with similar configurations (Persson et al., 2002). Pérez et al. (2005) carried out an exhaustive study allowing the identification of the factors contributing to this gradient of the total biomass concentration, and suggesting a cause for this biomass accumulation. The gradient was found to be linked to the characteristic times of the different dynamic processes taking place in this reactor i.e. mixing time, nitrification rate (involving reaction rate as well as diffusion processes) and growth rate of the two bacterial species performing the conversion of ammonia to nitrate. The authors also performed an estimation of characteristic time of the nitrification process based on literature data for the kinetic and diffusion parameters, and on experimental data about the operational conditions in the reactor. They found that the mixing time derived from the RTD experiments was higher than the estimated characteristic time for nitrification in most of the cases, suggesting that the former was controlling the process, leading to a profile of decreasing biomass concentration with height

#### *3.4.1.2 Assessment of the general biofilm structure. Presence of External Polymeric Substances (EPS)*

The general condition of the biofilm was analysed using general nucleic acid stains DAPI or SYTO 13 to target the cellular DNA, while the fluorescent lectin probe *Canavalia ensiformis* (ConA), labelled with Texas-Red, was used to target EPS.

A qualitative analysis of the CLSM images presented in Figure 3.7 shows the presence of EPS close to the DAPI or SYTO 13 targeted bacterial cells. These observations are in agreement with results described by other authors in biofilms of similar characteristics. Staudt et al. (2004) observed that the vast majority of the detected EPS in chemoautotrophic biofilms was found to be in contact with bacteria, while bacteria and EPS were organised in clusters in the case of heterotrophic biofilms. This is in agreement with the results presented in Figure 3.7, in which the red stained areas corresponding to the Texas-red labelled ConA lectin are found to be attached to the bacterial biomass.

The results obtained after quantification of CLSM images of several random samples obtained at different heights of the packed bed are shown in Figure 3.8. A slightly lower presence of EPS close to the bottom part of the reactor, i.e. the feeding point, can be observed. However, the percentages measured in fractions $F_2$, $F_4$, $F_5$, and $F_7$ (heights comprised between 12 and 50 cm) did not indicate a clear trend of the EPS ratio along the packed bed. Taking into account all the different

analysed samples randomly selected from different locations of the packed bed, and averaging the quantification results obtained for each of the samples, an estimated overall value of 18% (biovolume) EPS was obtained.

Results obtained in terms of EPS/cellular material abundance (Figure 3.8), are not in agreement with the observations of similar studies reported in the literature (Staudt et al., 2004). These authors studied the structure of multispecies biofilms originated from an enriched activated sludge culture by CLSM visualisation.

SYTO 60 nucleic-acid specific stain was used to target the bacterial cells and EPS was determined using the lectin of *Aleuria aurantia*. Staudt et al. (2004) observed a high presence of EPS in the chemoautotrophic biofilms, the EPS content in most biofilms being higher than the bacterial cell volume, which is not comparable to the values obtained in the present study. In addition, Zhang and Fang (2001) reported that the presence of EPS increases notably in mature biofilms, accordingly a high proportion of EPS should be expected in this nearly 5-year old biofilm.

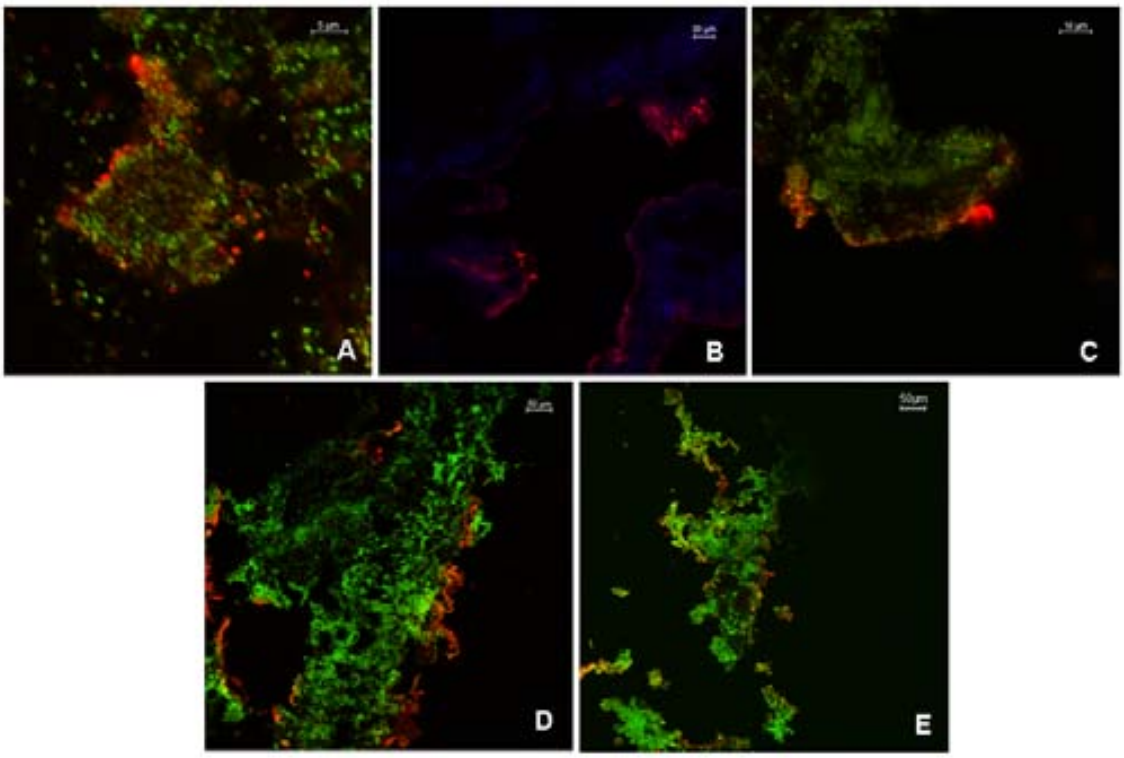


**Figure 3.7** CLSM images corresponding to 5 different heights of the packed bed: EPS (red, ConA-Texas Red) and cellular DNA (green, Syto13). (A) fraction F0; (B) fraction F2; (C) fraction F4; (D) fraction F5; (E) fraction F7.

Different hypothesis can be advanced to explain these results. First of all, the use of a single lectin (ConA) to target the EPS may have led to an underestimation of the total EPS abundance, which would have been misleading in the assessment

of the structure of the biofilm based on these results. The lectin ConA has been reported to bind specifically to mannose and glucose residues of polysaccharides (Jin et al., 2005). It is very likely that the analysed biofilm had a high presence of different polymeric substances other than those detected by ConA, thus leading to an underestimation, which would explain why certain scanned areas of the biofilm appear unstained in the CLSM images Figure 3.7. It is also possible that the EPS production might suffer alterations in such an old biofilm, leading to a lower production of polymeric substances due to the lower ammonium loads applied in the latest stages of operation before the reactor was stopped.

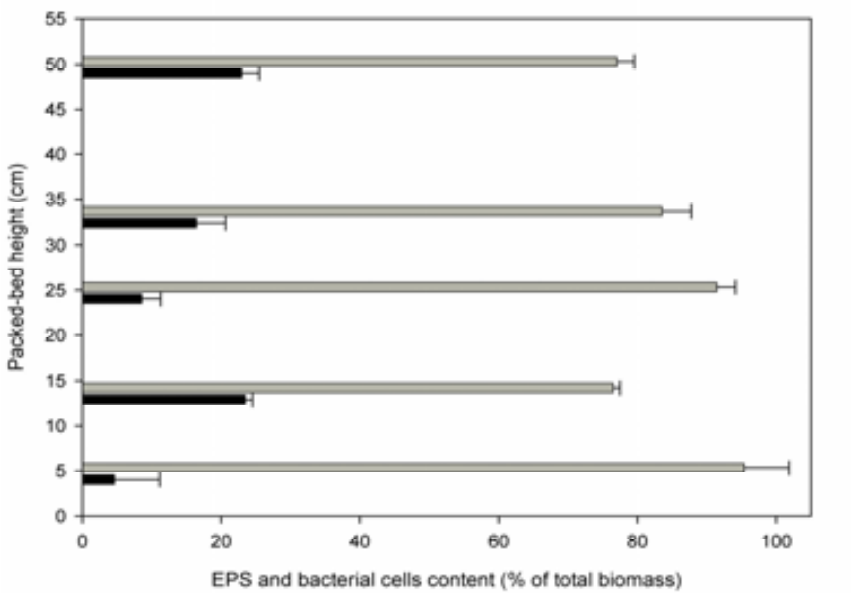


**Figure 3.8** EPS content along the height of the packed bed as depicted by ConA-Texas Red labelled lectin (black bars) and bacterial cells content as depicted by SYTO 13 and DAPI nucleic acid stains (grey bars).

## 3.4.2 INITIAL EVALUATION OF THE MICROBIAL DIVERSITY OF THE NITRIFYING BIOFILM

The reactor was operated axenically, and its nitrification efficiency was close to 100% during the whole period of operation. Nevertheless, contamination of the co-culture with other bacterial species, although not compromising the stability of the reactor, almost certainly occurred.

### *3.4.2.1 Assessment of the diversity of bacteria in the packed bed*

In order to guarantee that *N. europaea* and *N. winogradskyi* were the sole AOB and NOB, respectively, in the reactor the diversity of bacteria in the biofilm was investigated. After the absence of other AOB and NOB in the biofilm was assessed,

molecular analyses could be performed with the purpose of obtaining quantitative information on the relative abundance of the two initial strains.

The microbial community of the biofilm was analysed using PCR-based detection coupled with denaturing gradient gel electrophoresis (DGGE) targeting the 16S rRNA genes of several bacterial groups or bacterial species. The latter were selected because of their common occurrence in wastewater treatment plants and reactors treating water with an important content of ammonium or nitrite (Schramm et al, 1996; Dionisi et al., 2002; Siripong and Rittmann, 2007).

PCR- and DGGE-analyses were performed on samples from all fractions of the packed-bed reactor with the following targets: (i) *β*–proteobacterial AOB, (ii) *Nitrobacter* sp. And (iii) *Nitrospira* sp. The remaining taxa of ammonia- and nitrite-oxidizing micro-organisms were not targeted because of their specific ecophysiological properties, being either aerobic strains which occur in marine or saline environments (e.g. *Nitrosoccoccus oceani*, *Nitrococcus mobilis*, *Nitrospina gracilis*), or strictly anaerobic strains (e.g. anaerobic ammonia-oxidizing *Planctomycetales*) (Watson and Waterbury, 1971; Koops et al., 1990; Mulder et al., 1995; Van de Graaf et al., 1995). It is important to note that the ammonium, nitrite and nitrate measurements of the influent and effluent showed no evidence of denitrification or ammonia-assimilation in the reactor; hence, denitrifying activity or ammonia-assimilation by heterotrophic bacteria or coupled nitrification-denitrification by anammox could be neglected. Thus, as no members of the *β*-proteobacterial AOB other than *N. europaea* and no NOB other than *N. winogradskyi* were detected, Q-PCR analyses of reactor samples could be performed.

The presence of *N. europaea* in reactor samples harvested from eight different heights of the reactor ($F_0$-$F_7$) was investigated by targeting the β-proteobacterial AOB with different PCR primers following the protocols described by Kowalchuk et al., 1997. The PCR-products were separated with DGGE on an 8% acrylamide gel with a 45% - 60% denaturing gradient. In Figure 3.9 only two bands are observed in the lanes where the reactor samples were injected, which corresponded with the *N. europaea* positive control (lane 1) thus confirming the presence of *N. europaea* in all samples. *Nitrobacter* species bacteria were targeted using the FGPS-primers according to Degrange & Bardin (1995). After performing the PCR the products were again separated by DGGE as described above. In all packed bed fractions ($F_0$-$F_7$) only one band was observed which corresponded to the *N. winogradskyi* positive control and which differed from the band generated by the *Nitrobacter hamburgensis* negative control (Figure 3.10).

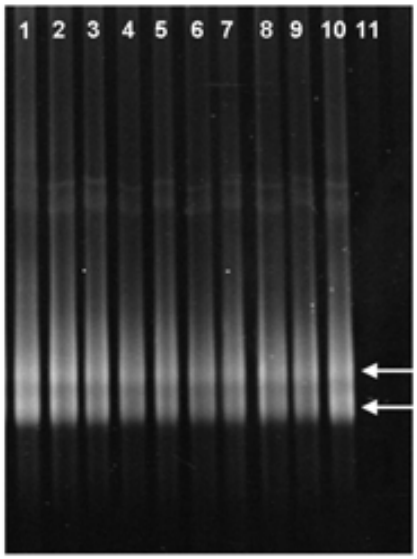


**Figure 3.9** Lane 1: Positive control (*N. europaea* ATCC 19718), Lane 2 – 9: Reactor samples $F_0$ – $F_7$, Lane 10: Positive control (*N. europaea* ATCC 19718), Lane 11: Negative control (sterile MilliQ water).

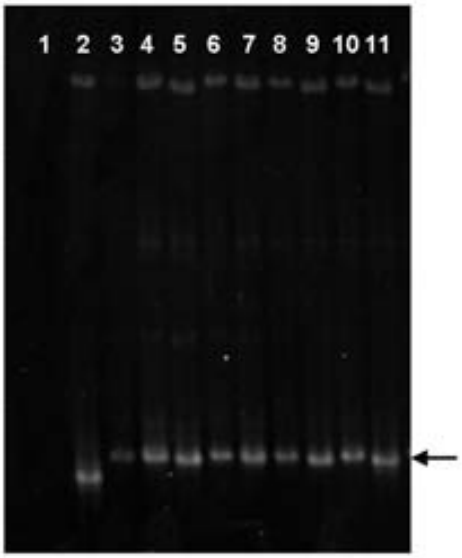


**Figure 3.10** Lane 1: Negative control (sterile MilliQ water), Lane 2: Negative control (*Nitrobacter hamburgensis*), Lanes 3 – 10: Reactor samples $F_0$ – $F_7$, Lane 11: Positive control (*N. winogradskyi* ATCC 25391).

Finally to investigate the presence of *Nitrospira* sp. PCR was performed using the NSR- genus specific primers as described by Dionisi et al., 2002. The resulting 1.2% agarose gel electrophoresis, depicted in Figure 3.11 shows no amplification for any of the reactor samples ($F_0$-$F_7$) that matches the strong signal yielded by the positive control, thus confirming *N. europaea* and N. *winogradskyi* as the only AOB and NOB present in the reactor samples.


**Figure 3.11** Lane 1: Fermentas GeneRuler™ 100 bp DNA Ladder, Lane 2: Positive control (*Nitrospira* sp.), Lane 3: Negative control (*N.r winogradskyi* ATCC 25391), Lane 4: Negative control (sterile MilliQ water), Lane 5 – 12: Reactor samples $F_0$ – $F_7$, Lane 13: Positive control (*Nitrospira* sp.), Lane 14: Negative control (*N. winogradskyi* ATCC 25391), Lane 15: Negative control (sterile MilliQ water), Lane 16 : Fermentas GeneRuler™ 100 bp DNA Ladder.

The fact that *N. europaea* and *N. winogradskyi* remained the only nitrifying strains in the biofilm after 1750 days of continuous operation, provided evidence of the stability of long term reactor performance of the MELiSSA nitrifying compartment.

### 3.4.3 FISH ANALYSIS OF THE NITRIFYING BIOFILM

To evaluate the dominance of the nitrifying species originally introduced in the bioreactor (*N. europaea* and *N. winogradskyi*) a number of samples obtained at different heights of the packed bed were subjected to FISH-CLSM analysis. Samples were hybridised with a mixture containing up to three different probes with different specificity towards the bacteria present in the sample. The relative amounts of the targeted groups of bacterial species were calculated as percentage of the total eubacterial biomass.

Interference caused by auto-fluorescent material was discarded prior to performing the FISH analysis by treating some samples from the reactor with the fixation protocol and subsequently visualising them through CLSM. Special care was necessary in determining the most adequate stringency for all the different probe combinations used. However, the complexity of biofilm samples makes it difficult to foresee all the possible factors related to its structure that may have an influence on the efficiency of the analysis. In addition, the number of biofilm samples available for FISH analysis after fixation and cryosectioning was limited in this study.

In order to obtain reliable quantitative information on the analysed samples through FISH and CLSM analysis, a great number of samples would be necessary for statistical reasons. The limited amount of samples available for analysis, together with the wide range of probe combinations needed for a comprehensive evaluation of the biofilm at different heights (Figure 3.12), led to the decision to use the FISH analsysis mainly as a tool to qualitatively assess the dominance of the two initial bacterial strains in the biofilm and to visualise their segregation along the packed bed. Q-PCR was performed next in order to provide the accurate and reliable quantitative information on the relative abundance of the *N. europaea* and *N. winogradskyi* that this study would otherwise lack.

#### *3.4.3.1 FISH probe selection*

Probes with different degrees of specificity that allowed us to target nitrifying bacteria in a hierarchical cascade, following a top to bottom approach, from group down to species, were selected (Figure 3.12). To this end, the EUBmix probes

(Amann et al., 1990; Daims et al., 1999) were conveniently combined with either one or two probes of higher specificity, taking into account the required stringency conditions as listed in Table 3.6. The fluorochrome used to tag each one of the probes to correctly visualise the different required combinations by means of CLSM can also be found in Table 3.6, together with the main characteristics of each probe.

Group level specific probes ALF1b, BET42 and GAM42 were selected to estimate the amount of active biomass (as targeted by EUBmix) that belonged to the $\alpha$,$\beta$ and γ-subclass of Proteobacteria. All ammonia oxidizing bacteria (AOB), with the exception of two marine species of the genus *Nitrosococcus*, belong to the $\beta$-subclass Proteobacteria; hence it is usually necessary to use several probes in order to discriminate and identify *Nitrosomonas*.

Probes specific to beta-subclass AOB (Nso190 and Nso1225) were used in combination with the species level specific probe Nse1472. However, no bacteria were detected with AOB probe Nso190 in any of the samples, while positive results were obtained with the Nse1472 and NEU probes.

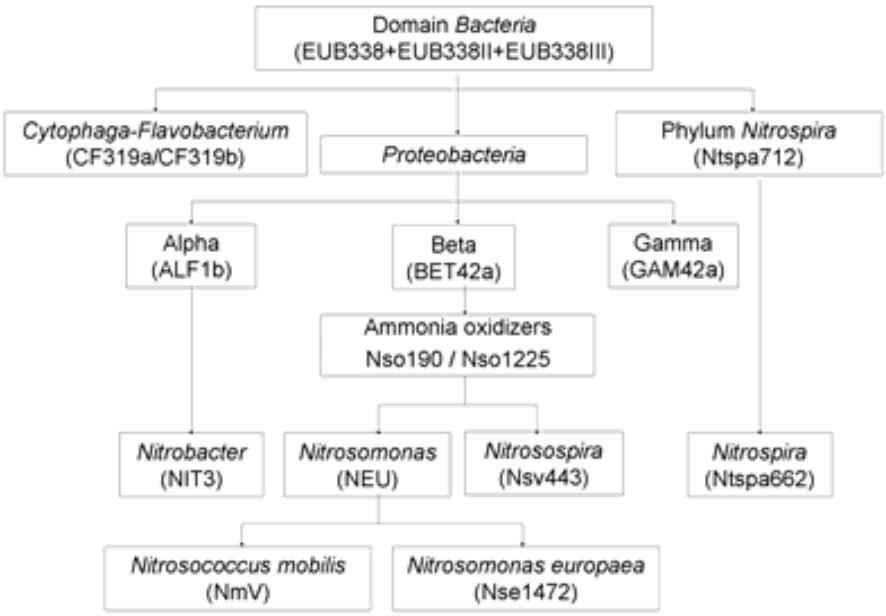


**Figure 3.12** Hierarchic classification of the rRNA-targeted oligonucleotide probes used for the FISH analysis. The used rRNA probes are listed together with their specific target species, ranging from the less specific (at the top of the diagram) to the most specific (bottom of the diagram).

The results obtained with the Nso190 probe were attributed to the sequence mismatch between the probe sequence and several strains of some AOB (e.g. *Nitrosomonas europaea*), which has already been reported by other authors (Persson et al., 2002; Utaker and Nes, 1998; Purkhold et al., 2000). On the other

hand, *Nitrobacter* belongs to the α-subclass of Proteobacteria while several other nitrite oxidizing bacteria (NOB) can not be included in this group. To specifically study the relative distribution of *N. europaea* and *N. winogradskyi*, the probes NEU and NIT3 (Wagner et al., 1995 and 1996, Table 3.6) were used, in combination with the EUBmix probes.

#### *3.4.3.2 Relative distribution of* N. europaea *and* N. winogradskyi *as depicted by FISH analysis*

After it was proved that no bacteria belonging to the β-proteobacterial AOB other than *N. europaea* and no NOB other than *N. winogradkyi* were detected, a number of samples arbitrarily chosen throughout the packed bed reactor were analysed by FISH-CLSM to evaluate the dominance of the initially inoculated nitrifiers (i.e. *N. europaea* and *N. winogradskyi*) in the biofilm. The relative amounts of the targeted bacterial species were calculated as the percentage of the total bacterial biomass.

Probes targeting *Nitrosomonas* species (NEU) (Wagner et al., 1995) or *Nitrobacter* species (NIT3) (Wagner et al., 1996) were combined in samples taken from fractions $F_0$, $F_2$, $F_4$ and $F_6$ (Figure 3.13). In samples taken from $F_0$ (4.7 cm) the average NEU positive biovolume was estimated as 82±9% of the total NEU+NIT3 positive biovolume, thus indicating that 82% of the total amount of nitrifying bacteria present in this fraction belong to the *Nitrosomonas* species and thus are AOB. In fraction $F_3$ (18.4 cm) the relative amount of *Nitrosomonas* was down to 44% and only 33.7% of the total biovolume occupied by nitrifiers in fraction $F_4$ (25 cm) corresponded to *Nitrosomonas*. In fraction $F_6$ (40.4 cm) *Nitrosomonas* represented 5% of the added volumes of *Nitrobacter* + *Nitrosomonas*.

Qualitative analysis of FISH images using the GAM42a (*γ-Proteobacteria*) and CF319a/b (*Cytophaga-Flavobacterium* group) probes, targeting heterotrophic organisms most commonly noted in nitrifying systems (Nogueira et al., 2002; Egli et al., 2003; Kindaichi et al., 2004), showed in general very little presence of bacteria belonging to these taxa.

**Table 3.6** Characteristics of the 16S rRNA-directed oligonucleotide probes used for FISH analysis. (*) probe position according to E. coli gene numbering. FITC: Fluorescein isothiocyanate, Cy3: sulfoindocyanine dye Cy3, Cy5: sulfoindocyanine dye Cy5.

| Name | Probe sequence | Label | Specificity | target site(*) | Reference | Formamide (%) | NaCl [mM] |
|---|---|---|---|---|---|---|---|
| EUB338 | **5'-gctgcctcccgtaggagt-3'** | **FITC** | All *Eubacteria* | 338-355 | Amann, et al. 1990 | 0-50% | 10-900 |
| EUB338II | **5'-gcagccacccgtaggtgt-3'** | **FITC** | *planctomycetales* | 338-355 | | 0-50% | 10-900 |
| EUB338III | **5'-gctgccacccgtaggtgt-3'** | **FITC** | *verrucomicrobiales* | 338-355 | Daims et al. 1999 Daims et al. 1999 | 0-50% | 10-900 |
| CF319a | **5'-tggtccgtgtctcagtac-3'** | **Cy5** | *Cytophaga-flavobacterium* group | 319-336 | Manz, et al., 1996 | 35% | 80 |
| CF319b | **5'-tggtccgtatctcagtac-3'** | **Cy5** | *Cytophaga-flavobacterium* group | 319-336 | Manz et al. 1996 | 35% | 80 |
| GAM42a | **5'-gccttcccacatcgttt-3'** | **Cy5** | γ-*proteobacteria* | 1027-1043 | Manz et al., 1992 | 35% | 80 |
| GAM42A Cmp | **5'-gccttcccacttcgttt-3'** | **Non** | β-*proteobacteria* | | | 35% | 80 |
| NIT3 | **5'-cctgtgctccatgctccg-3'** | **Cy3** | *Nitrobacter* | 1035-1052 | Wagner et al. 1996 | 40% | 50 |
| NIT3 Cmp | **5'-cctgtgctccaggctccg-3'** | **Non** | Competitor for NIT3 | | | 40% | 50 |
| NEU | **5'-cccctctgctgcactcta-3'** | **Cy5** | Most halophilic and halotolerant *Nitrosomonas species.* | 653-670 | Wagner et al. 1995 | 40% | 50 |
| NEU Cmp | **5'-ttccatccccctctgccg-3'** | **Non** | Competitor for NEU | | | 40% | 50 |
| Nse1472 | **5'-accccagtcatgaccccc-3'** | **Cy5** | *Nitosomonas europaea, Nitrosomonas halophila ,Nitrosomonas eutropha, isolate Nm103* | 1472-1489 | Burell et al. 1998 | 50% | 10 |

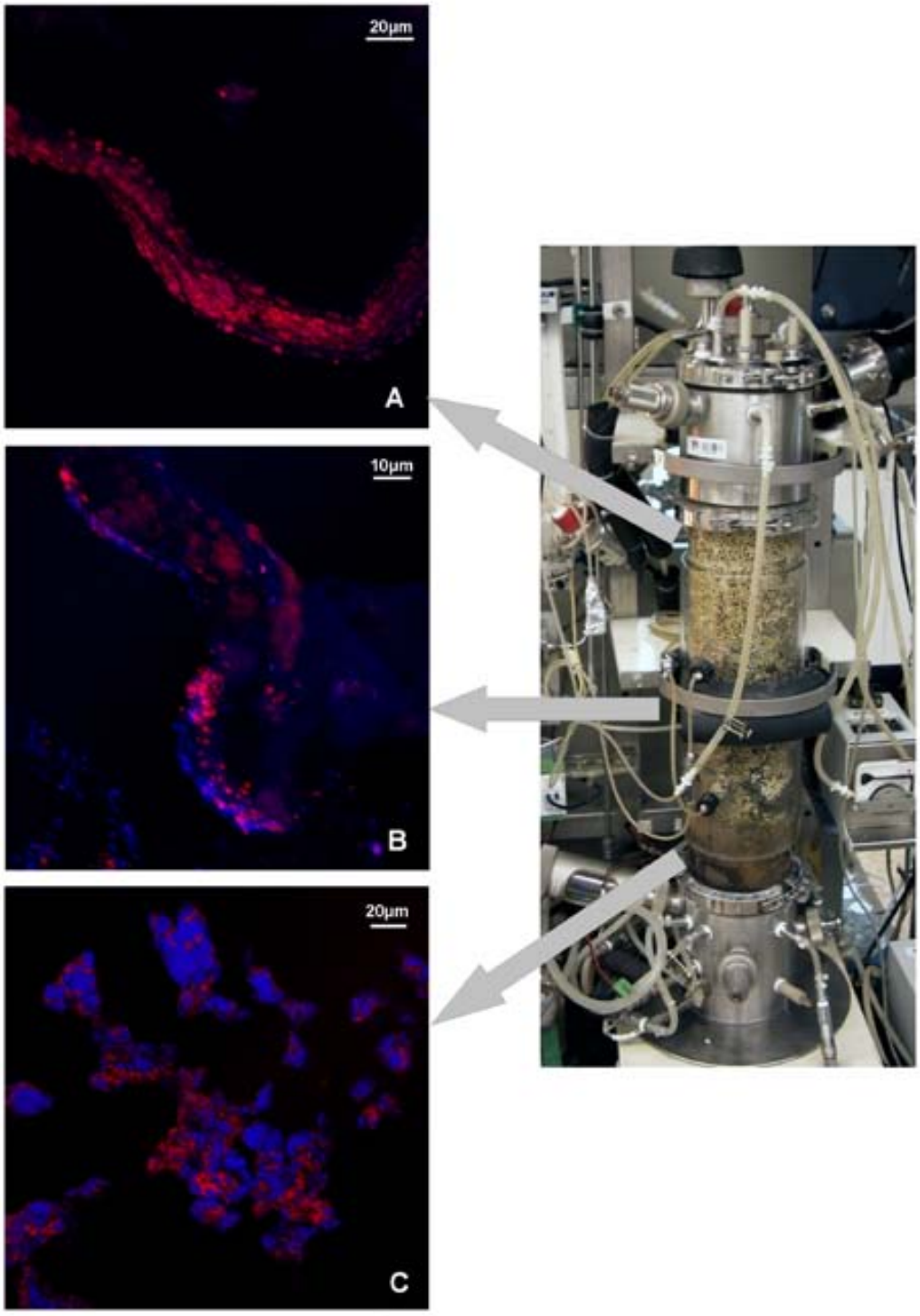


**Figure 3.13** FISH images showing the relative abundance of *N. europaea* (NEU, blue) and *N. winogradskyi* (NIT3, red) at different heights in the packed-bed. (A) fraction $F_6$. (B) fraction $F_4$. (C) fraction $F_0$.

The use of the GAM42a probe on samples from the fractions $F_0$, $F_1$ and $F_4$ revealed a presence of respectively 2.9%, 1.37% and 0.37% of cells belonging to the group of *γ-Proteobacteria* (Figure 3.14A). The CF319a/b was applied in samples $F_1$ as well as in $F_4$, resulting in the detection of 0.13% and 0.34%, respectively, of

the total scanned biomass, visualising bacterial cells belonging to the *Cytophaga-Flavobacterium* group (Figure 3.14B). However, the relative abundance of *Nitrosomonas* predicted by using the NEU and NIT3 probes was found to be of 82±9%, resulting in an approximate value of 18% of other contaminating organisms,; this is not in agreement with the low proportion of GAM42- and CF319-positive bacteria detected in the same fraction ($F_0$). Since it was proved through PCR and DGGE analysis that *Nitrosomas* and *Nitrobacter* were the only AOB and NOB present in the biofilm, this mismatch could only be attributed to a presence of other non-nitrifying bacteria that belonged to other taxa and hence could not be detected with the GAM42 and CF319 probes.

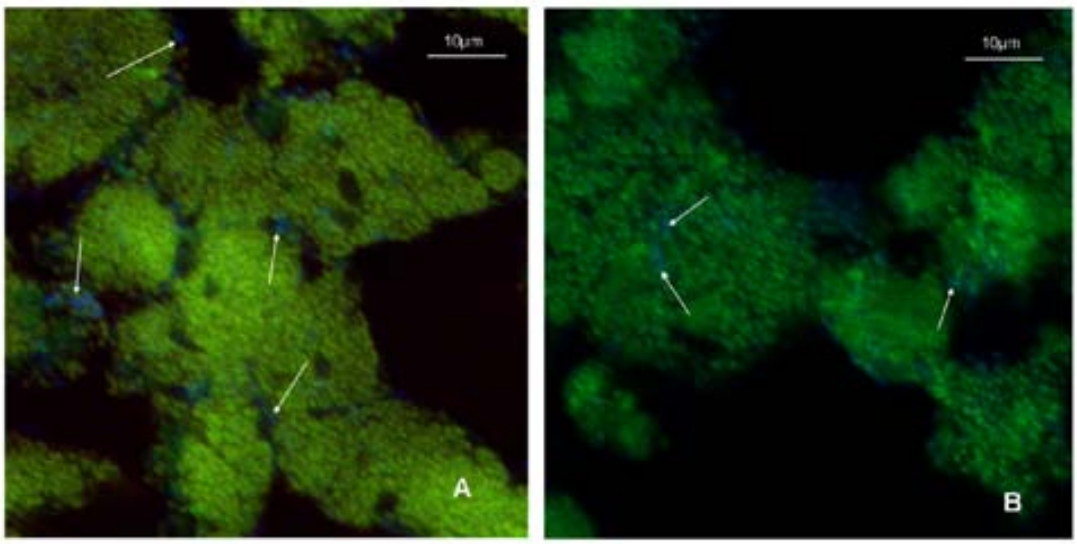


**Figure 3.14** (A) Image depicting the presence of bacteria belonging to the γ-Proteobacteria (GAM42a, blue) in the biofilm (EUBmix, green) in a sample taken from location $F_0$, (B) Image depicting bacteria belonging to the Cytophaga-flavobacterium group (CF319a/b, blue) in the biofilm (EUBmix, green) in a sample taken from location $F_4$.

In order to prove that, as indicated by DGGE analysis, *Nitrosomonas,* and more specifically, *N. europaea,* were the sole AOB in this autotrophic nitrifying biofilm, *,* the probe Nse1472, designed to target *N. europaea* and a very reduced group of other bacteria belonging to the *Nitrosomonas* species (Burell et al., 1998; Figure 3.6), was used on random samples taken at heights around 5 cm ($F_0$) (Figure 3.15A) and 25 cm ($F_4$) (Figure 3.15B). In fraction $F_0$ the biovolume of biofilm targeted by Nse1472 was estimated as 81% of the total EUBmix biomass, which is in good agreement with the results yielded by the *Nitrosomonas* species probe NEU (82±5%), thus confirming that *N. europaea* or a closely related species is indeed the most important AOB present in the biofilm. Similar results were obtained in fraction

$F_4$, halfway along the packed bed, in which hybridisation with the Nse1472 probe indicated that 34±23% of the total EUBmix biovolume was covered by *N. europaea*, while hybridisation results obtained with the NEU probe indicated that 38±15% of the total eubacterial biomass belonged to the *Nitrosomonas* species.

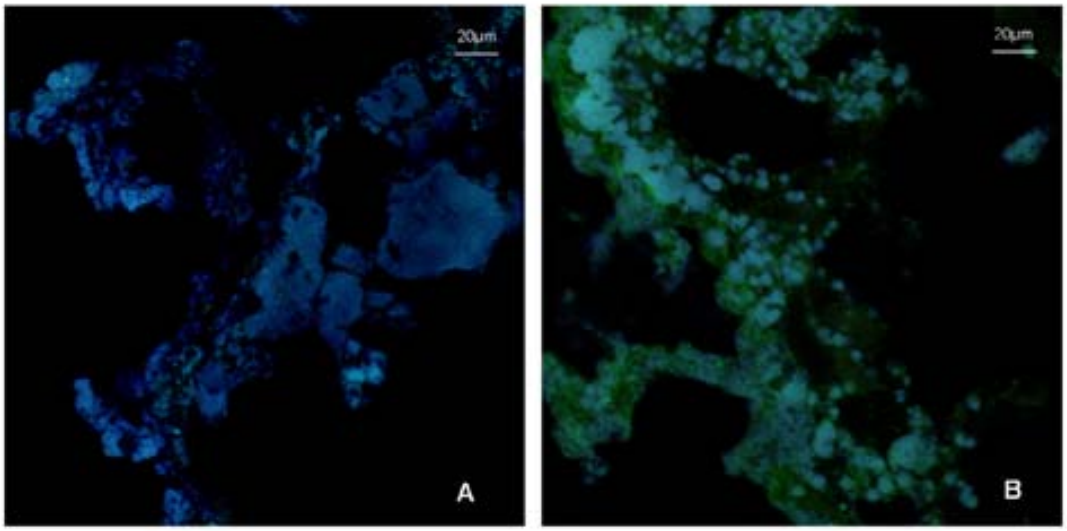


**Figure 3.15** (A) Image depicting Nitrosomonas (Nse 1472, blue) in the biofilm (EUBmix, green) in a sample taken from location $F_0$. (B) Image depicting *Nitrosomonas* (Nse1472, blue) in the biofilm (EUBmix, green) in a sample taken from location $F_4$.

### 3.4.4 Q-PCR ANALYSIS OF THE NITRIFYING BIOFILM

In this study, Q-PCR primers were developed to target the nitrifying organisms at species level for the enumeration of the AOB and NOB in each fraction of the packed-bed. Q-PCR on total genomic DNA extracted from the biofilm samples allowed the amplification of genome-bound 16S rRNA genes via transcription-independent screening of the biofilm for 16S rRNA gene-copy abundance. Validation of the primers and the chosen approach for the Q-PCR was performed with several test runs on different dilutions of *N. europaea* and *N. winogradskyi* cultures. Results obtained from the analysis of samples at different heights of the reactor by Q-PCR are shown in Figure 3.16.

In contrast to the relative abundances determined using the FISH-CLSM analyses (i.e. ratio with respect to total bacterial biovolume), the Neu/Nwi-ratios were calculated by determining the ratio of the cellular abundances of both bacteria to the sum of the total cellular abundance of both nitrifiers (e.g. # Nts / (# Nts + # Ntb) for the relative abundance of *N. europaea* in one position).

The Q-PCR results of the reactor samples appear to have a high similarity at position $F_0$ (89.7% ±7.8 *N. europaea*) and $F_1$ (91.3% ±7.1 *N. europaea*). The relative amounts of *N. europaea* in samples $F_2$ (57.3% ±8.3 *N. europaea*) and $F_3$ (58.7% ±5.3 *N. europaea*) also appear to be quite similar. A gradual increase of *N. winogradskyi* can be observed with increasing height as depicted by the relative amounts obtained from positions $F_4$ (61.0% ±2.6 *N. winogradskyi*), $F_5$ (70.1% ±1.3 *N. winogradskyi*), and $F_6$ (70.0% ±1.0 *N. winogradskyi*). However, in the last fraction of the packed-bed ($F_7$) an increase in the *N. europaea* relative abundance was observed, reducing the relative amount of *N. winogradskyi* back to 53.9% ±1.9.

These results are in agreement with observations performed at macroscopic scale in similar nitrifying bioreactors, e.g. nitrifying trickling filters or nitrifying bioreactors possessing a degree of plug-flow (Holben et al., 1998; Lydmark et al., 2006; Fdz-Polanco et al., 2000; Wijeyekoon et al., 2000), in which a spatial distribution profile of the AOB and NOB was detected.

### 3.4.5 CORRELATION BETWEEN THE RESULTS OBTAINED BY FISH AND Q-PCR

As discussed in section 3.4.3 the limited number of FISH images available for quantification led to a lack of statistical consistency of the FISH results making it necessary to rely almost uniquely on Q-PCR analysis to obtain quantitative information on the relative abundance of *N. europaea* and *N. winogradskyi* along the packed bed. However, the results of the FISH analysis were useful to qualitatively assess the dominance of the two initial strains (i.e. *N. europaea* and *N. winogradskyi*) in the biofilm based on the observations of CLSM images corresponding to several randomly selected samples taken from different positions of the packed bed.

The number of CLSM images available for quantification was low in most fractions of the packed bed and for most probe combinations. However, at some positions along the packed bed a higher number of CLSM images were available and thus quantification results were granted enough statistical consistency. Therefore, the quantification algorithm was applied to these samples in order to estimate the biovolumes of the NEU and NIT3 probes (targeting *Nitrosomonas* and *Nitrobacter* respectively) and the results are presented in Figure 3.16 together with the Q-PCR results.

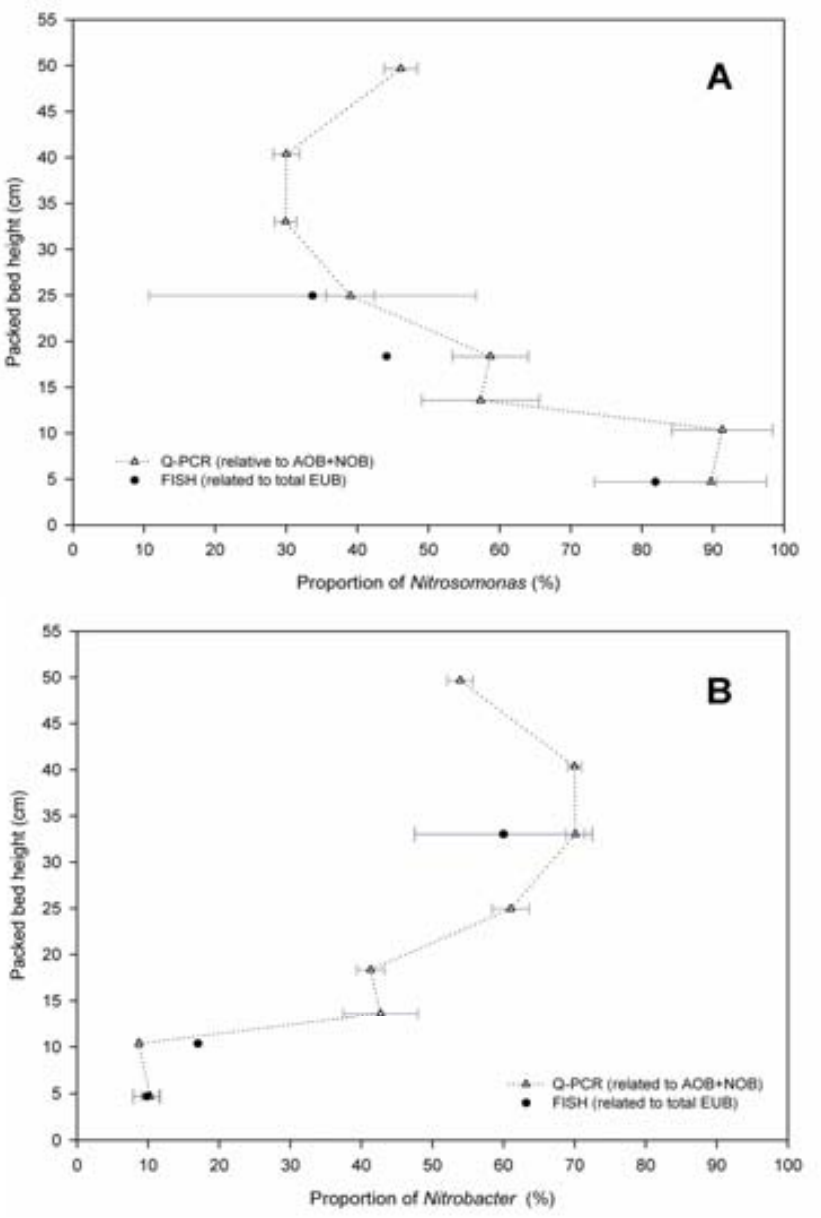


**Figure 3.16** Q-PCR and FISH estimation of the *Nitrosomonas* (A) and *Nitrobacter* (B) relative abundance along the packed bed.

It must be taken into account when comparing the results obtained with both methods that, while FISH percentages were obtained as a proportion of the total bacterial biomass targeted by EUBmix, Q-PCR percentages were calculated as related to total *Nitrosomonas* + *Nitrobacter* (e.g. Nitrosomonas/ (Nitrosomonas+Nitrobacter). The fact that DGGE and qualitative evaluation of FISH-CLSM images revealed only a low presence of possible contaminants, made the results obtained with both methods and presented in Figure 3.16 quite comparable. However, this could lead to a certain underestimation of the FISH results when compared to the Q-PCR.

In fraction F5, with samples obtained at an average height of 31cm, the proportion of *Nitrosomonas* obtained by Q-PCR was 29.9%, i.e. 70.1% for *Nitrobacter*, while the amount of *Nitrobacter* as estimated by FISH was 60%. Again, there is a certain difference between the estimations obtained by the two techniques that could be explained by the intrinsic error of each method, but a similar overall trend along the packed bed is depicted by both methods.

Finally, in fraction F7, which included a part of the packed bed that ranged between 43 cm and 56 cm, the trend of *Nitrosomonas* proportion to decrease was reversed. A proportion of 46.1% of *Nitrosomonas* and 53.9% of *Nitrobacter* was obtained as a result of Q-PCR analysis. Unfortunately, reliable FISH information was not available for this fraction to back up this information. In Chapter 5 of this thesis a mathematical model will be used to support the hypothesis that these results are influenced by the reactor hydrodynamics and, indeed, should be expected in this packed bed reactor.

## 3.5 CONCLUSIONS

Through analysis by means of two molecular-based techniques, relevant information was obtained regarding the biomass distribution within the autotrophic nitrifying biofilm from the CIII of the MELiSSA after 4.8 years of continuous operation. The main conclusions of this study are listed below:

- A trend of the total biomass concentration to decrease with increasing height was experimentally assessed through dry weight analysis, thus confirming the observations of previous periods of operation in this reactor.
- DGGE analysis, together with FISH analysis coupled with CLSM observation, demonstrated that after 4.8 years of continuous operation *N. europaea* and *N. winogradskyi* remained the dominant strains in the CIII biofilm, thus confirming the long term stability of the nitrifying compartment of MELiSSA.
- A general trend of the *N. europaea* proportion to decrease with height was assessed through qualitative evaluation of FISH samples visualised using CLSM. Quantitative experimental evidence of this segregation of the two bacterial strains performing the two step nitrification process was achieved through Q-PCR analysis.

# PART III

# MATHEMATICAL MODELLING

## CHAPTER 4

**Development of a dynamic one-dimensional multi-species biofilm model**

## CHAPTER 5

**Evaluation of the reactor nitrifying efficiency and the relative abundance of nitrifying bacteria in the biofilm through mathematical modelling**

## CHAPTER 6

**Model-based assessment of the backwashing frequency and intensity requirements in the packed bed reactor**

# CHAPTER 4

# DEVELOPMENT OF A DYNAMIC ONE-DIMENSIONAL MULTI-SPECIES BIOFILM MODEL

## *Foreword*

*The development of a mathematical model for the nitrifying packed bed reactor is expected to provide further knowledge of the development of the biofilm structure and the overall reactor performance, in combination with the experimental information collected throughout operation and upon dismantling of the reactor. The model presented in this chapter allows simulation of reactor behaviour with high accuracy under a wide range of conditions and prediction of the effect of different parameters and potential perturbations on the main state variables. In the formulation of this new model, processes such as detachment and soluble substrate / product diffusion within the biofilm are taken into account, thus providing the accurate description sought in this study, yet without high computational requirements. A thorough description of the formulation of this new model and the guidelines for its implementation will be provided in this chapter.*

## 4.1 INTRODUCTION

As part of a complex loop of interconnected bioreactors, the necessity to ensure the stability of the performance of every compartment in the MELiSSA loop under a wide range of conditions is essential. The availability of a mathematical model not only offers a useful tool to predict and analyse the behaviour of the bioreactor under different scenarios, but it can also be integrated in the local control strategy.

Mathematical modelling is a tool widely used to simulate different hypothetical scenarios and to optimise operation or control strategies. Theoretical studies based on the use of mathematical models applied to reactors similar to the one used in this study are well reported in the literature. Bernet et al. (2005) used a mathematical model to predict the effect of some operating parameters on nitrite accumulation and designed a control strategy based on the obtained results. Another example of simulation applied to the design of a control strategy is reported by Benthack et al. (2001), who used a mathematical model to optimise the treatment efficiency in an aerobic biofilter and implemented the solution on a control system.

The response of the nitrifying compartment, both in transient and steady states, was experimentally evaluated in previous studies by maintaining the continuous operation of the pilot reactor as well as three bench scale reactors for several months, during which several operational conditions were tested (Pérez et al., 2004). The results of these tests were used to validate a simple model that was capable of describing, with acceptable accuracy, the main features of the operation of the pilot nitrifying packed bed bioreactor (An accurate description of the reactor was provided in Chapter 1, section 1.5). Such a simplified mathematical model was implemented in Matlab v.4.2b (The MathWorks Inc., 1994) with the purpose of describing the operation of the reactor under typical operational conditions. The resulting model was required to be a dynamic model that could describe with acceptable accurary the general features of the reactor operation. The dynamic response during the transient states originated after a perturbation or the distribution of the biomass along the packed bed, which had been experimentally observed, should be correctly predicted by the model.

The established limits of the model were a compromise between computing time and required accuracy; using the model for control applications called for limited computational times, thus the formulation of a more complex model involving diffusion limitations of substrates was out of the scope of the defined goals at the

moment of its development. Based on the objectives presented above, the following main assumptions were made in the definition of the model: (i) a new flow model was developed that could harmonise the close to perfectly mixed tank behaviour revealed by DTR experiments with the profile of biomass concentration observed along the packed bed height; (ii) Diffusion limitation was not considered for the active cells in the biofilm; (ii) biomass growth takes place exclusively in the biofilm and hence no nitrifying activity from suspended biomass or biomass adhered below the packed bed was taken into account, (iii) detachment and cell decay were described by means of a single parameter that involved the two processes.

The resulting mathematical model strongly relied on the optimisation of two empirical parameters - the initial concentrations of both bacterial species and the parameter defined to describe detachment and decay. By adjusting these parameters, the overall behaviour of the reactor could be predicted with satisfactory accuracy but without unacceptable computational requirements (Pérez et al., 2005). However, this strategy complicates the identification and quantification of the individual parameters affecting the biofilm formation and their individual effect on certain features of the process behaviour.

With the aim of overcoming the limitations presented by the aforementioned mathematical model, such as the difficulty to study the different parameters affecting the biofilm structure and the substrate conversion separately, a new approach to the modelling of the reactor is proposed. The development of a dynamic one-dimensional multi-species mathematical biofilm model was envisaged with the goal to increase the knowledge about the operation of the nitrifying pilot bioreactor of the MELiSSA project.

## 4.2 MODEL DEVELOPMENT AND IMPLEMENTATION

The possibility to develop a biofilm model that would take into account the diffusion of soluble components through the biofilm and that would allow specific implementation of processes such as detachment was regarded as a remarkable improvement on the previous model of the system.

The model formulated hereafter was implemented in AQUASIM v. 2.1 (Wanner and Reichert, 1996; Reichert, 1998), which offers the possibility to define all the biofilm processes and to evaluate their effects individually. Studies performed with AQUASIM available in recent publications (Saejima et al., 2008; Ni and Yu,

2008; Terada, A. et al. 2007; Matsumoto et al., 2007; Wahman, D.G. et al. 2006), confirm its suitability for biofilm modelling.

In the present section the main considerations for the model formulation are established and its main structure is subsequently described. The main features of the mathematical model will be presented individually, followed by a description of the model structure and development. Hence, the mass transfer processes between the different phases of the reactor, the flow model describing the hydrodynamics of the reactor liquid phase and the stoichiometry and kinetics of the nitrification process will all be comprehensively described in the following sections of this chapter.

### 4.2.1 ASSUMPTIONS FOR THE FORMULATION OF THE MODEL

The complexity of a mathematical model needs to reach a compromise between computational time and required accuracy. The following assumptions and main considerations were made for the formulation of the model developed in this thesis:

- The transport of all substrates and products as well as the biofilm growth was assumed to take place along one single direction, giving as a result a one-dimensional biofilm model. Since the biofilm developed on a spherical support, all transport processes were considered to take place along the direction perpendicular to the surface of the support particles using spherical coordinates.
- Three different bacterial species were described in this model: *N. europaea*, *N. winogradskyi* and a mixed population of heterotrophic bacteria, according to the experimental results obtained in Chapter 3, which revealed a small population of heterotrophic bacteria in the reactor.
- The flow of solids within the biofilm matrix was assumed to take place only by advection. Therefore, diffusion of solid material within the biofilm matrix was not taken into account. The velocity of the interface between the biofilm and the the bulk volume ($u_L$) was assumed to have contributions only by the the advective velocity at the biofilm surface ($u_F$) and the detachment velocity ($u_{det}$).
- The porosity of the biofilm was assumed to be constant.

## 4.2.2 MASS TRANSFER PROCESSES IN THE BIOFILM

As previously mentioned, the use of AQUASIM v2.1 (Wanner and Reichert, 1996; Reichert, 1998) provided the required tools to develop a mathematical model that would allow the implementation of all the involved mass transfer processes, thus granting a compromise between complexity and improved accuracy.

### *4.2.2.1 Diffusive transport of soluble components between the liquid phase and the biofilm matrix*

All soluble substrates and products involved in the biochemical reactions that take place in the biofilm, have to diffuse from the liquid phase into the biofilm and vice versa.

The flux of a soluble component ($J_{L,i}$) can be described using Fick's law (Equation 4.1), where $D_i$ is the molecular diffusion coefficient (in $dm^2 \cdot d^{-1}$) for a soluble component (i) in the culture medium, $C_i$ is the concentration ($g \cdot L^{-1}$) of a soluble component (i) and $r$ indicates the radial direction of the flux. In this case, since the biofilm grows on a spherical support (BIOSTYR®), this substratum cannot be considered as a flat surface and the dependence of the biofilm volume on the radius has to be taken into account by using spherical coordinates.

$$J_i = -D_i \frac{\partial C_i}{\partial r} \qquad \textbf{4.1}$$

### *4.2.2.2 Advective transport of solid components: biofilm growth and detachment*

Biofilm growth is regulated by detachment mechanisms, which have a great influence on the biofilm morphology of the resulting biofilm. The detachment rate can change with time along the operation of the reactor and might be much higher at initial stages of operation and especially during reactor start-up.

A flux of solid material from the biofilm to the liquid phase due to detachment, as well as the advance of the solid-liquid interface due to growth, with resulting gradual increase of the biofilm thickness with time, have to be taken into account and implemented in the model. $J_{F,i}$ ($g \cdot dm^{-2} \cdot d^{-1}$) symbolises the flux of a solid component (denoted as i) from the substratum surface towards the biofilm-bulk liquid interface. Since it has been assumed that transport of particulate substances only takes place in the biofilm matrix by advection mechanisms, not by diffusion, this flow can be described by Equation 4.2, where $X^i$ is the concentration of a

particulate species (i) and $u_F$ ($dm \cdot d^{-1}$) accounts for the advective velocity of the biofilm surface due to growth, i.e. the summatory of the subsequent volume expansions of the biofilm from the surface of the support beads towards the surface of the biofilm in contact with the bulk liquid.

$$J_{F,i} = u_F \cdot X^i \quad \textbf{4.2}$$

The net velocity i.e. the actual increase of the biofilm thickness with time ($u_L$, Equation 4.3) is the result of subtracting the detachment rate ($u_{det}$) from the total advective velocity of the biofilm surface ($u_F$, Equation 4.4). All biofilm related velocities are expressed in $dm \cdot d^{-1}$.

$$\frac{dLF}{dt} = u_L \quad \textbf{4.3}$$

$$u_L = u_F - u_{det} \quad \textbf{4.4}$$

In the literature, detachment velocity has been described as being dependent on different parameters. The growth of a biofilm depends on the balance between attachment and detachment forces. The detachment rate ($u_{det}$) is usually correlated to the growth velocity of the biofilm ($u_F$) and the biofilm thickness (Morgenroth and Wilderer, 2000; Wanner and Morgenroth, 2004). The maximum biofilm thickness ($LF_{max}$) was estimated from the experimental dry weight measured at different heights (Figure 3.6, Chapter 3).

### 4.2.3 GAS-LIQUID MASS TRANSFER

Gas components involved in the reactions, mainly oxygen in the studied system, need to cross the gas-liquid interface before they can diffuse to and from the biofilm. In the specific case of oxygen the flux of this compound from the gas phase into the bulk liquid was defined as a dynamic process according to Equation 4.5, where $K_L \cdot a$ is the global volumetric gas-liquid mass transfer coefficient expressed in $d^{-1}$, $C_{O_2}$ is the dissolved oxygen concentration in the liquid phase, required in mg $O_2 \cdot L^{-1}$,and $C^*_{O_2}$ is the oxygen saturation concentration, also expressed in mg $O_2 \cdot L^{-1}$. The flux ($J_{L,O_2}$) thus calculated is obtained in terms of mg $O_2 \cdot L^{-1} \cdot d^{-1}$.

$$J_{G,O_2} = K_L \cdot a \cdot \left(C^*_{O_2} - C_{O_2}\right) \quad \textbf{4.5}$$

#### *4.2.3.1 Estimation of the oxygen volumetric gas-liquid mass transfer coefficient*

The volumetric gas-liquid mass transfer coefficient ($K_L \cdot a$) was determined differently in the three main different parts of the reactor (A, B and C). The reactor is provided with two oxygen sensors located in the bottom (A) and in the top (C) sections of the reactor, providing dissolved oxygen measurements in these two locations and hence allowing the use of a dynamic technique for the estimation of the $K_L \cdot a$.

The gassing-out method was thus used to experimentally estimate the value of the $K_L \cdot a$ in the bottom and the top sections of the reactor, both of which behave as a perfectly mixed tank. The $K_L \cdot a$ estimation procedure was performed in this case before reactor inoculation (Pérez et al., 2006). Under the operational conditions of the reactor ($Q_{rec}=6 \cdot Q_{in}$, $Q_G=3$ L·min$^{-1}$, magnetic stirring in the bottom section at 400 rpm) the measured values of $K_L \cdot a$ were 1555 d$^{-1}$ at the bottom section (A) and 1210 d$^{-1}$ at the top section (C) of the reactor.

The $K_L \cdot a$ in the packed bed was estimated by means of an empirical correlation (Poughon et al., 2003; Pérez et al., 2005), which is dependent on the reactor design and the gas superficial velocity ($u_G$). Using this correlation and taking into account the different values of the gas superficial velocity ($u_G$) in each one of the seven fractions of the packed bed ($B_1$-$B_7$) the $K_L \cdot a$ can be estimated using Equation 4.6, where $u_G$ is required in m·s$^{-1}$, $d_P$ is the substratum particle diameter (in dm) and D is the reactor diameter (in dm).

$$K_L \cdot a = 35544 \cdot (u_G)^{0.5979} \left( \frac{d_P}{D} \right)^{-0.1153} \qquad \textbf{4.6}$$

The gas superficial velocity not only varies with height, but also as a function of the operation time due to its dependence on the bed porosity and consequently on the biofilm thickness (LF). The value of $u_G$ can be calculated by means of Equation 4.7, where $Q_G$ is the gas flow rate, in m$^3$·d$^{-1}$, $(1-\varepsilon_P)$ is the bed porosity and $A$ is the section in m$^2$. The value of $u_G$ thus calculated is expressed in m·d$^{-1}$.

$$u_G = \frac{Q_G}{A \cdot (1-\varepsilon_P)} \qquad \textbf{4.7}$$

#### *4.2.3.2 Oxygen saturation concentration along the packed bed*

The oxygen saturation concentration along the reactor was estimated by combining the overall oxygen mass balance in the bioreactor, the expression of the oxygen saturation concentration given by Henry's law and the oxygen mass balance in the liquid phase. The oxygen saturation concentration ($C^*_{O_2}$) along the packed bed presents a gradient, decreasing with height as a result of diminishing oxygen purity in the air flow. A different oxygen saturation concentration was estimated for each one of the seven fractions of the packed bed (section B) as well as for the bottom and top parts of the reactor (sections A and C respectively).

The overall oxygen mass balance in the liquid phase of the reactor at steady state is described by Equation 4.8 where $n_G$ is the gas molar flow in mol·min$^{-1}$; $y_{O_2}$ is the oxygen molar fraction expressed in mol $O_2$·mol$^{-1}$; $V_{L,A}$, $V_{L,B}$ and $V_{L,C}$ are the volumes of the three main sections of the reactor (A, B and C) in L. The flow model, which will be explained in detail in section 4.2.4.2, is integrated in the balance, leading to different oxygen consumption rates ($r_{O_2,A}$, $r_{O_2,B}$ and $r_{O_2,C}$) in the different sections of the reactor and in each one of the seven fractions (j=1,…,N with N=7) integrating the packed bed (B), which were also considered separately. The oxygen consumption rate is required in mol $O_2$·L$^{-1}$·d$^{-1}$.

$$n_{G,in}\cdot y_{O_2,in} - n_{G,out}\cdot y_{O_2,out} = r_{O_2,A}\cdot V_{L,A} + \sum_{j=1}^{N} r_{O_2,B_j}\cdot V_{L,B_j} + r_{O_2,C}\cdot V_{L,C} \qquad \textbf{4.8}$$

The oxygen saturation concentration can be calculated through Equations 4.9-4.11. The saturation concentration is obtained in mol $O_2$·L$^{-1}$, the oxygen molar fraction ($y_{O_2}$) is expressed in mol $O_2$·mol$^{-1}$, $P$ is the total pressure in the reactor (the subscripts indicate the location in the reactor), H stands for Henry's constant and is required in Pa, $\rho$ is the liquid density (assumed to be equal to that of water and required in g·L$^{-1}$) and MW is the molecular weight of water (18) in g·mol$^{-1}$.

$$C^*_{O_2,A} = \frac{y_{O_2,in}\cdot P_{in} - y_{O_2,A}\cdot P_A}{H\cdot \ln\left(\frac{y_{O_2,in}\cdot P_{in}}{y_{O_2,A}\cdot P_A}\right)}\cdot\left(\frac{\rho}{MW}\right)_{H_2O} \quad \text{(section A of the reactor, bottom)} \qquad \textbf{4.9}$$

$$C^*_{O_2,Bj} = \frac{y_{O_2,A}\cdot P_A - y_{O_2,Bj}\cdot P_{Bj}}{H\cdot \ln\left(\frac{y_{O_2,A}\cdot P_A}{y_{O_2,B_j}\cdot P_{B_j}}\right)}\cdot\left(\frac{\rho}{MW}\right)_{H_2O} \quad \text{(section B; j=1,…,N with N=7)} \qquad \textbf{4.10}$$

$$C^*_{O_2,C} = \frac{y_{O_2,B_n}\cdot P_{B_n} - y_{O_2,C}\cdot P_C}{H\cdot \ln\left(\frac{y_{O_2,B_n}\cdot P_{B_n}}{y_{O_2,C}\cdot P_C}\right)}\cdot\left(\frac{\rho}{MW}\right)_{H_2O} \quad \text{(section C of the reactor, top)} \qquad \textbf{4.11}$$

The oxygen balance in the liquid phase at steady state and when the dissolved oxygen concentration is negligible (such as is the case when either the sulphite or the gassing out method is applied) is given by Equations 4.12-4.14, where the value of the $K_L\cdot a$ is obtained in $d^{-1}$ when the oxygen consumption rate ($r_{O_2}$) is expressed in $molO_2\cdot L^{-1}\cdot d^{-1}$ and the oxygen saturation concentration ($C^*_A$) in $molO_2\cdot L^{-1}$.

$$(K_L\cdot a)_A = \frac{r_{O_2,A}}{C^*_{O_2,A}} \quad \text{(section A)} \qquad \textbf{4.12}$$

$$(K_L\cdot a)_{B_j} = \frac{r_{O_2,B_j}}{C^*_{O_2,B_j}} \quad \text{(section B; j=1,…,N; with N=7)} \qquad \textbf{4.13}$$

$$(K_L\cdot a)_C = \frac{r_{O_2,C}}{C^*_{O_2,C}} \quad \text{(section C)} \qquad \textbf{4.14}$$

The oxygen molar fraction in the gas flow ($y_{O_2}$) can be calculated through Equations 4.15 -4.22 for the different reactor sections.

$$y_{O_2,A} = \frac{A}{1+A} \quad \text{where:} \qquad \textbf{4.15}$$

$$A = \frac{y_{O_w,in} - r_{O_2,A}\cdot\frac{V_{L,A}}{n_{G,in}}}{1-y_{O_2,in}} \qquad \textbf{4.16}$$

$$y_{O_2,B_j} = \frac{A}{1+A} \text{ where:} \quad \textbf{4.17}$$

$$A = \frac{y_{O_w,A} - r_{O_2,B_j} \cdot \frac{V_{L,B_j}}{n_{G,A}}}{1 - y_{O_2,A}} \text{ with j=1,…,N; with N=7} \quad \textbf{4.18}$$

$$n_{G,A} = n_{G,in} - r_{O_2,A} \cdot V_{L,A} \quad \textbf{4.19}$$

$$y_{O_2,out} = \frac{A}{1+A} \text{ where:} \quad \textbf{4.20}$$

$$A = \frac{y_{O_w,B_N} - r_{O_2,C} \cdot \frac{V_{L,C}}{n_{G,B_N}}}{1 - y_{O_2,B_N}} \quad \textbf{4.21}$$

$$n_{G,B} = n_{G,A} - r_{O_2,B_N} \cdot V_{L,B_N} \quad \textbf{4.22}$$

The effect of the ionic strength of the culture medium on Henry's constant ($H$) was estimated following the protocol described by Schumpe et al. (1982), which takes into account the concentration of all the electrolytes present in the culture broth to estimate their effect on the oxygen solubility according to Equations 4.23 and 4.24. In Equation 4.23 the value of Henry's constant for the culture medium ($H$) and Henry's constant of water ($H_{H_2O}$) are required in Pa. Schumpe's model parameters ($h_i$) are tabulated for each ion as a function of temperature (Schumpe et al., 1982).

$$\log\left(\frac{H}{H_{H_2O}}\right) = \sum h_i \cdot I_i \quad \textbf{4.23}$$

The ionic strength ($I_i$) can be calculated by means of Equation 4.24 as a function of the concentration of each ion present in the solution ($C_i$, required in mol·L$^{-1}$) and the absolute value of its charge ($z_i$).

$$I_i = \frac{1}{2} C_i \cdot z_i^2 \text{ where:} \quad \textbf{4.24}$$

The effect of decreasing total pressure with height on the estimation of oxygen saturation concentration described by Sekizawa et al. (1985) was calculated using Equation 4.25, where $\rho$ is the density of the solution in g·L$^{-1}$, $g$ is the acceleration due to gravity in m·s$^{-2}$, $P_{atm}$ is the atmospheric pressure in Pa, $\varepsilon_G$ is the gas hold up, $(1-\varepsilon_p)$ is the bed porosity, $h$ is the distance from the oxygen supply point in dm.

$$C^{*}_{O_2,corrected} = C^{*}\left[1+\frac{\rho \cdot g}{P_{atm}}\cdot\frac{1-\varepsilon_G}{1-\varepsilon_p}\right]\cdot h \qquad \textbf{4.25}$$

Equations 4.8 to 4.14 were solved by assuming the $K_L$·a estimated for each fraction through an empirical correlation (Equation 4.6) was constant with time, i.e. the $K_L$·a values previously calculated with Equations 4.6 and 4.7 were used as input to estimate the oxygen saturation concentration through the algorithm presented in Figure 4.1.

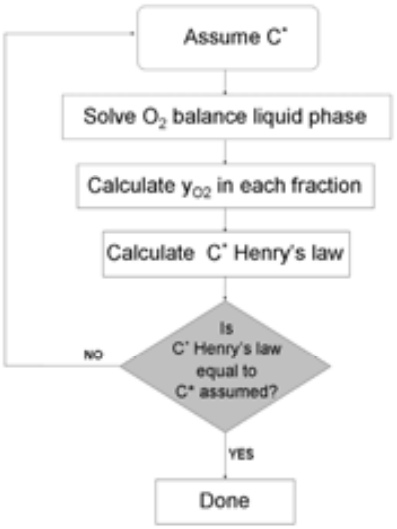


**Figure 4.1** Procedure followed for the estimation of the oxygen saturation concentration in each reactor fraction.

### 4.2.4 LIQUID PHASE FLOW MODEL

The liquid phase hydrodynamics in the reactor was studied through Residence Time Distribution (RTD) experiments (Pérez et al., 2004). It was determined that the reactor behaved similarly to a Continuous Stirred Tank Reactor (CSTR), but with a slight contribution from plug flow (Pérez et al., 2004). A flow model of the liquid phase that would describe with high accuracy the hydrodynamic behaviour of the reactor as evidenced by RTD experiments was subsequently developed and validated by Pérez et al. (2005). A detailed description of the resulting flow mode and the RTD experiments that led to the development and calibration of the model will be presented in this section.

#### *4.2.4.1 Assessment of the flow pattern through RTD experiments*

As previously stated, the liquid flow pattern in the bioreactor was assessed through RTD experiments performed prior to reactor inoculation (Pérez et al., 2004). The experimental RTD profiles obtained under three sets of operational conditions,

including different values of recirculation ratio and aeration flow rate (Table 4.1), are presented in Figure 4.4 alongside the model results.

**Table 4.1** Residence time distribution experiments operational conditions.

| Experiment number | Gas flow rate ($L \cdot min^{-1}$) | Liquid rate ($L \cdot min^{-1}$) | Recirculation flow rate ($L \cdot min^{-1}$) | Recirculation ratio (inlet/rec) | Back-mixing flow rate ($mL \cdot min^{-1}$) |
|---|---|---|---|---|---|
| 1 | 3 | 0.0028 | 0.045 | 1/15 | 175.0 |
| 2 | 3 | 0.0028 | 0.018 | 1/6 | 229.4 |
| 3 | 3 | 0.0028 | 0 | 1/0 | 277.9 |

From these results it was concluded that as long as the gas flow rate was maintained around its usual operational value of 3 $L \cdot min^{-1}$, the flow pattern of the liquid phase of the reactor could be considered as being very similar to that of an ideal stirred tank. Although the use of different values of the recirculation ratio was found to have an effect on the RTD profile, the main contribution to the liquid flow pattern was due to the gas flow rate, thus only a small contribution from plug-flow had to be considered.

#### *4.2.4.2 Flow model description*

Although only a small deviation from perfectly mixed tank behaviour was observed through RTD analysis, this small contribution was accountable for the gradient in biofilm thickness along the packed bed. A high mixing time for the liquid phase, in combination with a high nitrification rate are the main causes for this gradient in biomass concentration that could be experimentally observed along the packed bed vertical axis (Figure 4.2).

A common way to model the hydrodynamic behaviour of certain reactors is by using a tanks-in-series model, i.e. by combining a number of CSTRs in series. The use of a tanks-in-series model was found to be appropriate to model the liquid phase of this reactor, as it allowed describing the plug flow component detected through RTD analysis.

An accurate description of the reactor hydrodynamics was achieved by dividing it into three different parts (henceforth referred to as A, B and C). The bottom section (A) and the top section (C) were both approximated by a single stirred tank reactor, while the packed bed (B) was divided into N perfectly mixed tanks in series, each one having the same liquid volume. The liquid phase was thus described by means of a tanks-in-series model with the addition of a back mixing term to describe the mixing effect induced by the aeration flow rate (Figure 4.2).

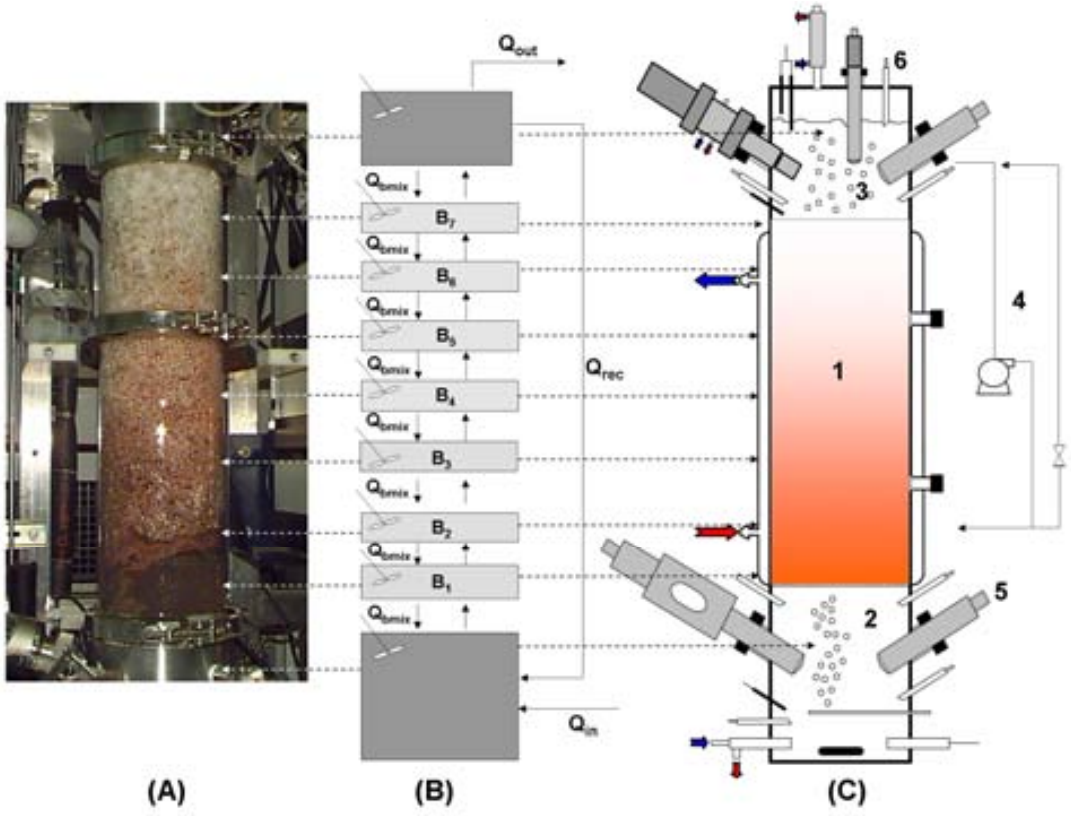


**Figure 4.2** (A) Picture of the reactor at t=1750d. (B) Flow model of the packed bed reactor. C) Scheme of the hardware of the packed bed reactor. (1) Packed bed section, (2) bottom section for air and liquid supply, (3) top section for liquid-gas separation, (4) liquid recirculation and back-washing loop, (5) reactor liquid feeding, (6) reactor liquid exhaust. $Q_{in}$ represents the liquid incoming flow rate, $Q_{out}$ stands for the effluent of the reactor, $Q_{rec}$ is the recirculation flow rate between the top of the reactor and the bottom mixed compartment, $Q_{bmix}$ is the back-mixing flow rate used in the description of the flow model to symbolise the mixing effect induced by aeration.

The number of tanks of equal liquid volume (N) into which the central section B (i.e. the area in which the support material and the biofilm are confined) was divided was set to 7 in this study. In order to divide the packed bed into seven fractions with the same liquid volume, the consolidation of the packed bed must be taken into account. The constant pressure to which the BIOSTYR® beads are submitted has an effect on their structure, eventually leading to deformation and to the consolidation of the packed bed. In Figure 4.3 the state of the packed bed after 4.8 years of operation can be seen. An important accumulation of biomass below the BIOSTYR® beads as well as a certain volume with no biomass growth underneath can be observed due to this consolidation, leading to an empty space on the lower part of section B of the reactor.

As a result, when the central section of the reactor (B) is divided into seven fractions (N=7) of equal liquid volume, these fractions will differ in terms of total

volume ($B_3$-$B_7$ contain support beads with attached biofilm, $B_2$ is only composed by biomass growing below the actual packed bed and $B_1$ is only occupied by liquid).

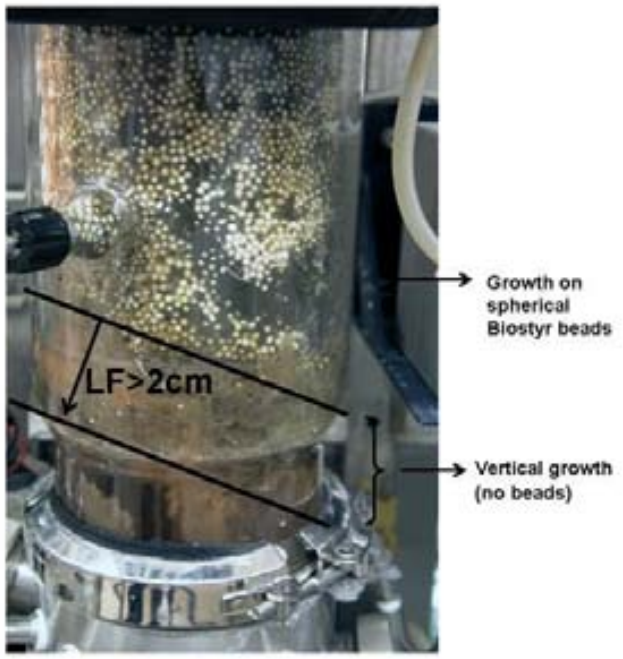


**Figure 4.3** Close up image of the reactor during its final stage of operation.

The volume left beneath the consolidated packed bed had a value of 0.86 L. Half of this volume was occupied by biofilm that grew following the direction of the vertical axis of the reactor, while the rest could be assimilated to a regular stirred tank with no growth. The volume of each one of these two zones (0.43 L) was taken as the liquid volume of each fraction. Taking into account the experimental bed porosity (0.39) and the total volume of section B (6.17 L), this yielded a total number of 7 compartments (N=7) of 0.43L of liquid volume.

The three RTD experiments performed by Pérez et al. (2005) were used to estimate the back-mixing coefficient (*f*) used to calculate the liquid back-mixing flow rate ($Q_{bmix,}$ Equation 4.26) through optimisation. The results are shown in Table 4.1.

$$Q_{bmix} = f \cdot (Q_{in} + Q_{rec}) \qquad \textbf{4.26}$$

Results of the optimisation for those experiments using a least-squares algorithm are shown in Figure 4.4. As a result, the following correlation of the liquid back-mixing flow rate ($Q_{bmix}$) as a function of recirculation flow rate ($Q_{rec}$) was obtained with a correlation coefficient of $r^2$=0.993 (Equation 4.27). All flow rates in Equations 4.26 and 4.27 should be expressed in $mL \cdot min^{-1}$.

$$Q_{bmix} = 274.99 - 2.264 \cdot Q_{rec} \qquad \textbf{4.27}$$

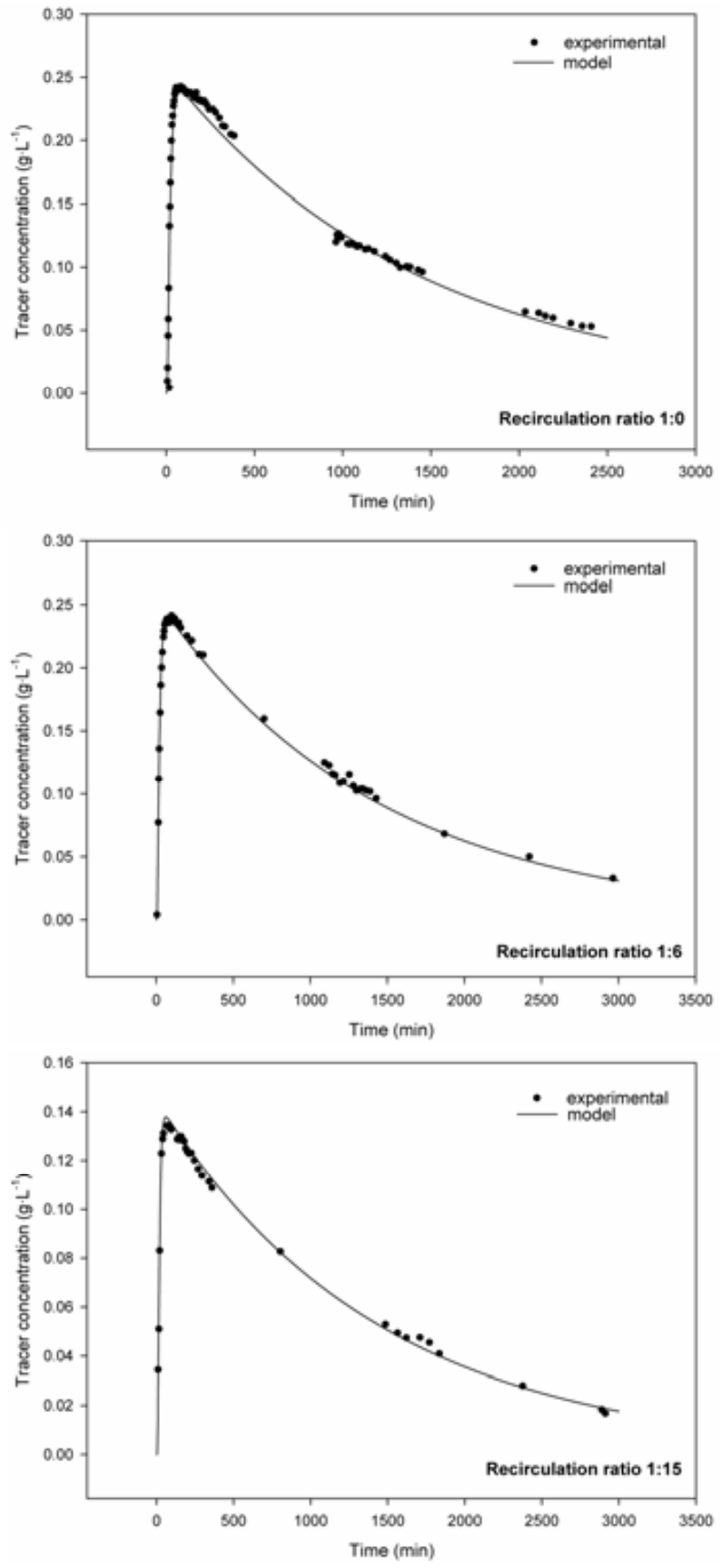


**Figure 4.4** Flow model results as obtained from optimisation with three different RTD experiments.

### 4.2.5 OUTLINE OF THE MODEL DEVELOPMENT

A very common way of modelling a biofilm reactor is by considering it as a combination of three different compartments: (i) a completely mixed compartment containing the gas phase, (ii) a completely mixed stirred tank compartment where the bulk liquid is contained and (iii) a biofilm compartment consisting of the solid cellular material i.e. the growing biofilm that gradually displaces the liquid phase.

The approach followed to develop the mathematical model consists on combining a biofilm model, which provides the description of all processes taking place within the biofilm, with a flow model used to describe the global liquid phase mixing in the reactor. This strategy has been successfully applied by other authors to describe a trickling filter (Wik, 1999 and 2003). The integration of the flow model and the biofilm model gave as a result the general structure presented in Figure 4.5.

Figure 4.5 depicts the three phases of the continuous biofilm reactor. The mass transfer processes between phases, as well as the liquid hydrodynamics along the reactor, which ultimately provide the biofilm with the necessary soluble substrates, will be taken into account as depicted in Figure 4.5.

The diffusion of soluble substrates and products between the liquid phase and the biofilm ($J_{L,i}$) is described by Fick's law. $J_G$ is the flux of gas components (e.g. oxygen) from the gas phase to the liquid phase and $J_F$ is the detachment of biofilm fragments from the biofilm and into the liquid phase. The advective links between the different liquid compartments have also been included. This structure derives from the description of the liquid phase by means of a tanks-in-series flow model, which was explained in section 4.2.4.

The progressive increase of the biofilm thickness with time due to growth is also represented in this figure and needs to be considered in the formulation of the biofilm model together with the detachment processes depicted in Figure 4.5, which originate a flux of solid material into the liquid phase. A more extensive description of all the processes taking place within the biofilm matrix was already provided in section 4.2.2.2.

In Figure 4.6 a detailed description of all the processes taking place within the biofilm is presented. The hypothetical profiles for a bacterial species Xi and soluble substrates or products (Ci) originating from the nitrification reactions (here symbolised as $r_i$) are depicted, as well as the diffusion of the soluble substrates and

products across the biofilm ($J_i$). The advective transport of the solid components, which leads to the advance of the biofilm interphase, is symbolised as LF(t).

The concentrations of all the soluble and particulate species present in the reactor at any time can then be estimated by assembling all the involved processes (stoichiometry, reaction kinetics and mass transfer) and solving the resulting mass balances in the reactor.

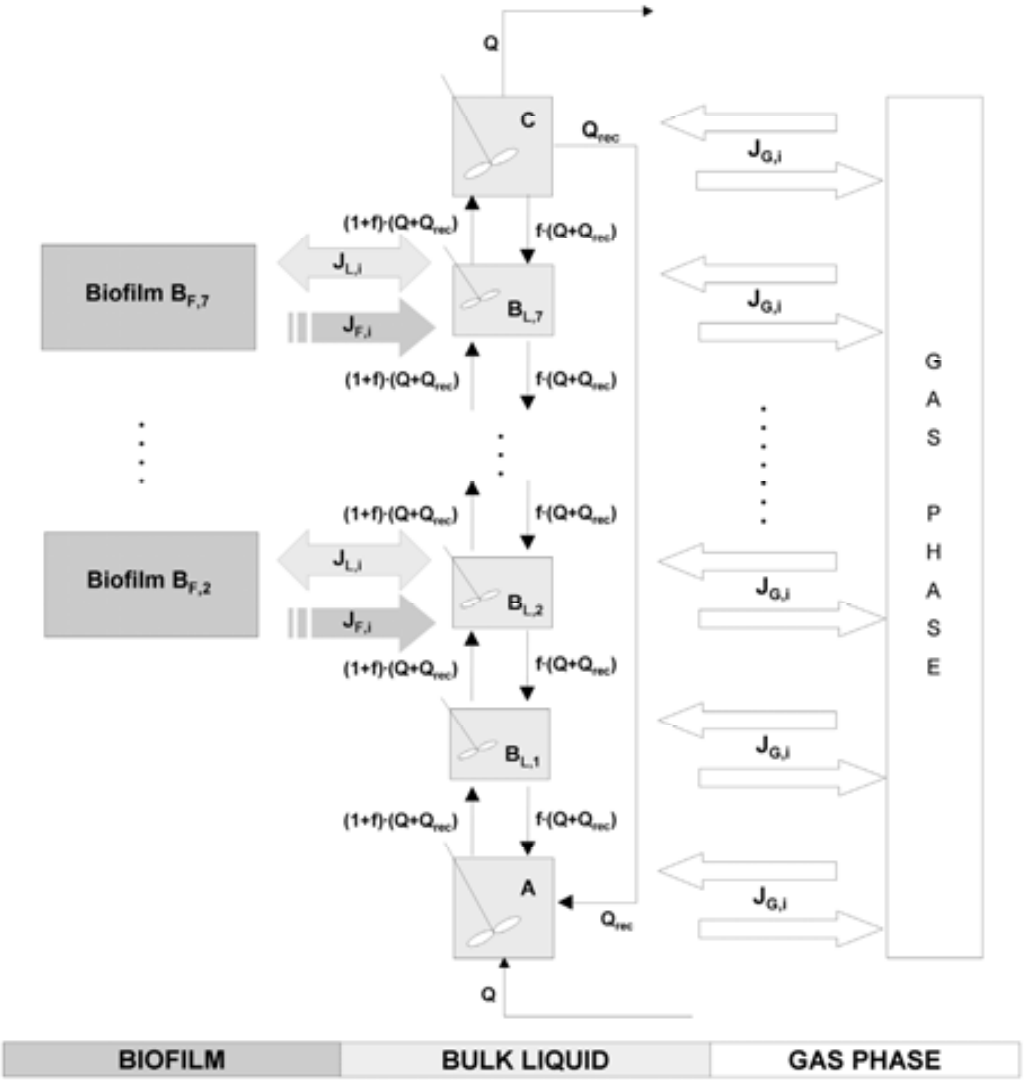


**Figure 4.5** General schematic representation of the model for the packed bed nitrifying reactor, depicting the different phases and processes taken into account for the formulation of the model. The reactor is divided in three main parts (A) is the bottom mixed compartment, (B) is the packed bed integrated by N tanks in series of equal liquid volume ($B_{L,1} = B_{L,3} = \cdot ... = B_{L,N}$) and their corresponding biofilm content ($B_{F,2}, \cdot ... B_{F,N}$).(C) is the top part of the reactor where the liquid effluent leaves the reactor (Q) and part of the liquid phase is recirculated to the bottom.($Q_{rec}$) $J_{G,i}$, $J_{L,i}$ and $J_{F,i}$ stand for the flux of the different gas, liquid and biofilm components (i) between phases.

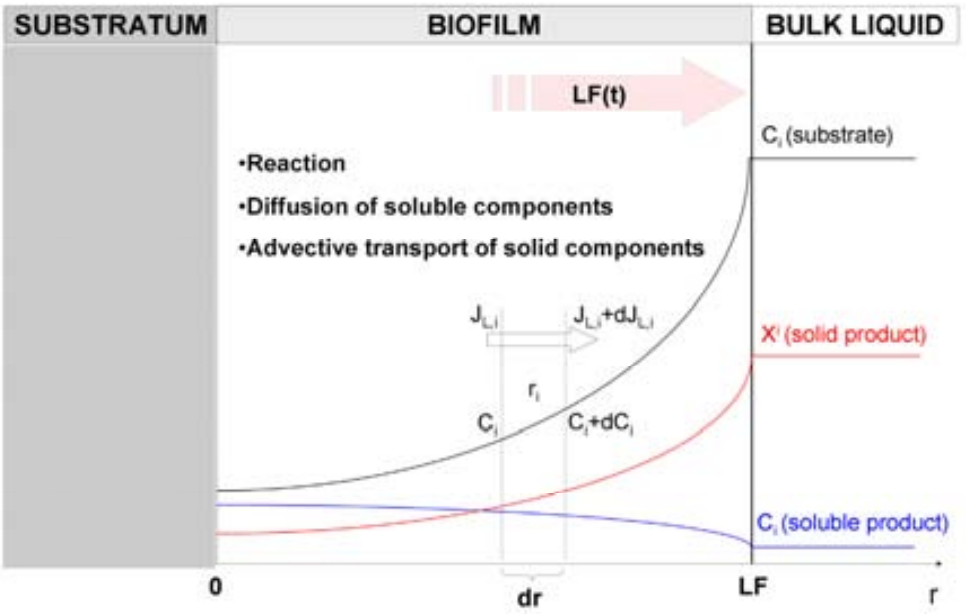


**Figure 4.6** Biofilm model: description of the main processes occurring within a portion of the biofilm. NOTE: the flux of all components was considered to be perpendicular to the spherical surface of the support beads (following the radial direction r) and the biofilm model was implemented using spherical coordinates For easier representation the figure depicts only a small portion of the biofilm surface for easier representation. $C_i$ stands for the concentration of dissolved substrates and products, $X_i$ denotes the concentration of solid species, $J_{L,i}$ symbolises the flux of a liquid species (i) and $r_i$ represents a biochemical reaction.

### 4.2.6 KINETICS AND STOICHIOMETRY

The following soluble species were considered: ammonium ($C_{NH_4^+}$), nitrite ($C_{NO_2^-}$), nitrate ($C_{NO_3^-}$), expressed as $gN \cdot L^{-1}$, dissolved oxygen ($C_{O_2}$) and soluble biodegradable substrate obtained from the hydrolysis of the biodegradable fraction of inert biomass ($C_S$).The biofilm was considered to be composed of the following particulate species: *N. europaea* ($X^{Nts}$), *N. winogradskyi* ($X^{Ntb}$), heterotrophic bacteria ($X^H$), inert biomass yielded by the biomass decay of all bacterial species present in the biofilm ($X^I$), non-biodegradable fraction of inert biomass ($X^P$), biodegradable fraction of inert biomass ($X^S$).

The main dynamic processes considered in this one-dimensional multi-species biofilm model were biomass growth, cellular maintenance and biomass decay of all bacterial species (Table 4.4, Hunik et al., 1994; Carrera et al., 2004; Henze et al., 2000). Stoichiometry coefficients of all the processes considered in this mathematical model are summarised in Table 4.5.

The bacterial species considered in this multi-species model were the two initial strains used to inoculate the reactor (*N. europaea* and *N. winogradskyi*) with the addition of a population of heterotrophic bacteria. Investigation of the microbiological composition of this nitrifying biofilm, as presented in Chapter 3 of this thesis, yielded as an important finding the presence of a proportion of heterotrophic contaminants. The predominance of *N. europaea* and *N. winogradskyi* in the nitrifying biofilm was thus confirmed.

Given the absence of any organic carbon source from the culture medium, any heterotrophic bacteria present in the biofilm could only have developed on soluble microbial products, potentially limiting the impact of the heterotrophic population on the biofilm structure and the reactor performance. Nevertheless, the inclusion of a heterotrophic population in the model definition was regarded as an interesting addition, allowing an exhaustive study of the possible effect of the presence of these bacteria on the different process parameters

#### *4.2.6.1 Kinetics of autotrophic nitrifying bacteria*

The growth of *N. europaea* and *N. winogradskyi* was considered to be limited by both the nitrogen source (i.e. $NH_4^+$ and $NO_2^-$ respectively) and the dissolved oxygen concentration. Inhibition by the respective substrates and products was also incorporated (Anthonisen et al., 1976). The study of the inhibitory effect of ammonium and nitrite on AOB and NOB performed by Anthonisen et al. (1976) pointed to free ammonia (FA) and free nitrous acid (FNA) as being the actual inhibitors of the nitrifying activity. The results of that study on the inhibiting levels of these two species as a function of pH are shown in Figure 4.7.

The pH of the medium was found to have a marked effect on the magnitude of the inhibition effect due to the equilibrium between the dissolved species ($NH_4^+$ and $NO_2^-$) and the actual inhibiting compounds (FA and FNA).

The growth rate of *N. europaea* was considered to be affected by the inhibition of its own substrate, free ammonia. Substrate inhibition kinetics was modelled with a Haldane type equation (Equation 4.28). Inhibition of the growth of *N. europaea* by FNA is not significant under the typical reactor operating conditions according to (Figure 4.7), and hence its effect was not taken into account in the kinetic equations.

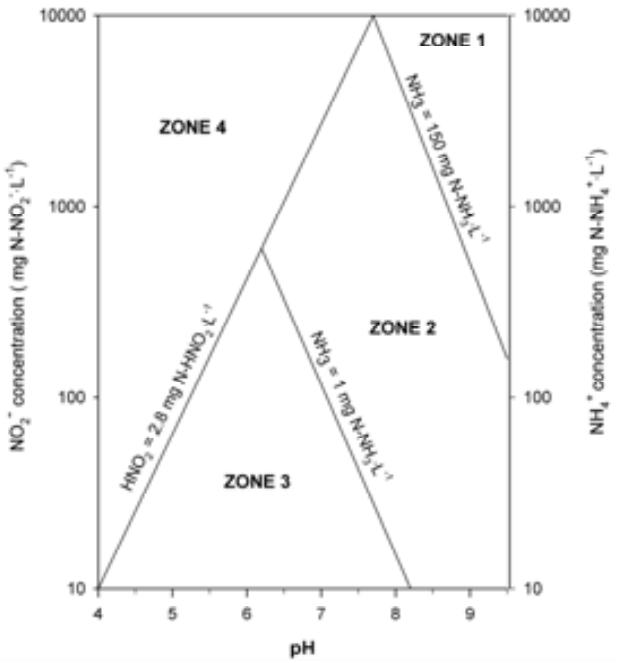


**Figure 4.7** Anthonisen inhibition diagram (Anthonisen et al., 1976).

$$\mu_{max}^{Nts} \cdot X^{Nts} \cdot \frac{C_{NH_4^+}}{K_{NH_4^+}^{Nts} + C_{NH_4^+} + \frac{C_{NH_4^+}^2}{K_{FA}^{In,Nts}}} \cdot \frac{C_{O_2}}{K_{O_2}^{Nts} + C_{O_2}} \qquad \textbf{4.28}$$

*N. winogradskyi* was considered to be inhibited non-competitively by FA, and also the inhibiting effect of the substrate (FNA) on the growth rate was considered, described by a Haldane type equation (Equation 4.29).

$$\mu_{max}^{Ntb} \cdot X^{Ntb} \cdot \frac{C_{NO_2^-}}{K_{NO_2^-}^{Ntb} + C_{NO_2^-} + \frac{C_{NO_2^-}^2}{K_{FNA}^{in,Ntb}}} \cdot \frac{C_{O_2}}{K_{O_2}^{Ntb} + C_{O_2}} \cdot \frac{K_{FA}^{n,NtbI}}{K_{FA}^{In,Ntb} + C_{NH_4^+}} \qquad \textbf{4.29}$$

### *4.2.6.2 Kinetics of heterotrophic bacteria*

The presence of heterotrophic bacteria, as indicated by the FISH analysis results, was implemented in the model. Their kinetics and stoichiometry were described following the indications of the activated sludge models ASM1 and ASM2 (Henze et al., 2000). The growth of heterotrophic bacteria was described by two consecutive processes. The hydrolysis of slowly biodegradable products ($X^S$), consisting mostly of the biodegradable fraction of the biomass derived from decay, to readily biodegradable substrate ($C_S$). The product of the hydrolysis process (Equation 4.30) is then used by heterotrophic bacteria following Monod type kinetics with a double limitation by oxygen and readily biodegradable carbon source (Equation 4.31).

$$k_h \cdot \frac{X^S / X^H}{K_{X^S}^H + X^S / X^H} \cdot \frac{C_{O_2}}{K_{O_2}^H + C_{O_2}} \cdot X^H \qquad \textbf{4.30}$$

$$\mu_{max}^H \cdot X^H \cdot \frac{C_S}{K_S^H + C_S} \cdot \frac{C_{O_2}}{K_{O_2}^H + C_{O_2}} \qquad \textbf{4.31}$$

#### *4.2.6.3 Stoichiometric and kinetic parameters*

The main parameters defining the stoichiometry and kinetics of all the involved processes are shown in Table 4.2. The affinity constants and inhibition constants of *N. europaea* and *N. winogradskyi* were obtained from the literature (Hunik et al., 1994; Carrera et al., 2004) and adapted to the operational conditions of this nitrifying reactor when necessary according to the pH value or temperature as described hereafter.

**Table 4.2** Kinetic and stoichiometric parameters for nitrifying bacteria (28ºC and pH=8). All inhibition constants of nitrifying bacteria calculated with the $NH_4^+$-$NH_3$ equilibrium and with the $NO_2^-$free nitrous acid equilibrium.

| Symbol | Units | *Nitrosomonas europaea* ($X_{Nts}$) | *Nitrobacter winogradskyi* ($X_{Ntb}$) | Reference |
|---|---|---|---|---|
| $K_{NH_4^+}^{Nts}$ | g N-$NH_4^+$·$L^{-1}$ | 0.0175 | | Hunik et al. (1992) |
| $K_{NO_2^-}^{Ntb}$ | g N-$NO_2^-$·$L^{-1}$ | | $5.04 \cdot 10^{-3}$ | Hunik et al. (1993a) |
| $K_{O_2}^{Nts}$ | g $O_2$·$L^{-1}$ | $1.616 \cdot 10^{-4}$ | | Hunik et al. (1993b) |
| $K_{O_2}^{Ntb}$ | g $O_2$·$L^{-1}$ | | $5.44 \cdot 10^{-4}$ | Wijffels et al. (1991) |
| $K_{FA}^{In,Nts}$ ***a*** | g FA·$L^{-1}$ | 0.116 | | Carrera (2001) |
| $K_{FA}^{In,Ntb}$ ***b*** | g FA·$L^{-1}$ | | $5.2 \cdot 10^{-4}$ | Carrera et al. (2004) |
| $K_{FNA}^{In,Ntb}$ | g FNA·$L^{-1}$ | | $1.56 \cdot 10^{-4}$ | Hunik et al. (1993a) |
| $Y_{X/S}^{Nts}$ | g VSS $g^{-1}$ N-$NH_4^+$ | 0.119 | | Hunik et al. (1994) |
| $Y_{X/S}^{Ntb}$ | g VSS $g^{-1}$ N-$NO_2^-$ | | 0.0414 | Wijffels et al. (1991) |
| $\mu_{max}^{Nts}$ | $d^{-1}$ | 1.368 | | Hunik et al. (1994) |
| $\mu_{max}^{Ntb}$ | $d^{-1}$ | | 0.864 | Wijffels et al. (1991) |
| $m^{Nts}$ | gN $g^{-1}$VSS $d^{-1}$ | 1.137 | | Hunik et al. (1994) |
| $m^{Ntb}$ | gN $g^{-1}$VSS $d^{-1}$ | | 2.661 | Wijffels et al. (1991) |

In the case of the inhibition constants of the nitrifying bacteria, the actual inhibiting species being either free ammonia (FA) or free nitrous acid (FNA), the constant values had to be recalculated by means of Equations 4.32 at the temperature and pH of operation in the reactor (28ºC and pH=8).

$$C_{FA} = \frac{(17/14)\cdot C_{NH_4^+}\cdot 10^{pH}}{K_b/K_w + 10^{pH}} \qquad \textbf{4.32}$$

Where $C_{FA}$ stands for the free nitrous acid concentration expressed in $g\,NH_3\cdot L^{-1}$, $C_{NH_4^+}$ denotes the concentration of nitrogen as ammonium in $gN-NH_4^+\cdot L^{-1}$, $K_b$ and $K_w$ are the ionization constants of ammonium and water respectively. They can be calculated by means of Equation 4.33.

$$K_b/K_w = e^{\left(\frac{6344}{273+T(^oC)}\right)} \qquad \textbf{4.33}$$

Similarly free nitrous acid concentration is calculated from the nitrite ($NO_2^-$) concentration dissolved in the medium by means of Equations 4.34.

$$C_{FNA} = \frac{(47/14)\cdot C_{NO_2^-}}{K_a\cdot 10^{pH}} \qquad \textbf{4.34}$$

Where $C_{FNA}$ is the concentration of free nitrous acid expressed in $g\,HNO_2\cdot L^{-1}$, $C_{NO_2^-}$ stands for the nitrogen as nitrite concentration $\left(gN-NO_2^-\cdot L^{-1}\right)$, $K_a$ is the ionization constant for nitrite, calculated using Equation 4.35 (Anthonisen et al., 1976).

$$K_a = e^{\left(\frac{-2300}{273+T(^oC)}\right)} \qquad \textbf{4.35}$$

The parameters relating to heterotrophic bacteria and to the hydrolysis of the biodegradable fraction of inert biomass ($X^S$) to soluble biodegradable substrate ($C_S$) were obtained from the literature (Henze et al., 2000) and are shown in Table 4.3. The maximum specific growth rate ($\mu_{max}$) and the decay rate ($b_H$) of heterotrophic bacteria are known to be dependent on the temperature. Their values at the operational conditions of the reactor, i.e. 28ºC, can be calculated with equations 4.36 and 4.37 (Henze et al., 2000). Where T is the temperature (ºC) and $\mu_{max}$ and $b_H$ are obtained in $d^{-1}$.

$$\mu_{max} = 6 \cdot (1.07)^{(T-20)} \quad \textbf{4.36}$$

$$b_H = 0.4 \cdot (1.07)^{(T-20)} \quad \textbf{4.37}$$

**Table 4.3** Kinetic and stoichiometric parameters for heterotrophic bacteria. All parameters obtained from Henze et al. (2000).

| Symbol | Units | Heterotrophic bacteria ($X_H$) | Biodegradable inert biomass ($X_S$) |
|---|---|---|---|
| $Y^H_{X/S}$ | g VSS $g^{-1}$ VSS | 0.67 | |
| $K^H_S$ | gCOD $L^{-1}$ | 0.004 | |
| $K^H_{O_2}$ | g $O_2$ $L^{-1}$ | $2 \cdot 10^{-3}$ | |
| $\mu^H_{max}$ | $d^{-1}$ | 10.31 | |
| $b^H$ | $d^{-1}$ | 0.69 | |
| $f_P$ | g COD $g^{-1}$ COD | 0.08 | |
| $k_h$ | g COD $g^{-1}$ COD $d^{-1}$ | | 3 |
| $K^H_{XS}$ | g COD $g^{-1}$ COD | | 0.03 |

### 4.2.7 IMPLEMENTATION OF THE MODEL IN AQUASIM

As mentioned above, the biofilm compartment as defined by AQUASIM consists of three different zones: (i) bulk liquid, which is considered as a perfectly mixed liquid phase through which the substrates diffuse to the biofilm, (ii) biofilm matrix and (iii) biofilm pore water. In aerobic processes such as this, in which oxygen gas is supplied to the reactor, the transport of oxygen from the gas phase into the liquid phase also needs to be accounted for. A scheme depicting the different phases and the processes taking place between them in the bioreactor was presented in Figure 4.5.

The reactor was modelled in AQUASIM as a combination of completely mixed and biofilm compartments connected by advective links (Figure 4.2, Figure 4.5). The top section (A) and the bottom section (C) of the reactor were described as completely mixed compartments where no biofilm growth was taking place. The central part (B) of the reactor was comprised of N (where N was set to 7) tanks ($B_1$-$B_7$). The lowest one of these compartments ($B_1$ in Figure 4.2) was thus defined as a completely mixed compartment (i.e. no biofilm growth was taking place) to simulate the consolidation of the support material due to pressure (Figure 4.2), while the six remaining fractions were described as biofilm compartments. In the lowest of the six tanks with biofilm growth ($B_2$), the biofilm was assumed to develop on the direction of the vertical axis only (as evidenced by experimental observation, Figure 4.3). In the five remaining packed bed sub-compartments ($B_3$-$B_7$) growth was considered to

take place on the spherical surface of the support beads, considering spherical coordinates (i.e. the biofilm grew on the surface of the spherical substratum and expands radially from the surface).

**Table 4.4** Kinetics of all dynamic processes and involved in the mathematical model including heterotrophic bacteria. (Hunik et al., 1994; Carrera et al., 2004; Henze et al., 2000).

| Process | Rate Equations |
|---|---|
| Growth of *N. europaea* on $NH_4^+$ | $\mu_{max}^{Nts} \cdot X^{Nts} \cdot \frac{C_{NH_4^+}}{K_{NH_4^+}^{Nts} + C_{NH_4^+} + \frac{C_{NH_4^+}^2}{K_{FA}^{In,Nts}}} \cdot \frac{C_{O_2}}{K_{O_2}^{Nts} + C_{O_2}}$ |
| Growth of *N. winogradskyi* on $NO_2^-$ | $\mu_{max}^{Ntb} \cdot X^{Ntb} \cdot \frac{C_{NO_2^-}}{K_{NO_2^-}^{Ntb} + C_{NO_2^-} + \frac{C_{NO_2^-}^2}{K_{FNA}^{in,Ntb}}} \cdot \frac{C_{O_2}}{K_{O_2}^{Ntb} + C_{O_2}} \cdot \frac{K_{FA}^{n,NtbI}}{K_{FA}^{In,Ntb} + C_{NH_4^+}}$ |
| Growth of heterotrophic bacteria | $\mu_{max}^{H} \cdot X^{H} \cdot \frac{C_S}{K_S^H + C_S} \cdot \frac{C_{O_2}}{K_{O_2}^H + C_{O_2}}$ |
| Decay of *N. europaea* | $Y_{X/S}^{Nts} m^{Nts} X^{Nts} \left[ 1 - \frac{C_{NH_4^+}}{K_{NH_4^+}^{Nts} + C_{NH_4^+} + \frac{C_{NH_4^+}^2}{K_{FA}^{In,Nts}}} \cdot \frac{C_{O_2}}{K_{O_2}^{Nts} + C_{O_2}} \right]$ |
| Decay of *N. winogradskyi* | $Y_{X/S}^{Ntb} m^{Ntb} X^{Ntb} \left[ 1 - \frac{C_{NO_2^-}}{K_{NO_2^-}^{Ntb} + C_{NO_2^-} + \frac{C_{NO_2^-}^2}{K_{FNA}^{In,Ntb}}} \cdot \frac{C_{O_2}}{K_{O_2}^{Ntb} + C_{O_2}} \cdot \frac{K_{FA}^{In,Ntb}}{K_{FA}^{In,Ntb} + C_{NH_4^+}} \right]$ |
| Decay of heterotrophic bacteria | $b^H \cdot X^H$ |
| *N. europaea* maintenance | $m^{Nts} X^{Nts} \frac{C_{NH_4^+}}{K_{NH_4^+}^{Nts} + C_{NH_4^+} + \frac{C_{NH_4^+}^2}{K_{FA}^{In,Nts}}} \cdot \frac{C_{O_2}}{K_{O_2}^{Nts} + C_{O_2}}$ |
| *N. winogradskyi* maintenance | $m^{Ntb} X^{Ntb} \frac{C_{NO_2^-}}{K_{NO_2^-}^{Ntb} + C_{NO_2^-} + \frac{C_{NO_2^-}^2}{K_{FNA}^{In,Ntb}}} \cdot \frac{C_{O_2}}{K_{O_2}^{Ntb} + C_{O_2}} \cdot \frac{K_{FA}^{n,NtbI}}{K_{FA}^{In,Ntb} + C_{NH_4^+}}$ |
| Hydrolysis of $X_S$ | $k_h \cdot \frac{X^S / X^H}{K_{X^S}^H + X^S / X^H} \cdot \frac{C_{O_2}}{K_{O_2}^H + C_{O_2}} \cdot X^H$ |

**Table 4.5** Stoichiometry coefficients of the dynamic processes involved in the mathematical model.

| Bacterial species | $C_{NH_4^+}$ | $C_{NO_2^-}$ | $C_{NO_3^-}$ | $C_{O_2}$ | $C_S$ | $X^{Nts}$ | $X^{Ntb}$ | $X^H$ | $X^I$ | $X^P$ | $X^S$ |
|---|---|---|---|---|---|---|---|---|---|---|---|
| Growth of *N. europaea* on $NH_4^+$ | $-1/Y^{Nts}_{X/S}$ | $1/Y^{Nts}_{X/S}$ | | $-3.43/Y^{Nts}_{X/S}$ | | 1 | | | | | |
| Growth of *N. winogradskyi* on $NO_2^-$ | | $-1/Y^{Ntb}_{X/S}$ | $1/Y^{Ntb}_{X/S}$ | $-1.14/Y^{Ntb}_{X/S}$ | | | 1 | | | | |
| Growth of heterotrophic bacteria | | | | $-(1-Y^H_{X/S})/Y^H_{X/S}$ | $-1/Y^H_{X/S}$ | | | 1 | | | |
| Decay of *N. europaea* | | | | | | -1 | | | 1 | $f_P$ | $(1-f_P)$ |
| Decay of *N. winogradskyi* | | | | | | | -1 | | 1 | $f_P$ | $(1-f_P)$ |
| Decay of heterotrophic bacteria | | | | | | | | -1 | 1 | $f_P$ | $(1-f_P)$ |
| *N. europaea* maintenance | -1 | 1 | | -3.43 | | | | | | | |
| *N. winogradskyi* maintenance | | -1 | 1 | -1.14 | | | | | | | |
| Hydrolysis of $X_S$ | | | | | 1 | | | | | | -1 |

## 4.2.8 MODEL SIMULATION

### *4.2.8.1 Numerical parameters and integration settings*

The need to solve partial differential equations in such a complex system was overcome by discretising the space, i.e. the biofilm thickness, using a grid with a specified number of divisions. The number of divisions is to be set depending on the required length of the simulated period and on the required accuracy. Due to the length of the reactor operational periods analysed in this study, the selected degree of discretisation is a compromise between accuracy and computational. For most of the simulations performed in this study a grid of 20-30 divisions was applied to all fractions except for fraction $B_2$ of the packed bed, where the biofilm thickness was remarkably higher. In the latter case a grid with 30 to 40 divisions was used.

### *4.2.8.2 Input data and initial conditions*

A summary of the main parameters related to biofilm structure and to the diffusive transport of substrates and products through the bulk liquid and into the biofilm can be found in Table 4.6.

The inflow ammonium concentrations and inflow rates were defined based on the measurements during the complete period of reactor operation (real list variables). These data sets allowed simulations covering the whole range of operational conditions applied over the complete period of reactor operation (Figure 5.1). The liquid recirculation ratio was 1:6 ($Q_{in}$:$Q_{rec}$).

A biofilm thickness of 10 μm was set as the initial value for this parameter. The inoculum was assumed to contain 67% of *N. europaea* and 33% of *N. winogradskyi* in all biofilm compartments ($B_2$ to $B_7$). This value was selected taking into account the growth yields of both bacterial populations (*N. europaea* and *N. winogradskyi*) as obtained from the literature (Hunik, 1993).

The six biofilm compartments were defined as having a reactor volume of 0.397dm$^3$. In the first biofilm compartment ($B_2$), where the biofilm grew along the vertical direction only, the cross-sectional area of the packed bed was set to a constant value and was calculated as 1.13 dm$^2$. Parameters required for the definition of the biofilm compartments are presented in Table 4.6.

Two of the main parameters needed to define biofilm structure are biofilm porosity and biofilm density. Biofilm porosity is a complex concept, thus the correlation between its value and other characteristic parameters of the biofilm structure, have only recently been studied (Lewandowski, 2000). Biofilm density

depends on the composition of the bacterial population of the biofilm, but also on other factors such as the age and composition of the biofilm or the presence of EPS (Laspidou and Rittmann, 2004a). A wide diversity of values has been reported for biofilm density in nitrifying biofilm which depends on the biofilm bacterial composition among other factors (Horn et al., 2002; Terada et al., 2006).

**Table 4.6** Parameters used in the definition of the biofilm. (a) When more than one reference is provided, an average value has been used. (b) the same biofilm density was assumed for all the species conforming the biofilm ($\rho=\rho^{Nts}=\rho^{Ntb}=\rho^{H}=\rho^{I}$).

| Parameter | Symbol | Units | Value | Reference[(a)] |
|---|---|---|---|---|
| Diffusivity of $NH_4^+$ | $D_{NH_4^+}$ | $dm^2\ d^{-1}$ | $1.6\cdot10^{-2}$ | Terada et al., 2006<br>Bernet et al., 2005 |
| Diffusivity of $NO_2^-$ | $D_{NO_2^-}$ | $dm^2\ d^{-1}$ | $1.7\cdot10^{-2}$ | Terada et al., 2006<br>Bernet et al., 2005 |
| Diffusivity of $NO_3^-$ | $D_{NO_3^-}$ | $dm^2\ d^{-1}$ | $1.5\cdot10^{-2}$ | Terada et al., 2006<br>Bernet et al., 2005 |
| Diffusivity of $O_2$ | $D_{O_2}$ | $dm^2\ d^{-1}$ | $1.8\cdot10^{-2}$ | Terada et al., 2006<br>Bernet et al., 2005 |
| Biofilm porosity | $\theta$ | dimensionless | 0.40 | This study |
| Biofilm density [(b)] | $\rho$ | $g\ L^{-1}$ | 160 | This study |

A value of 160 $g\cdot L^{-1}$ was assumed in this study for the biofilm density, which is higher than most reported values. This value originates from the experimental determination of the dry weight of the biofilm in the different packed bed fractions. The high biofilm density that needs to be assumed in this study is believed to be a result of the inner biofilm consolidation and development history of this specific biofilm. Laspidou and Rittmann (2004a) modelled the development of biofilm density and evaluated its trends at different stages of the biofilm life (Laspidou and Rittmann, 2004b). Their modelled results indicate an increase of biofilm density with consolidation, older biofilms having greater densities than younger ones, and density being higher in the inner part of the biofilm where inert biomass accumulates. Densities between 150-170 $g\cdot L^{-1}$ were estimated for old biofilms. Since the available experimental information for the biofilm studied in the present work was obtained after close to 5 years of operation, it was reasonable to assume a biofilm density of 160 $g\cdot L^{-1}$, which was in agreement with the results reported for old, thick biofilms and correlated well with the measured values of the dry weight.

Finally, a biofilm porosity of 0.4 was used in this study, which is a result of the biofilm density of 160 $g\cdot L^{-1}$ and the assumed inoculum composition of 67% of *N. europaea* and 33% of *N. winogradskyi*

#### *4.2.8.3 Biomass detachment from the biofilm*

Several expressions reported in the literature were tested for the definition of the detachment rate and a number of them were found to produce good results. The detachment rate ($u_{det}$, $dm \cdot d^{-1}$) was finally modelled as being dependent on the biofilm growth velocity ($u_F$) and $LF_{max}$ through Equation 4.38. After verifying that different values of the exponent (i.e. 2, 3, 4, 5) produced equally good results, the exponent 2, which has been widely used in the literature (Wanner and Gujer, 1986; Chambless and Stewart, 2007; Lackner et al., 2007), was finally selected for its simplicity.

$$u_{det} = (LF/LF_{max})^2 \cdot u_F \quad \text{when } u_F > 0 \text{ (otherwise } u_F = 0) \qquad \textbf{4.38}$$

# CHAPTER 5

# EVALUATION OF THE REACTOR NITRIFYING EFFICIENCY AND THE DISTRIBUTION OF NITRIFYING BACTERIA ALONG THE PACKED BED THROUGH MATHEMATICAL MODELLING

## *Foreword*

*The mathematical model developed in Chapter 4 is applied to the study of the reactor operation and the structure of the autotrophic nitrifying biofilm. In the present chapter the model is applied to the steady state without prior parameter optimisation. The main conclusions drawn from the experimental study performed in Chapter 3 is compared to the results of the model simulations in terms of nitrifying efficiency of the reactor as well as the relative abundance of N. europaea and N. winogradskyi at the final steady state achieved after 4.8 years of continuous operation. A number of parameters potentially affecting the segregation of the two bacterial species involved in this two-step nitrification process is targeted and their effect on the relative abundance profile along the packed bed height is studied, leading to the identification of the main factors causing the segregation of AOB and NOB along the vertical axis of the packed bed.*

## 5.1 INTRODUCTION

The application of different molecular techniques to the study of a nitrifying biofilm (Chapter 3) yielded relevant information on the distribution of the different bacterial species on the macroscale, i.e. along the vertical axis of the packed bed, after long term operation (1750 d). In addition, experimental data on the reactor efficiency throughout the whole period of operation were also available for analysis.

Modelling of multi-species biofilms with different levels of complexity is well reported in the literature (Wanner and Reichert, 1996; Gheewala et al., 2004; Terada et al., 2006). However, the use of biofilm models to predict the spatial distribution of different bacterial populations on the macroscale in reactors similar to the packed bed reactor used in the present study, and the effect of operational or structural parameters on this heterogeneity, is not so well documented and has only been reported in a few recent works (Fdz-Polanco et al., 2000; Wik, 2003; Lydmark et al., 2006; Yun and Kim, 2003). Furthermore, experimental results on the biomass distribution have been only very rarely compared to those predicted by a mathematical model.

The biofilm model developed in Chapter 4 can be used to simulate the final steady state achieved after 1750 days of operation and to assess the relative abundance of *N. europaea* and *N. winogradskyi* along the packed bed vertical axis. An appropriate model would allow the simulation of different scenarios and the assessment of the effect of different parameters on the final biomass profile.

## 5.2 OBJECTIVES

The model developed in Chapter 4 will be used in this chapter to predict the behaviour of the liquid phase and the biofilm under steady state conditions, focusing on long term operation results. The following goals have been established:

- Assessment of the nitrifying efficiency and of the spatial distribution of *N. europaea* and *N. winogradskyi* along the packed bed under steady state using the mathematical model.
- Identify the correlation between the modelled results and the experimental data yielded by experimental analysis using molecular methods.

- Assessment of the effect of different parameters on the final biomass profiles along the packed bed vertical axis.

## 5.3 MATERIAL AND METHODS

### 5.3.1 OPERATIONAL CONDITIONS

Experimental data used in this study were obtained during the last testing period of the nitrifying pilot reactor of the MELiSSA CIII. The bioreactor was inoculated with an axenic co-culture of *N. europaea* (ATCC 19718) and *N. winogradskyi* (ATCC 25391). The start up was carried out by gradually increasing the ammonium load, either by changing the ammonium concentration in the feeding solution or by increasing the input flow rate. In the operational period studied in the present work, the start up process lasted around 45 days.

The reactor was operated with a residence time of 80 h for 30 days and subsequently decreased to 54 h (Pérez, 2001). The reactor was fed under sterile conditions throughout the whole period of operation and different conditions were applied over a total time of 1750 days (i.e. 4.8 years). During this extended operational period different ammonium loads were tested, allowing evaluation of the reactor efficiency under a wide range of operational conditions. The main ammonium loads and flow rates are depicted in Figure 5.1.

### 5.3.2 INTEGRATION SETTINGS

The thickness of the biofilm was discretised using a grid with 20 or 30 divisions for the long term simulations presented in the present chapter.The lower discretisation (30-division grid) was applied to the bottom fraction of the packed bed ($B_2$), where the biofilm thickness was markedly higher, while a 20-division grid was used in all remaining fractions ($B_3$-$B_7$). These settings led to a simulation time of 71 minutes for 60 days of operation on an Intel® Pentium® D CPU at 3.00 GHz.

## 5.4 APPLICATION OF THE MODEL TO STEADY STATE

The first goal set for the developed model was to reproduce the results of the biofilm community analysis presented in Chapter 3. For this application, simulations were run without any previous parameter optimisation, using literature values as the main inputs for all kinetic, stoichiometric or biofilm characteristic parameters as described in Chapter 4.

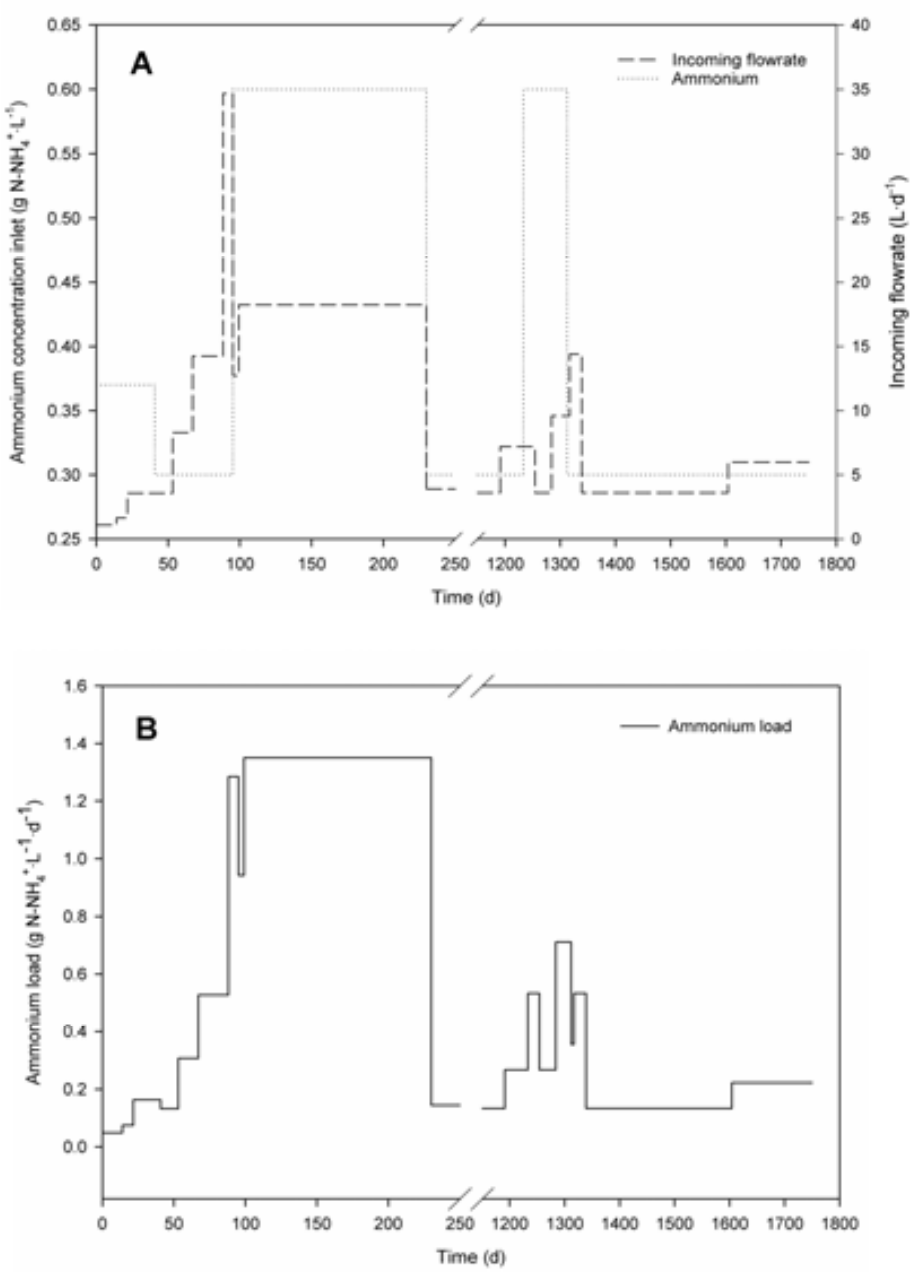


**Figure 5.1** Operational conditions in the reactor along the whole analysed period of continuous operation. (A) Incoming flow rate and ammonium concentration. (B) Input ammonium load.

Since the results of the experimental biofilm analysis were obtained at the time when the reactor operation was stopped (i.e. at time 1750 days), the study of the solid phase was mainly focussed on the final stage of operation (1300-1750 days), when the reactor had been operating under the same conditions for several months. In this scenario, all parameters, including those related to the biofilm, can be considered to have achieved the steady state and thus to remain constant.

Since experimental data of ammonium, nitrite and nitrate concentration were available for all the different steady states depicted in Figure 4.5, this information

was used to validate the accuracy of the model predictions in steady state regarding the efficiency of the conversion of ammonium to nitrate.

### 5.4.1 MAIN ASSUMPTIONS

The main aim in the present section is the evaluation of the model performance in steady state and, most importantly, during the last few days of operation of the reactor. Therefore, in addition to the general assumptions extensively discussed in Chapter 4, the values of the $K_L \cdot a$ and the oxygen saturation concentration used in this section are those calculated in the final conditions of the reactor operation, i.e. at a time of 1750 days. The estimated values of the $K_L \cdot a$ and the oxygen saturation in the different parts of the reactor at that time can be found in Table 5.1. they were considered constant throughout the whole operational period of the reactor.

**Table 5.1** Volumetric gas-liquid mass transfer coefficient ($K_L \cdot a$) and oxygen saturation concentration ($C_{O_2}^{sat}$) in the different fractions of the packed-bed after 1750 days operation.

| Fraction | Bottom (sectionA) | B1 | B2 | B3 | B4 | B5 | B6 | B7 | Top (sectionC) |
|---|---|---|---|---|---|---|---|---|---|
| $K_L \cdot a$ **($h^{-1}$)** | 64.8 | 85.5 | 85.5 | 609 | 244 | 220 | 198 | 179 | 50.4 |
| $C_{O_2}^{sat} \cdot 10^3$ **(g $L^{-1}$)** | 8.99 | 8.79 | 8.64 | 8.35 | 8.02 | 7.79 | 7.57 | 7.36 | 7.21 |

### 5.4.2 ANALYSIS OF THE NITRIFYING EFFICIENCY

Although the main focus of the work presented in this section was directed at studying long term results, the capacity of the model to predict the nitrifying efficiency of the different steady states achieved along the complete operational period was also investigated. The experimental concentrations of the soluble substrates and products measured at the different steady states achieved during this 1750-day time span in which the reactor was kept under continuous operation (Pérez et al., 2004) have been compared with the predictions of the model developed in the present study.

The experimental efficiencies of the ammonia oxidation to nitrite (nitritation) as well as the total efficiency of the two-step oxidation to nitrate are listed in Table 5.2 alongside the results predicted by the model, showing differences in the oxidation efficiencies of less than 0.5% in all listed steady states. Therefore, it can be concluded that the nitrifying efficiency was close to 100% during the complete operation of the reactor and that the results obtained with the model showed a good correlation with the experimental results under the tested conditions.

### 5.4.3 ANALYSIS OF LONG TERM STEADY STATE RESULTS

As previously stated, the complete analysis of the solid phase of the biofilm reactor was focussed on the last of the steady states achieved in this extended operational period. Two main reasons motivated the selection of this final steady state to perform this study. First of all the information obtained at this stage of the operation is valuable due to the length of this operation run, which enabled us to study long term reactor behaviour. The second reason has to do with the actual hardware limitations of the reactor and the possibility to obtain biofilm samples. Since it is essential that the reactor operates under axenic conditions, and due to the confinement of the biofilm inside the packed bed, it was not possible to harvest biomass samples from the biofilm without compromising the axenicity of the reactor. Therefore, the termination of the reactor operation provided the opportunity to perform an exhaustive experimental evaluation of the biofilm structure and composition (Chapter 3).

During this final stage of the reactor operation, the input ammonium load was 0.22 $g \cdot L^{-1} d^{-1}$ (Table 5.2, see row highlighted with grey background). The substrate degradation predicted by the model (total nitrogen removal efficiency of 99.1%) was in agreement with the experimental results (99.4%) as well as the partial oxidation of ammonia to nitrite, which produced similar results (0.2% difference between the experimental and modelled efficiencies). The ammonium load during the last few months of operation was kept low due to the limitations of the reactor performance, mostly due to the advanced clogging of the packed bed, which would eventually lead to significant nitrite accumulation if higher loads were applied.

**Table 5.2** Conversion rates in the reactor at different ammonium loads (*load referred to total reactor volume). The second row of the table is highlighted with a grey background for future reference in section 5.4.3.

| Liquid flowrate ($L \cdot d^{-1}$) | Influent $NH_4^+$ concentration ($g\ N\text{-}NH_4^+\ L^{-1}$) | *Influent $NH_4^+$ load ($g\ L^{-1}\ d^{-1}$) | *Effluent $NH_4^+$ load ($g \cdot L^{-1} \cdot d^{-1}$) | | Total $NH_4^+$ load oxidation (%) | | *Effluent $NO_2^-$ load ($g \cdot L^{-1} \cdot d^{-1}$) | | Conversion of $NH_4^+$ load to $NO_3^-$ (%) | |
|---|---|---|---|---|---|---|---|---|---|---|
| | | | Exp. | Model | Exp. | Model | Exp. | Model | Exp. | Model |
| 3.6 | 0.3 | 0.13 | $2.3 \cdot 10^{-4}$ | $6.1 \cdot 10^{-4}$ | 99.8 | 99.5 | $3 \cdot 10^{-4}$ | $2.6 \cdot 10^{-4}$ | 99.6 | 99.3 |
| 6.0 | 0.3 | 0.22 | $8.7 \cdot 10^{-4}$ | $1.3 \cdot 10^{-3}$ | 99.6 | 99.4 | $5.2 \cdot 10^{-4}$ | $6.8 \cdot 10^{-4}$ | 99.4 | 99.1 |
| 7.2 | 0.3 | 0.27 | $9 \cdot 10^{-5}$ | $1.6 \cdot 10^{-3}$ | 99.9 | 99.4 | $2.7 \cdot 10^{-5}$ | $8.1 \cdot 10^{-4}$ | 99.9 | 99.1 |
| 14.3 | 0.3 | 0.53 | $8.8 \cdot 10^{-4}$ | $3.3 \cdot 10^{-3}$ | 99.8 | 99.4 | $2.7 \cdot 10^{-3}$ | $1.6 \cdot 10^{-3}$ | 99.3 | 99.1 |
| 12.7 | 0.6 | 0.94 | $7.9 \cdot 10^{-4}$ | $1.7 \cdot 10^{-3}$ | 99.9 | 99.8 | $1.1 \cdot 10^{-3}$ | $4.9 \cdot 10^{-3}$ | 99.8 | 99.3 |
| 34.7 | 0.3 | 1.28 | $1.2 \cdot 10^{-2}$ | $3.8 \cdot 10^{-3}$ | 99.1 | 99.6 | $4.8 \cdot 10^{-2}$ | $2.3 \cdot 10^{-1}$ | 95.3 | 75.8 |

### 5.4.3.1 *Biomass concentration along the packed bed*

Experimental results presented in Chapter 3 showed a gradual decrease of the total biomass concentration with increasing height along the packed bed.

In Figure 5.2 an illustration of the division of the packed bed into different fractions is presented in terms of total volume (i.e. liquid+solid volume) and scaled with the actual bed heights. The volumes of the experimental fractions were determined as explained in Chapter 3, while the definition of the volumes of the fractions used in the mathematical model can be found in Chapter 4. The biomass concentration estimated with the model at different heights along the packed bed (fractions $B_2$-$B_7$) is depicted in the graph alongside the experimental values estimated for fractions $F_1$-$F_7$ (bar chart). A good correlation is observed between the experimental results and the profile obtained through simulation with the new AQUASIM model. The good correspondence of the modelled results with the experimental data indicates that the model was capable of predicting the gradient of biomass concentration along the packed bed.

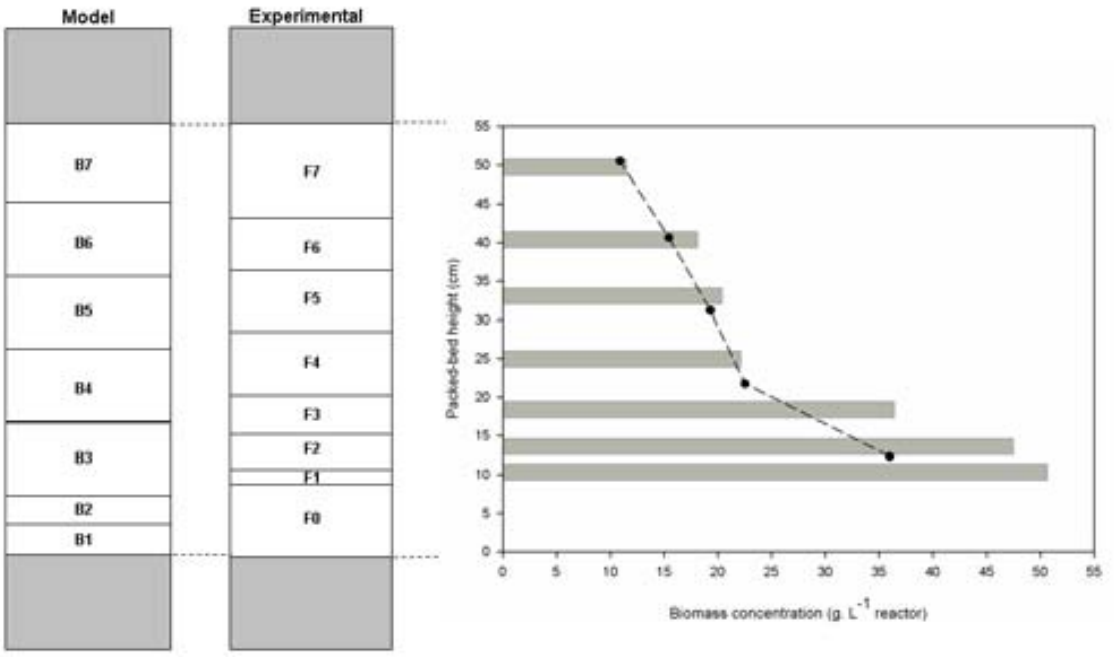


**Figure 5.2** Biomass concentration in the packed-bed as a function of the position along the vertical axis, estimated using mathematical modelling (•) and experimental measurements (bar chart) after reactor dismantling. A comparative scheme of the fractions as defined for mathematical modelling (Model) and fraction volumes from which samples were taken for molecular analysis (Experimental) is added to visualise the location of the different model (B) and packed-bed fractions (F). Reactor height is expressed as the average height of the packed-bed fraction from which the samples were obtained.

It must be noted that the concentration results depicted in Figure 5.2 are those corresponding to the zone of the packed bed where the biofilm is growing on the BIOSTYR® support, whereas the biomass concentration of experimental fraction $F_0$ (i.e. fractions $B_1$ and $B_2$ according to the model definition) has not been included in the figure. The reason of this omission lies in the difficulty of estimating the real concentration of the experimental samples due to clogging. The concentrations presented in Figure 5.2 were calculated as dry weight related to the total volume of each packed bed fraction. In the case of fraction $F_0$, the exact space occupied by the biomass layer was difficult to establish with reasonable accuracy, leading to a misleading value of the experimental concentration that was not comparable to the value yielded by the model for the concentration in fraction $B_2$. To avoid misleading information, this point was omitted from the graph as it was not essential to establish the trend of the studied parameter.

Once the trend of the biomass to accumulate on the bottom sections of the packed bed was established, the next step was to extend the evaluation of the biofilm heterogeneity to the relative abundances of the different bacterial species, assessing their distribution along the packed bed vertical axis.

#### *5.4.3.2 Relative abundance of N. europaea and N. winogradskyi along the packed bed*

To study the relative abundance of the AOB and NOB along the packed bed, the concentrations of each bacterial species as estimated by the model at a time of 1750 days were used to calculate, through numerical integration across the biofilm thickness, a total concentration of each bacterial species for every fraction. Integration of the biomass profile obtained with the model in the biofilm depth was performed for each particular fraction in order to account for all the active cells present in the biofilm. The relative abundances (i.e. the ratio of each one of the two species performing the two-step nitrification process to the total *N. europaea* + *N. winogradskyi* amount) were calculated for each fraction and the results were compared to the experimental quantitative information obtained through Q-PCR analysis (Figure 5.3).

For a first approach only the two initial bacterial strains used to inoculate the reactor, i.e. *N. europaea* and *N. winogradskyi* were implemented in the model. However, since a certain level of contamination was detected through FISH analysis (Chapter 3), it was eventually recognised that the effect of the presence of heterotrophic bacteria could not be disregarded and thus a population of

heterotrophic bacteria was included in the model definition. In order to quantify and analyse the extent of the effect of the possible contaminants, the kinetics of a hypothetical population of heterotrophic bacteria (parameters from the models ASM1 and ASM2, Henze et al., 2000), were implemented in the model (Chapter 4).

Due to the absence of any organic carbon source in the culture medium, the population of heterotrophic bacteria could only have developed on soluble microbial products coming from the hydrolysis of cellular decay material, reducing the possible effect of the heterotrophic population on the final results at all levels. The results of the simulations that included the heterotrophic population proved that the presence of this bacterial population was indeed minimal throughout the packed bed. Only below a height of 12 cm (fraction $B_2$ or $F_0$, Figure 5.2), where the biofilm grew following the feed axis direction, the presence of heterotrophic biomass, in terms of dry weight, was higher, although relative abundance of *N. europaea* was not significantly affected. It must be noted at this point that, due to the large thickness of the biofilm layer in fraction B2 (5 cm), the results were found to be influenced by the number of grid divisions used for integration. Some test simulations performed after increasing the number of grid divisions used to discretise the biofilm in the bottom fraction (40 grid divisions instead of 20) revealed that the heterotrophs had a certain effect on the relative abundance on the bottom fraction, leading to slightly lower relative abundances of *N. europaea* that would be closer to the experimental Q-PCR measurement. In all remaining fractions, the relative distribution of *N. europaea* and *N. winogradskyi*, only suffered minor variations (1-5% at heights 20, 40 and 50 cm) when compared to the profile obtained in the absence of heterotrophic biomass (Figure 5.3), and these results were not altered by a reduction of the space discretisation unlike the bottom fraction.

The overall low presence of heterotrophic bacteria shown by the simulation results proves that, as expected, the limited availability of organic material is limiting the impact of the heterotrophic population on the nitrifying relative abundance, which would otherwise have a stronger effect. As indicated by experimental FISH results, the model simulations proved that the highest population of heterotrophic bacteria was found on the thick biofilm layer growing underneath the BIOSTYR® support. However, the overall impact of the presence of heterotrophic bacteria on the macroscale biofilm structure (relative abundance along the packed bed) and on the reactor operation (in terms of nitrification efficiency) at steady state was found to be minimal. The conversion of the incoming ammonium load to nitrite and nitrate showed good agreement with the experimental results (Table 5.2). The modelled

results were very similar with or without inclusion of the population of HB growing on decay products. Similarly, the profile of all soluble species with height obtained in the simulations with HB (Figure 5.4) did not differ from the modelled results obtained when HB were not included.

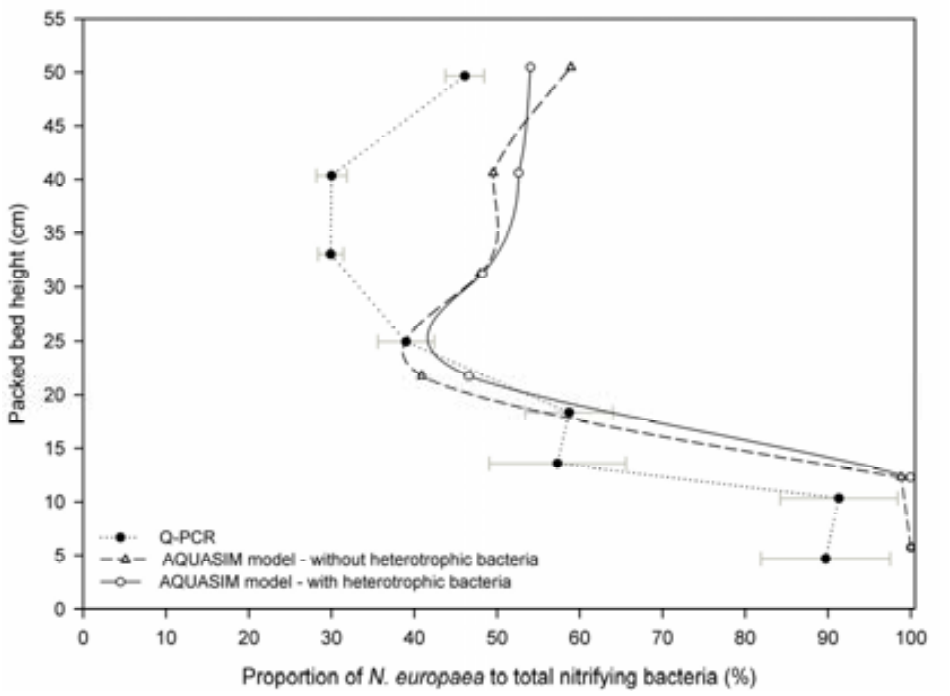


**Figure 5.3** Effect of the presence of heterotrophic bacteria on the relative abundance of *N. europaea* and *N. winogradskyi* along the packed bed.

However minimal the observed differences were, heterotrophic bacteria have been considered in all further simulations performed in this study, as their presence was experimentally confirmed in the simulated conditions (long term operation in which axenicity had been altered). The proportions estimated by the model reveal a general trend of the relative abundance that was qualitatively in agreement with the profile obtained by Q-PCR (Figure 5.3). Both the experimental and the modelled results pointed out a trend of the relative abundance of *N. europaea* to gradually decrease with height up to 30 cm, where the trend reverted, finally increasing again in the top fraction. In quantitative terms however, while the values of the relative abundance of *N. europaea* obtained through Q-PCR analysis matched the modelled results at heights up to 25 cm, the values predicted by the model in fractions $B_5$-$B_7$ differed from the experimental curve. To investigate the possible causes behind this discrepancy, the effect of different parameters on the biomass relative abundances was evaluated and will be presented hereafter.

The supply of substrates and oxygen are the main variables with a direct effect on the distribution of the different bacterial species within the biofilm or on the macroscale along the reactor. The profiles of oxygen and soluble nitrogen species in the bulk liquid, as predicted by the model, are depicted in Figure 5.4, where a gradient in all soluble species can be observed along the packed bed height. The nitrogen species profiles show a higher presence of ammonium at the bottom of the reactor. The profile thus suggests that ammonium was consumed almost completely in the two lower biofilm compartments ($B_2$ and $B_3$, between 5 and 15 cm), where the relative abundance of *N. europaea* was found to be maximum (60-90% of the total nitrifying population). A high ammonium oxidation activity matched the low dissolved oxygen availability in the lower fractions of the packed bed. In Figure 5.4 the dissolved oxygen concentration is shown alongside the concentration of the different nitrogen species. Clearly, the dissolved oxygen concentration decreases quite abruptly with height up to fraction $B_3$ (around 15 cm). However, starting at 15 cm and up to 40 cm, the oxygen concentration gradually increases again, remaining almost constant in the last two fractions of the packed bed ($B_6$ and $B_7$).

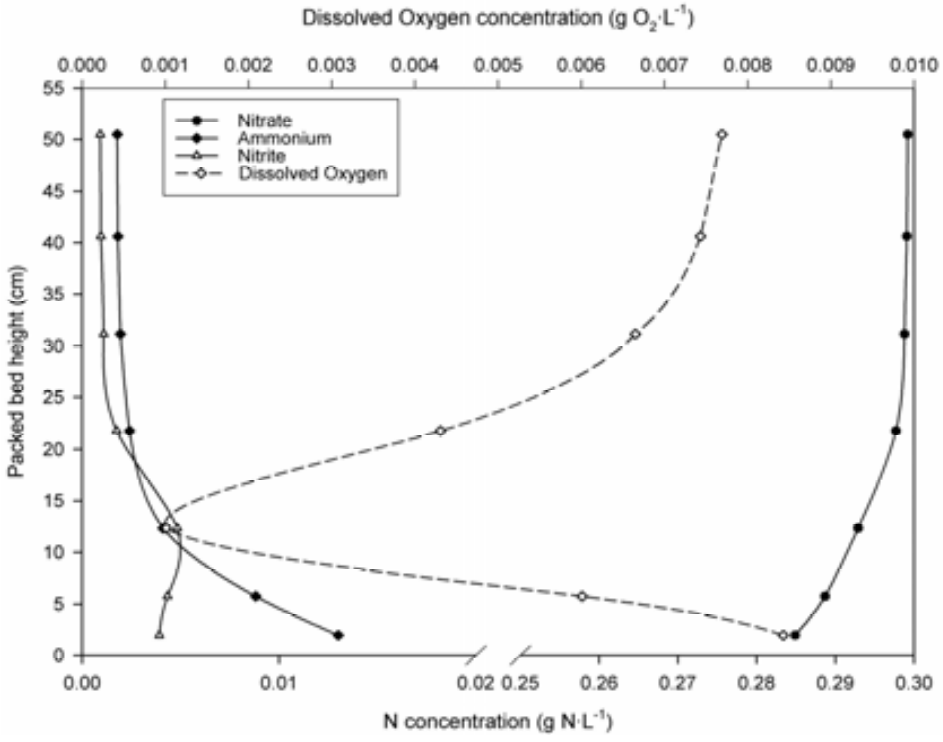


**Figure 5.4** Concentration of ammonium, nitrite, nitrate and dissolved oxygen along the packed-bed upon stop of the reactor operation (1750 days).

In addition to the availability of the different substrates determined by the stoichiometry and the kinetics of the process, there are a number of other parameters that are bound to have an effect on the biomass profile. A set of different

parameters, described in the following paragraph, were selected and their effect on the relative abundance of *N. europaea* and *N. winogradskyi* along the packed bed at steady state was assessed through simulation with the described model.

Specific simulations were conducted to evaluate the effect of (1) maximum density of the biofilm, (2) biofilm porosity, (3) biofilm thickness (LF), (4) the presence of heterotrophic bacteria growing on organic material originated from cell decay, (5) detachment rate, (6) liquid phase flow pattern, (7) growth yield ratio between *N. europaea* and *N. winogradskyi* ($Y_{X/S}^{Nts} / Y_{X/S}^{Ntb}$) and (8) oxygen concentration. Among those parameters, the ones that were found to have a relevant effect on the relative abundance of AOB and NOB along the packed bed height were (6) reactor hydrodynamics, i.e. the liquid phase flow pattern, (7) the ratio between the growth yields of the two involved nitrifying species and (8) oxygen gas-liquid mass transfer and its consequent effect on the dissolved oxygen concentration in the bulk liquid. The effect of each one of these parameters on the biomass distribution will be thoroughly analysed in later sections.

Other factors with a possible contribution – not examined in this chapter – are the kinetic parameters. Since the reactor was inoculated with an axenic culture containing two widely-studied bacterial strains, it was considered reasonable to assume that the literature parameters regarding these two species are quite accurate and no optimisation is necessary if a precise definition of all the relevant processes is provided.

#### *5.4.3.3 Effect of initial inoculum composition and biofilm thickness*

The pilot scale packed bed bioreactor was inoculated with a known volume of a culture broth containing a co-culture of *N. europaea* and *N. winogradskyi* that had previously been cultured in Erlenmeyer flasks and subsequently transferred to a bench scale (2 L) stirred tank reactor (Biostat B, B-Braun Biotech, Melsungen, Germany) to accelerate its development. The composition of the resulting culture broth could not be experimentally determined and thus the value used as an input for the model was an estimate based on the growth yields of the two bacterial species present in the culture, i.e. *N. europaea* and *N. winogradkyi*, as obtained from the literature (Hunik et al., 1993).

However, as the growth yields had not been determined experimentally, several simulations were performed to evaluate the effect of the inoculum composition on the final composition of the biomass population. The results

indicated that the model was not sensitive to either the initial inoculum composition or biofilm thickness, which is in agreement with similar results reported in the literature (Lackner et al., 2008).

In Table 5.3 the biomass profiles obtained at the final steady state (1750 days) with simulations performed using different values of the initial biofilm thickness and inoculum composition, are presented. From the results in this table it can be concluded that neither the composition of the inoculum, nor the initial biofilm thickness have any significant effect on the final biomass profiles in the packed bed.

**Table 5.3** Comparison of the biomass profiles obtained at 1750 days with different values of the initial biofilm thickness and different inoculum conpositions. Data expressed in % *N. europaea* referred to total nitrifying biomass (*N. europaea* + *N. winogradskyi*).

| Packed-bed height (cm) | LF=10µm 67%Nts/33% Ntb | LF=1µm 67%Nts/33% Ntb | LF=10µm 50%Nts/50%Ntb | LF=10µm 33%Nts/ 67%Ntb |
|---|---|---|---|---|
| 5.75 | 100.00 | 100 | 100 | 100 |
| 12.31 | 98.83 | 98.83 | 99.01 | 98.83 |
| 21.75 | 40.92 | 40.93 | 41.41 | 40.92 |
| 31.19 | 47.95 | 47.97 | 48.33 | 47.95 |
| 40.63 | 49.52 | 49.57 | 49.34 | 49.52 |
| 50.47 | 58.93 | 58.84 | 59.23 | 58.93 |

#### *5.4.3.4 Effect of the growth yield ratio between* N. europaea *and* N. winogradskyi

The first of the studied parameters was the growth yield of the two bacterial species involved in the two-step nitrification process. The results presented in Figure 5.5 suggest that the model systematically overestimated the relative abundance of *N. europaea* in all fractions of the packed bed, when compared to the Q-PCR profile. Since nitrification is almost complete in the reactor, this would point towards an overestimation of the growth yield ratio of *N. europaea* and *N. winogradskyi* ($Y_{X/S}^{Nts} / Y_{X/S}^{Ntb}$) as the cause for this divergence between the experimental and the predicted results.

Recently, the estimation of the true growth yield of *Nitrosomonas* and *Nitrobacter* has been the objective of research using respirometry (Vadivelu et al., 2006a and 2006b). Since *Nitrosomonas* and *Nitrobacter* use an important part of the energy gained from the oxidation of ammonia and nitrite (respectively) in maintenance, there are significant differences between the true and the apparent

yield (as pointed out by Vadivelu et al., 2006a and 2006b). Since the kinetic model (described in Table 4.4) considers maintenance, the true growth yield must be used.

All stoichiometric parameters, and hence the growth yields, used in this study were taken from the same source (Hunik et al., 1994; Chapter 4, Table 4.2). The growth yield coefficient used for *N. europaea* was an averaged value based on literature data, as reported by Hunik, 1993 and thus it was not experimentally determined. Likewise, the *Nitrobacter* growth yield used in this study was also derived from the studies performed by Hunik (1993). It must be underscored that *N. agilis* was expected to be the predominant strain in the particular process conditions used by Hunik (1993). Pan (1971; cited in Hunik, 1993) and Watson (1974; cited in Hunik, 1993) suggested that *N. agilis* and *N. winogradskyi*, formerly considered as two different species, had no significant morphological differences and should thereafter be combined as two strains of the common species *N. winogradskyi*. Therefore, the growth yield used by Hunik (1993) was initially considered to be applicable to the present work. However, since other studies (Fliermans et al., 1974) had, indeed, suggested the existence of a difference between the two strains, it is reasonable to believe that the value used as the *N. winogradskyi* growth yield in the definition of the model (Table 4.2, Chapter 4) might not be accurate. Based on the hypothesis that the assumed *N. winogradskyi* growth yield coefficient was inaccurate for the reasons stated above, the relative bacterial abundance along the packed bed was simulated using three different values for the ratio $Y_{X/S}^{Nts} / Y_{X/S}^{Ntb}$ (2.8, 2.5 and 2.2, respectively; Figure 5.5).

Results obtained by decreasing the growth yield ratio are closer to the experimental results and thus the conclusion was drawn that the ratio $Y_{X/S}^{Nts} / Y_{X/S}^{Ntb}$ used in the model is most probably overestimated. The possible underestimation of the *N. winogradskyi* growth yield will be further discussed in section 6.3.2, where optimisation of this parameter will be performed during the calibration of the model for its exploitation under dynamic conditions.

#### *5.4.3.5 Effect of the liquid phase flow pattern*

As shown in Figure 5.6, the contribution of plug flow detected through RTD analysis induced a gradient of substrates along the feed direction of the packed bed, producing a segregation of the two bacterial species. Reactor hydrodynamics were modelled by means of a tanks-in-series model with the addition of a back mixing term, as described in Chapter 4, section 4.2.4.2. The packed bed was divided into N

tanks of equal liquid volume, where N was originally set to 7. The back mixing flow rate was a function of the feed flow rate, the recycling flow rate and a back-mixing coefficient (*f*), which was fitted through optimisation with the RTD experiments. The division of the packed bed into N=7 tanks yielded a back-mixing flow rate of 314.5 $L \cdot d^{-1}$. To evaluate the effect of the plug flow on the segregation of the bacterial population, simulations were performed with back-mixing flow rates of 228.5 $L \cdot d^{-1}$ and 440.3 $L \cdot d^{-1}$ (Figure 5.6).

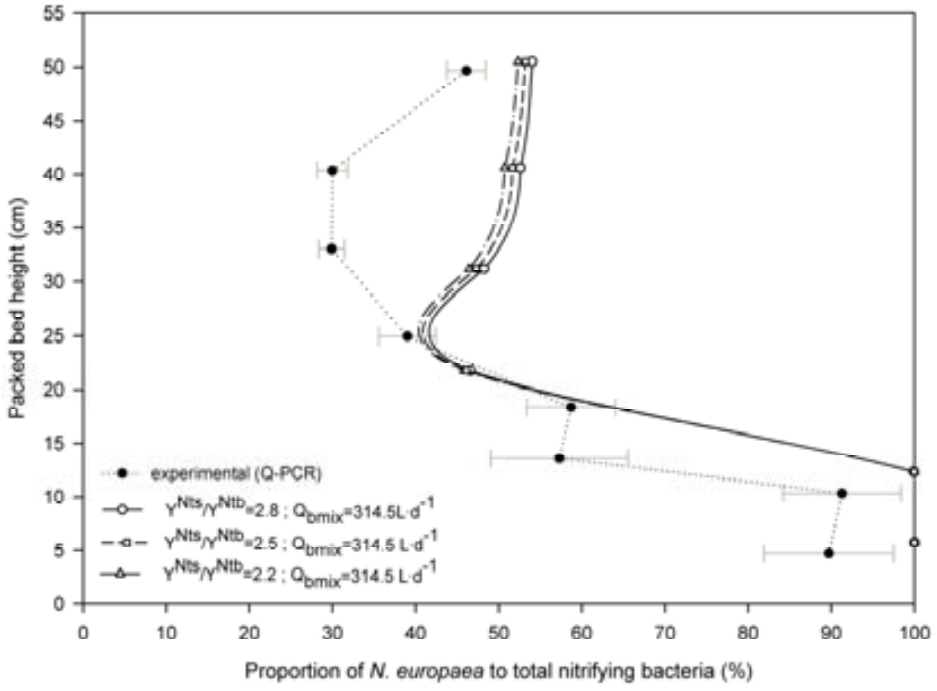


**Figure 5.5** Effect of the *N. europaea/N. winogradskyi* growth yield ratio on the simulated relative abundances of *N. europaea* and *N. winogradskyi* along the packed bed.

An increase of the plug flow contribution (i.e. a higher deviation from perfectly mixed tank behaviour in the overall flow pattern of the liquid phase in the reactor, simulated by using a back mixing flow rate of 228.5 $L \cdot d^{-1}$), produced a more significant segregation of *N. europaea* and *N. winogradskyi* (Figure 5.6). The biggest impact of the plug flow contribution can be observed in the lower fractions of the packed bed (up to a height of 20 cm), where a decrease of the back mixing flow rate clearly affects the profile, enhancing the segregation of the two bacterial species. On the other hand, a lower contribution from plug flow ($Q_{bmix}$ =440.3 $L \cdot d^{-1}$) improves the correlation between the experimental curve and the modelled profile. Therefore, it appears that plug flow contributed to the compartmentalisation of ammonia oxidation and nitrite oxidation. This is not entirely unexpected for two consecutive reactions in which the metabolic by-product of *Nitrosomonas* (i.e. nitrite) is the growth substrate of *Nitrobacter*.

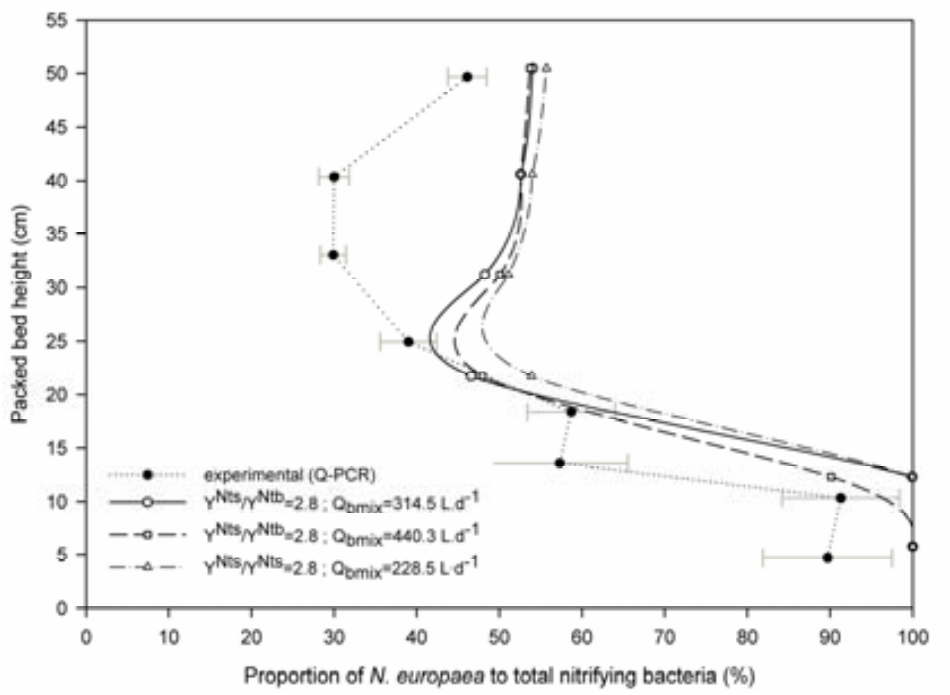


**Figure 5.6** Effect of the back-mixing flow rate on the simulated relative abundances of *N. europaea* and *N. winogradskyi* along the packed bed.

#### *5.4.3.6 Effect of oxygen concentration*

The amount of oxygen available for the biofilm to carry out the ammonium and nitrite oxidation was expected to have an effect on the relative distribution of the two nitrifying species. The nitrite concentration under our operating conditions (T=28 ºC and pH=8.1) is below the values reported by Anthonisen et al. (1976) (Figure 4.7, Chapter 4) as producing inhibition by free nitrous acid.

Due to the complexity of the assessment of the oxygen mass transfer, the effect of possible changes of the $K_L$·a on the relative abundance along the packed bed was studied. The results are shown in Figure 5.7. The $K_L$·a variation has a more relevant effect on the lower fractions of the packed bed. At heights between 12 cm and 25 cm the relative abundance of *N. europaea* is clearly lower while fractions closer to the top are not as visibly influenced by the change in the oxygen gas-liquid mass transfer coefficient.

The inclusion of HB in the model definition, as well as the introduction of a $K_L$·a profile along the packed bed height, were implemented in order to make the model definition more exhaustive. However, it must be taken into account that the study of a single steady state is not sufficient to accurately and quantitatively assess the effect of these two parameters. The results presented in this chapter should be

taken as a way to evaluate the overall trend of the biomass profile along the packed bed height qualitatively and to study the potential effect of different parameters.

In earlier simulations the oxygen mass transfer was simply considered as not limiting, i.e. a high value of $K_L \cdot a$ was assumed for all fractions. Those simulations revealed lower proportions of *N. europaea* between 30 cm and 50 cm.

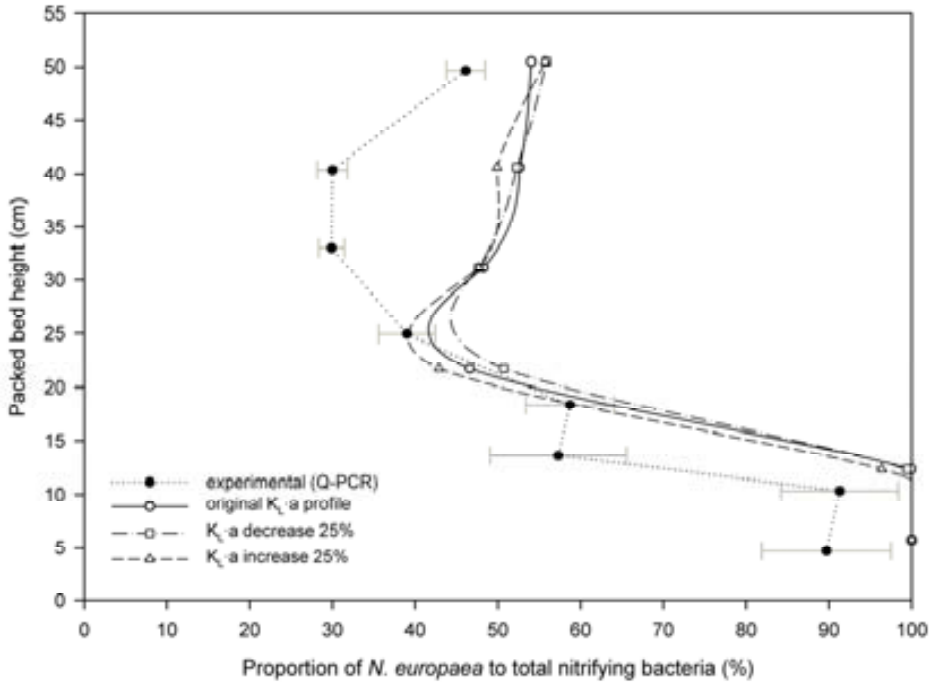


**Figure 5.7** Effect of a change in the gas-liquid mass transfer for oxygen on the simulated relative abundances of *N. europaea* and *N. winogradskyi* along the packed bed.

## 5.5 CONCLUSIONS

The mathematical model developed in Chapter 4 was successfully applied to the simulation of the reactor performance in steady state. The focus was on the macroscale biomass distribution along the packed bed. The following conclusions were drawn by this study:

- *N. europaea* and *N. winogradskyi* remained the most dominant AOB and NOB species in the packed-bed after 4.8 years of continuous operation.
- The relative distribution of *N. europaea* and *N. winogradskyi* in the biofilm reactor was quantified using Q-PCR, revealing a spatial segregation between the ammonia oxidiser and nitrite oxidiser on the macroscale, along the vertical axis of the packed bed.

- The mathematical one-dimensional biofilm model generated simulations in agreement with the relative bacterial abundance of *N. europaea* and *N. winogradskyi* as was estimated experimentally.
- The effect of several parameters on the profile of *N. europaea* and *N. winogradskyi* along the packed bed height was investigated. The parameters that were found to have a contribution to the bacterial segregation were (i) the liquid phase flow pattern, (ii) the ratio between the growth yields of *N. europaea* and *N. winogradskyi* and (iii) the dissolved oxygen concentration. Other investigated parameters (e.g. the presence of HB growing on decay products, the initial biofilm thickness, the biofilm porosity or the inoculum composition) showed minimal- or no- effect on the final distribution.
- An increase in the plug flow contribution led to more significant segregation of the *N. europaea* and *N. winogradskyi* along the packed bed height. The effect of the flow pattern is more relevant in the lower fractions of the reactor.
- The possible underestimation of the growth yield of *N. winogradskyi* was identified. A change in the ratio $Y_{X/S}^{Nts} / Y_{X/S}^{Ntb}$ in the higher fractions of the packed bed has a clear effect on the curve of the relative distribution of the two bacterial strains, a decrease of the ratio $Y_{X/S}^{Nts} / Y_{X/S}^{Ntb}$ leading to a better correlation with the experimental data with i.e. when $Y_{X/S}^{Ntb}$ increases.
- A decrease of the oxygen mass transfer coefficient had a stronger effect on the lower fractions of the packed bed, where the oxygen requirements are higher.